SLAC-PUB-1903
March 1977
(T/E)

LARGE p_T PHYSICS: DATA AND THE CONSTITUENT MODELS*

S. D. Ellis

Department of Physics
University of Washington, Seattle, Washington 98195

R. Stroynowski

Stanford Linear Accelerator Center
Stanford University, Stanford, California 94305

ABSTRACT

Recent developments in the field of large p_T physics are reviewed. Special attention is paid to the explanation of the data offered by specific constituent models. Emphasis is placed on those data which tend to differentiate between the models. Prospects for better understanding of large p_T events as the result of new experiments and further theoretical work are discussed.

(This report constitutes a summary of the talks given at the topical meeting on large p_T physics held at the Stanford Linear Accelerator Center on October 29, 1976. Also submitted for publication.)

*Work supported in part by the Energy Research and Development Administration.

Table of Contents

1. INTRODUCTION

The observation (1) that the transverse momentum spectrum of produced particles deviates, at high energies and large p_T, from the exponential behavior observed at low p_T has raised hopes that in such processes one has started to probe the structure of hadronic reactions at very short distances. Several fairly sophisticated pictures of constituent interactions were subsequently developed (2) which in turn have stimulated increased effort on the part of experimentalists to study new and varied aspects of the events containing large transverse momentum hadrons. As a result, a large amount of new data has become available during the past two years.

The first half of this report includes a review of the data. Emphasis is placed on recent results, as the earlier data have been extensively reviewed (3) and are well known today. The second half of the report comprises an overview of two apparently distinct constituent interaction pictures. While reviewing those features of the models which are consistent with the existing data, special attention is paid to those aspects which are most likely to distinguish between the two models. Many of the comments made are also applicable to other large p_T constituent models and this is pointed out when relevant. Also a list of the experimental quantities best suited for further study of the constituent models is provided.

2. SINGLE PARTICLE DISTRIBUTIONS

In most experiments the large transverse momentum spectrum is measured for the particles emitted at 90^o in the c.m. system. The large p_T signal is expected to be cleanest there and least affected by kinematical effects near the phase space boundary. Both ISR and FNAL experiments extend their measurements up to a value of $p_T \sim 7$ GeV/c. In terms of the reduced transverse momentum

$x_T = 2p_T/\sqrt{s}$, this corresponds to $x_T \sim (0.25 \text{ to } 0.30)$ for the higher energies of the ISR and to $x_T \sim 0.7$ for the FNAL experiments. There are also published measurements of the large p_T spectra at smaller emission angles. Knowledge of the angular dependence of single particle distributions is, however, still fragmentary.

The general features of the momentum spectra of particles emitted at 90^o in the cms at high energy can be summarized as follows.

i) The transverse momentum spectrum deviates for $p_T \gtrsim 1.5$ GeV/c from the exponential distribution observed at small p_T values. The parametrization $E\frac{d^3\sigma}{dp^3} = A\, e^{-6p_T}$, which describes well the bulk of the data at small p_T, is about two orders of magnitude lower than the measured points at 3 GeV/c.

ii) The measured cross section shows strong energy dependence at fixed p_T values ($\gtrsim 1.5$ GeV/c) across the ISR energy range. The invariant cross section at $p_T = 3$ GeV/c increases by a factor of ~ 5 when $\sqrt{s}$ increases from 23 to 63 GeV (see Figure 1).

2.1 Scaling

The invariant cross section distribution was parametrized in different experiments by a host of various phenomenological functions. The success of the constituent models justifies a preference for a parametrization of the form

$$E\frac{d^3\sigma}{dp^3} = A\, p_T^{-N}\, f(x_T, \theta) \qquad 1$$

or, in order to take into account also the low p_T region,

$$E\frac{d^3\sigma}{dp^3} = A\left(p_T^2 + M^2\right)^{-N/2} f(x_T, \theta) \qquad 2$$

These parametrizations factorize the explicit p_T dependence from the dimensionless scaling function $f(x_T, \theta)$ dependent only on the reduced transverse momentum and the emission angle θ. The scaling function, expected in parton models to be energy independent at fixed x_T, is often parametrized at $\theta = 90^o$ as

$$f(x_T, \theta)|_{\theta=90^o} = (1-x_T)^F \quad . \qquad 3$$

A compilation of the parameters N, M^2 and F as obtained in various experiments is given in Table 1. It is important to recall, however, that these parameters are not necessarily of a fundamental nature. In particular, even in the models Equation 3 is only an approximation except near $x_T = 1$.

To summarize the table, the value of N is equal to ~8 for pions, 8-9 for kaons, 10-12 for protons and ~9 for antiprotons. These values are generally compatible with those suggested by the dimensional counting rules (10) and are discussed further in Section 4.

The function $f(x_T, \theta)$ presented in Figure 2 for the data of the CERN-Columbia-Rockefeller-Saclay Collaboration (4) shows indeed very good scaling properties within the systematic uncertainties of the ISR experiments. The functional form is difficult to determine at the ISR due to the rather small range of x_T measured. The results of the recent Chicago-Princeton (6) experiment extending to $x_T \sim 0.7$ indicate good agreement with a $(1-x_T)^F$ behavior.

The high values of the parameter N observed in the early part of the Chicago-Princeton experiment (11) were derived from the extrapolation of the measurements performed on nuclear targets. Recently a hydrogen target was used giving lower values of the parameter N, compatible with the ISR results. The data indicate that the atomic number dependence of the particle yields observed previously is also p_T dependent, $\sim A^{\alpha(p_T)}$. The values of $\alpha(p_T)$ are shown in Figure 3 for π^+ and π^- production.

So far little is known about the emission angle dependence of the function $f(x_T, \theta)$. Data of the ACHM Collaboration (7) on π^o production indicate no significant angular variation in the range $53^o \leq \theta^* \leq 90^o$ in the cms. At smaller emission angles, the large p_T π^o spectrum, measured by the FNAL-Northern Illinois group (12), shows surprisingly good scaling when x_T is replaced by $x_R = 2p/\sqrt{s}$ (Figure 4) and there is no other θ dependence. More detailed measurements of the production of charged particles are needed, however, to check further the validity of this parametrization.

2.2 Particles Ratios

The relative yields of particles with large p_T are of great interest as a testing ground for various phenomenological models. It was known already from the early ISR experiments (5) that the π^+ to π^- cross section ratio, $R_{prod}(\pi^+/\pi^-)$, is 1.2-1.3 at large p_T values and that the relative yield of heavier secondaries (K and p) increases with increasing transverse momentum for $p_T \leq 3$ GeV/c. Recent Chicago-Princeton Collaboration data (6, 13) permit the study of relative yields also in the large x_T range.

The results shown in Figure 5a indicate approximate scaling of $R(\pi^+/\pi^-)$ and, at small x_T, values compatible with the previous British-Scandinavian Collaboration measurements (5) at the ISR. At larger x_T $R(\pi^+/\pi^-)$ increases rapidly up to the value of about 3 at x_T=0.6 in agreement with parton model predictions.

For pn interactions $R(\pi^+/\pi^-)$, presented in Figure 5b, is derived from the difference between the results of pp and pd measurements and shows no deviation from the value R=1 expected at 90^o from isospin conservation.

The ratio of heavier particle yields to that of pions of the same charge is illustrated in Figure 6. It increases at small transverse momentum with increasing p_T, reaching a maximum at $p_T \sim 2$ GeV/c. Then, except for $R(K^+/\pi^+)$,

it decreases in the large p_T region, where pion production accounts for 70-80% of the total yield.

The Chicago-Princeton data from FNAL are in most cases in good agreement with previous ISR results. They indicate, however, a significantly smaller cross section for $\bar{p}$ production at large p_T then previously measured. This discrepancy will be resolved in the near future, as there are several second generation experiments set up at the ISR and FNAL equipped for particle identification.

It is interesting to note that the ratio of positive to negative secondaries, is increasing with p_T much more dramatically for heavier particles than for pions, rising above 20 for $R(p/\bar{p})$ at $p_T > 5$ GeV/c (see Figure 7).

The parametrization with formula 1 describes not only the single particle spectrum but also the ratio of the particle yields. This is illustrated in Figure 8 where the scaling function $f(x_T, \theta)$ is presented for the p/π and K/π ratios. The parametrization with $(1-x_T)^F$ seems to satisfactorily describe the large x_T region. The large errors in the fit with the parameters N and F, given in Table 2, reflect the uncertainty in defining the x_T region in which the parametrization is to apply.

2.3 Beam Ratios

The first measurement of π^o production at large p_T using various beams was performed recently by the BNL-CIT-LBL Collaboration (8) at 100 and 200 GeV/c. The ratio R_{beam} of the invariant cross sections, presented in Figure 9, shows no difference in the π^o production spectra from π^+ and π^- beams. However, comparing proton with pion beams, one notices immediately a strong p_T dependence of R_{beam}. At low transverse momentum the ratio of differential cross sections is approximately equal to the ratio of the total pp and πp cross sections

at the same energies. With increasing p_T, π^o production becomes more likely in the case of the pion beam than for the proton beam. Although the energy range is rather limited, the ratio $R\left(\frac{pp \rightarrow \pi^o X}{\pi p \rightarrow \pi^o X}\right)$ indicates rather good scaling as a function of x_T (see Figure 10) with the parametrization $f(x_T) = (1-x_T)^{1.6\pm.5}$.

3. CORRELATIONS

The vast amount of data on the general characteristics of events with a large p_T particle, measured in ISR experiments, was extensively reviewed by many authors (3, 15). Therefore, after a brief summary of known facts, the main discussion will concentrate on recent results.

Due to experimental difficulties in estimating multiparticle efficiencies and acceptances over the large solid angle covered by the experiments, large p_T events are usually compared to normal hadronic collisions collected with the same apparatus in "minimum bias" trigger modes. Such a comparison eliminates acceptance problems in first approximation. A schematic description of the kinematical regions commonly used in the study of large p_T events is shown in Figure 11.

Before giving a detailed discussion, it is useful to first summarize the overall differences of large p_T events with respect to minimum bias events.

1) There is an increase of multiplicity of produced particles.
2) This increase is spread over a relatively large rapidity range dependent on the azimuthal direction ϕ with respect to the trigger. As can be seen in Figure 12, it is broader and more prominent at a value of ϕ opposite to the large p_T particle than at other azimuthal angles.
3) This increase of multiplicity also depends on the transverse momentum of the triggering particle. As seen in Figure 13 it

has an approximately linear dependence on p_T (trigger) with the largest slope in the region of $\phi=180^o$.

4) Although hinted by the early results of the Daresbury-Illinois-Liverpool-Rutherford Collaboration (16), there is, as yet, little firm evidence that the correlations observed are dependent on the type of the triggering particle.

5) The correlation with the large p_T particle is also a function of the transverse momentum of the secondaries. The strength of the correlation increases with increasing p_T (Figures 14 and 15) of the secondary.

From the above general features a picture has evolved of large p_T events as having three components:

i) "towards" jet—small cluster of particles emitted together with the triggering particle;

ii) "away" jet—large number of particles balancing the transverse momentum of the trigger but spread over a large rapidity range on average;

iii) underlying low p_T cloud—presumably little affected by the superimposed jet structure.

The structure of these three components will be discussed next.

3.1 Low p_T Cloud

Little is known at present about the behavior of the low p_T secondaries in large p_T events. This situation is to a large extent caused by the experimental difficulties in measuring low p_T particles at the ISR. The data of the CERN-College de France-Heidelberg-Karlsruhe Collaboration (17) shown in Figures 14 and 15 indicate some structure in the central rapidity region. This is most

clearly visible in the azimuthal wedge towards the trigger. Whether this structure is a real effect or reflects experimental problems of the apparatus is the subject of ongoing studies. In various constituent models different numbers of quarks take part in the interaction. This results in different expectations for the charge distribution of low p_T secondaries. Precise studies of the low p_T particles in large p_T events are useful for testing the details of the various models and are needed in order to distinguish the superimposed jet structure.

At large values of longitudinal momentum, there is evidence for the leading particle effect in large p_T events. Leading particles are usually defined as secondaries of the same charge as the beam particle and carrying most of the beam momentum ($x > 0.5$). They are quite common in normal pp interactions and occur in ~27% of the events. The CCHK Collaboration has shown (18) that the fraction of events with a leading particle, presented in Figure 16, decreases in large p_T events with increasing transverse momentum of the trigger. This effect was recently confirmed by the British-French-Scandinavian group (19) which had also shown that the probability of observing a leading particle is the same whether the high p_T trigger is a pion, kaon or proton. The compatibility of the values from these two experiments, compared in Figure 16, indicates that the effect is independent of the emission angle of the high p_T particles.

In Figure 17 the longitudinal x distribution of leading particles in large p_T events is compared to that for normal events. The prominent diffractive peak observed in minimum bias events is strongly suppressed. This suppression is partially caused by energy-momentum conservation effects since a large fraction of the c.m. energy is taken by the triggering particle and accompanying jet. In the "towards" azimuthal wedge (least affected by these kinematical effects) there is indeed a forward peak in the low p_T secondaries (Figure 15).

3.2 Towards Jet

It was already noted that large transverse momentum particles are usually accompanied by an excess of particles collimated both in azimuth and in rapidity near the trigger. This excess, illustrated again in Figure 18, is usually referred to as the towards jet. The properties of the towards jet were studied during the past year in several experiments. Eggert et al reported (20) that the average number of charged particles in the jet, other than the trigger, is about 0.85. This number strongly depends on the definition of the jet and can vary, as shown in other analyses (21, 22) between 0.5 and 1.5. The particles belonging to the jet show an azimuthal symmetry with respect to the jet axis, while their momentum transverse to the jet axis, p_T^j, shown in Figure 19, is limited and well described by the function $e^{-6\left(p_T^j\right)^2}$.

The collimation of the particles inside the jet increases with the p_T of the secondaries, and exhibits characteristics similar to the correlations among the decay products of low mass resonances. This is clearly illustrated by data of the CERN group (21) in Figure 20, where the effective mass of a large p_T π^o and a charged secondary assumed to be a pion is shown. Above the background of uncorrelated particles a prominent signal may be observed in the low $(\pi^o\pi^+)$ mass region. It is dominated by the $\rho^\pm$ peak for higher values of charged pion transverse momentum. The ρ signal is more clearly visible in Figure 21 where only pions with $p_T > 0.7$ GeV/c are included. This restricts the transverse momentum of the ρ to be above 2 GeV/c with $\langle p_T \rangle_\rho \approx 3.5$ GeV/c. An estimate of the ρ production cross section yielded the ratio $1/2\ (\rho^+ + \rho^-)/\pi^o = 0.9 \pm 0.2$. It follows that at least 16% of the observed large p_T π^o signal is derived from ρ decays. Similarly, the CCHK Collaboration had observed (3) a clear ρ^o signal (see Figure 22) and estimated the ρ^o/π^- ratio to be compatible with ~ 1.4 at

$p_T(\rho) > 2$ GeV/c. These values should be taken as conservative estimates burdened with large systematic errors because the selection criteria for correlated particles limit the acceptance for the ρ decay products. This acceptance effect in turn depends strongly on the polarization of the ρ produced at high p_T.

Due to the lack of identification of the charged secondaries in the ISR experiments, all charged particles are usually assumed to be pions. However, in the p_T region studied it is known that kaons represent about 10% of the pion yield. When a kaon is misidentified as a pion the K^*_{890} resonance peak is shifted to $M(\pi\pi)$ 400 MeV/c. There is indeed an indication of such an enhancement in Figure 21. Further confirmation of large p_T K^*_{890} production is given in Figure 23 by the preliminary data of the British-French-Scandinavian Collaboration (19). The results indicate that a large fraction of the high p_T particles comes from the decays of low mass $\pi\pi$, $K\pi$ and $p\pi$ resonances.

The two-body resonances are not sufficient, however, to explain all the observed correlations inside the towards jet. This is illustrated in Figure 24 which shows the rapidity distribution of secondaries with $p_T > 1$ GeV/c of the opposite and same charge as the trigger ($y_{trigger}=0$). When the trigger momentum increases, there is an enhancement for both the opposite charge and same charge secondaries at small y. Whether this effect can be fully explained by the production and decay of large p_T three-body resonances like A_2, K^*_{1420} etc remains as yet unsolved.

Ellis, Jacob and Landshoff had noticed (23) that by requiring in the trigger a single large p_T particle, experiments may introduce a trigger bias against multiparticle jets. A new series of calorimeter type experiments triggering on large energy emitted at 90^o in the cms will soon shed more light on this problem.

3.3 Away Jet

The third component in large p_T events is manifested in the azimuthal region away from the trigger (ϕ=180^o) by an excess of particles over the minimum bias distribution (see Figures 14 and 15) in a broad range of rapidity. The number of charged particles in this region increases linearly with the p_T of the trigger with a slope of about 0.8 GeV/c and is little dependent on the nature of the trigger.

The away secondaries show increasing collimation around ϕ=180^o with increasing transverse momentum (Figure 25). The p_{out} component of transverse momentum, perpendicular to the triggering plane defined by the beam and triggering particle is independent of the p_T of the trigger (see Figure 26). The average $\langle p_{out} \rangle \approx 500$ MeV/c is approximately independent of the rapidity and the charge of the secondaries. This may be contrasted to minimum bias events where the average p_{out}, defined with respect to an arbitrary plane, increases with the p_T of the particles.

The shape of the rapidity distribution of the correlated secondaries is weakly dependent on the transverse momentum of both the trigger and "away" particles. The enhancement, spans about four units of rapidity for the low p_T secondaries and about 3 units for the large p_T particles. This collimation increases with p_T of the trigger.

In experiments where the large p_T particle is detected at 90^o in the c.m. system, the rapidity distribution in the away region is symmetric around y=0. It remains symmetric even when the emission angle of the trigger particle varies. The CCHK collaboration has measured (17) events with positive and negative large p_T particles emitted at θ=45^o and 20^o and the Pisa-Stony Brook group has observed (24) events with large p_T photon emitted at θ=17.5^o in the cms. In

both experiments the average transverse momentum of the triggering particle was about 2.5 GeV/c and the "away" rapidity distribution showed a broad enhancement centered around y=0. An exception is quoted in the ACHM Collaboration experiment (7) in which a streamer chamber was triggered by a large p_T π^o ($\langle p_T \rangle = 3.8$ GeV/c) at $\theta=53^o$. Here, the y distribution in the away region, presented in Figure 27, shows a shift to rapidities opposite to the rapidity of the triggering π^o. Although this effect needs further confirmation, it indicates the interesting possibility that a back-to-back correlation in rapidity may evolve with increasing transverse momentum of the trigger, and that for very large p_T triggers, the towards and away jets may tend to balance not only their transverse but also their longitudinal momentum.

The question of whether the away jet is indeed very broad, or if it has the same characteristic width as the towards jet, i.e., narrow in rapidity in any given event but with an axis varying from an event to event, was studied in several experiments (19, 21, 22). All of them report strong short range correlations in rapidity among the "away" particles which increase with their transverse momentum. The effect is illustrated in Figures 28 and 29. The correlation is stronger by about a factor of 2 for opposite charge pairs than for the particles of the same charge. This may indicate substantial resonance production. The short range correlations although centered around y=0, are not restricted to the small rapidity region. The contour lines of the correlation function for opposite charge pairs shown in Figure 30 span four units of rapidity. Evidence exists, therefore, for the narrow jet-like structure also in the away region. The axis of the jet, however, strongly varies from one event to another.

In most of the parton models the away jet originates from the fragmentation of the scattered constituent. Factorization and scaling hypotheses for the jet

assert that the distributions of the fragments should be independent of the origin of the constituent and of its momentum. The CERN group (21) has compared the spectrum of particles in the away jet in terms of the variable $x_E = p_T / |p_T \text{ trigger}|$ for a large p_T π^o trigger and the corresponding distributions obtained from deep inelastic ep scattering and e^+e^- annihilation. The shape of the distribution, shown in Figure 31, does not change significantly whether the p_T of the trigger or the p_T of the presumed towards jet is taken in the definition of x_E. The similarity of the shapes of the distributions indicates good agreement with the expectations of factorization.

Similar spectra presented by the CCHK Collaboration for a 45^o trigger (25) show (Figure 32) strong variation with the p_T of the trigger. Although at first sight this result looks like a violation of scaling it may merely reflect the difficulties of separating the particles belonging to the away jet from the low p_T cloud, as the possible overlap of these two components vary with the p_T of the trigger. More data at higher values of transverse momentum are needed to study this question of scaling. This is particularly important as a test of the relevance of the constituent models which naively predict independence of the p_T of the trigger.

4. THEORETICAL OVERVIEW

The purpose of the following sections is to review what is understood about the structure of large p_T events and to focus attention on those experimental results which most easily distinguish between the various theoretical models available (26). In particular the quark-quark scattering picture (Q-Q) of Field and Feynman (14) will be contrasted with the Constituent Interchange Model (CIM) of Blankenbecler, Brodsky and Gunion (27). One must keep in mind, however, the work of other groups not discussed in detail here. A well known example is the

quark-fusion model of the Cambridge group (28), in which the final meson-meson state has recently been generalized to a jet-jet state (29). This picture shares many features with the CIM. Another well studied model is the Massive Quark Model of Preparata and collaborators (30). Attention is also drawn to the recent work of various groups (31) who invoke power type nonscaling behavior in the initial quark distributions or in the scattering process to explain the observed data. The limitation of the discussion to "hard scattering" models reflects both the personal biases of the authors and the fact that the existing correlation data are highly suggestive of the jet picture which arises naturally in such models.

In the context of "hard scattering" models one's understanding of the experimental data on large p_T events arises from the following qualitative picture (2, 23, 32):

The large p_T event is produced via the "hard" scattering of two, perhaps fundamental, hadronic constituents. Subsequent to the scattering process, the constituents, both those at large p_T and those still moving in the initial direction, evolve into hadrons. This second step is presumed to occur in a fashion characteristic of the more usual "soft" (low momentum transfer) hadronic interactions. This implies a certain scaling behavior specified more completely below. It is, however, already familiar in normal, low p_T, hadronic reactions (Feynman scaling) and is apparently also observed in lepton induced deep inelastic processes. The result is a picture in momentum space wherein the final hadrons appear in a coplanar jet configuration with jets of hadrons aligned with the directions of both the scattered constituents and the unscattered constituents. There is a jet along the initial beam direction (the low p_T cloud) and one along the direction of each of the scattered constituents. The jets are visualized in momentum space as cylinders which are exponentially cutoff in the radial direction with radius

$\sim$300 MeV/c independent of s, p_{jet} etc. It should be noted that, a priori, the two jets do not have to be collinear in the overall center-of-mass system since the center-of-mass of the scattering constituents is generally moving in the overall frame. This two step development is schematically illustrated in Figure 33, where Figure 33a indicates the distribution of constituents in momentum space immediately after the hard scattering and Figure 33b shows the resulting hadronic distributions. Note that constituents which are initially isolated in momentum space evolve into several hadrons, i.e. into jets.

In order to discuss this process more specifically it is necessary to introduce functions which describe the distributions of constituents inside the initial hadrons and the corresponding functions for the distributions of hadrons within the jets. Note that this factorization (incoherence) between the structure of the initial state prior to the hard scattering process and the subsequent evolution of the scattered constituents is central to the basic impulse approximation approach to the large p_T process. The assumption is that the bulk of the strong interactions involve communication only between constituents of small relative invariant subenergies. Furthermore, during the short time and distance scales characteristic of the hard scattering, the large momentum ($\sim\sqrt{s}$) constituents are acting essentially freely. The central assumption concerning the structure of the aforementioned distribution functions is that they are rapidly cutoff functions of the transverse momentum and are dependent on only the fraction of the longitudinal momentum. Define the scaling variables (let $\bar{q}$ be the three-momentum of a constituent or jet and $\bar{p}$ be the three-momentum of a hadron). $x=\frac{\bar{q}\cdot\bar{p}}{\bar{p}^2}$ and $z=\frac{\bar{q}\cdot\bar{p}}{\bar{q}^2}$. The probability to find constituent a in hadron A in the range dx_a about x_a and $d^2\bar{K}_a$ about $\bar{K}_a$ ($\bar{K}_a$ is a two dimensional transverse vector) is taken

to be

$$dP_{a/A} = F_{a/A}(x_a, \bar{K}_a)\, dx_a\, d^2\bar{K}_a \quad . \tag{4a}$$

The logarithmic corrections inherent in the now popular gauge theories of strong interactions will be ignored in this discussion. The corresponding distribution for hadron B in a jet resulting from constituent b is described by

$$dP_{B/b} = D_{B/b}(z_B, K_B)\, dz_B\, d^2\bar{K}_B \tag{4b}$$

These particular forms are favored by various theoretical considerations, but more importantly they are consistent with the observed structure in deep inelastic lepton induced events (e.g. $ep \rightarrow eX$). In particular, the lepton induced process is viewed as being initiated by the scattering of the lepton by a hadronic constituent. The resulting picture is similar to Figure 33a where all the constituents above and to the right of the origin are replaced by a single lepton. Hence the lepton induced reactions are thought to measure at least a subset of these distributions directly. It is exactly this organic relationship to lepton physics which makes the hard scattering explanation for large p_T events so attractive. Expressions 4a and 4b are not just arbitrary functions for large p_T processes only but are, in principle, measurable in other reactions. For the present purposes the notation is simplified by taking the limit of a δ function distribution in $\bar{K}$ so that the $d^2\bar{K}$ integrals effectively drop out, i.e. constituents have only longitudinal momentum components inside the hadrons.

The final ingredient needed in order to define the large p_T process, is the cross section for the constituent-constituent hard scattering denoted by $\frac{d\hat{\sigma}}{d\hat{t}}$ ($\hat{}$ refers to constituent-constituent variables). Hence the inclusive process

illustrated in Figure 34 is described by the expression

$$E_C \frac{d^3\sigma}{d^3p_C}\left(s, p_T^c, \theta_C^*\right) = \int dx_a \int dx_b \, F_{a/A}(x_a) F_{b/B}(x_b) \frac{1}{\pi} \frac{d\sigma}{d\hat{t}} \frac{D_{C/c}(z_C)}{z_C^2}, \qquad 5$$

where

$$\hat{t} = (q_a - q_c)^2 = -\frac{x_a x_T}{2} s \tan(\theta_C^*/2)/z_C \quad ,$$

$$x_T = 2p_{T_C}/\sqrt{s} \quad ,$$

$$\hat{s} = (q_a + q_b)^2 = x_a x_b s \quad ,$$

and

$$z_C = \frac{1}{2} x_T \frac{\tan(\theta_C^*/2)}{x_b} + \frac{\cot(\theta_C^*/2)}{x_a} \quad .$$

Here θ^* is measured from the direction of hadron A.

It is the choice of the interacting constituents and the specific form of the hard scattering process which distinguishes the various models. Three illustrative cases for the central region in Figure 34 are indicated in Figure 35. The first (Figure 35a) is the basic quark-quark process where a, b and c are all quarks or antiquarks and the functions F and D are in principle available from the lepton data. The basic scattering mechanism is presumably due to the short distance structure of the gluon mediated interaction which confines the quark and is not a priori known in detail. The naive guess of single gluon exchange (2), i.e. p_T^{-4}, has not been observed experimentally.

The second case (Figure 35b) is one of the quark interchange terms in the CIM corresponding to quark-meson scattering with the exchange of a quark-antiquark pair in the $\hat{t}$ channel. This diagram has the virtue of being similar to the set of quark diagrams used successfully in the case of quasi two-body

hadronic reactions in the Regge limit, i.e. there are hadronic quantum numbers in the $\hat{t}$ channel as is not necessary in Figure 35a. The distinctive feature of this term, clear already from Figure 35b, is that the corresponding D function is exceedingly simple (ignore resonance production for now):

$$D_{C/c}(z_c) \sim \delta(1-z_c)\,\delta_{C,c} \qquad 6$$

Although the contribution of this diagram is generally considered to be dominant for meson production at large p_T, there is apparently a large number of distinct terms available to the CIM phenomenologist which makes it necessary to test the model with the results of various experiments simultaneously.

The final example (Figure 35c) is also a possible CIM term but it is special in many ways. It forms the basis of the quark-fusion model of the Cambridge school. Note that in this case the exchanged object in the $\hat{t}$ channel is a single quark. Initially (28) the final state consisted of two mesons with the D functions behaving as δ functions as in Equation 6. More recently (29) the picture has been enlarged to include double mesonic jet (resonance ?) production with a corresponding increase in the complexity of the D function and therefore with increased ability to fit the data.

It is probably helpful here to briefly review the so-called "counting rules" (10) obtained under certain conditions in specific field theory models and which allow one to immediately guess the expected behavior of a specific hard scattering process, as in Figure 35, if these conditions are assumed to be fulfilled. The rule is that a fixed angle hard scattering process behaves as $(\hat{s})^{-n+2}$ where n is the number of participating elementary constituents. Here a constituent meson is composed of two $(q\bar{q})$ elementary constituents. This results in the acceptable prediction of $\hat{s}^{-4}$ for the processes in Figures 35b and 35c but $\hat{s}^{-2}$ for the process in Figure 35a. It is the premise of Feynman and Field (14) that

simple quark-quark scattering in fact violates this rule and for reasons as yet unknown the process in Figure 35a also behaves as $\hat{s}^{-4}$ which translates into p_T^{-8} times a function of x_T and θ for the hadronic reaction (Equation 5).

No attempt will be made here to review the models in further detail. Rather a more global view will be adopted and from this vantage point an attempt will be made to isolate those questions which are most likely to be embarrassing to the various models and therefore informative (irritating ?) to the theorists. For the impatient reader two related and important questions, which should serve to distinguish the two models of central interest simply on the basis of the fundamental differences of Figures 35a and 35b, are immediately specified.

i) What is the ratio of the momentum of the triggering hadron in single particle triggers to the total momentum of the jet (constituent) from which it arose (i.e. what is $\langle z_C \rangle$)?

ii) What is the ratio of the production rate of jets with a certain energy E_T (accumulated, e.g. with a calorimeter type trigger) to the single particle rate with the same E_T?

Of course other experimental measurements are unquestionably important and will help to more thoroughly understand large p_T physics and therefore more closely confine the models. However, the purpose here is to attempt to distinquish between the fundamental structures of the models. It is argued below that most other features of the correlation data, which are independent of these two points, are either common to all hard scattering models or ambiguously addressed in the models (or both).

5. SINGLE PARTICLE CROSS SECTION

Before discussing the correlations in large p_T events in detail, it is useful to first discuss the single particle data, and to set up the formalism to be used

later. As shown in Section 2, the production of all hadrons except protons appears to exhibit a $p_T^{-8}\, f(x_T, \theta)$ behavior. From the assumption that the only dimensional (i.e. nonscaling) quantity in Equation 2 is $d\sigma/d\hat{t}$, one infers that this hard scattering cross section must behave as $1/\hat{s}^4\, f(\theta)$. Furthermore the observed angular dependence of the single particle spectra suggests (14, 33) a number of related specific forms for the hard scattering cross section. The possibilities are $1/(\hat{s}\,\hat{t}^3)$, $1/(\hat{s}\,\hat{u}^3)$, $1/(\hat{t}^2 p_T^4)$ and perhaps even $1/(\hat{s}^2\hat{t}^2)$ though at present data seem to favor $1/(\hat{s}\,\hat{t}^3)$ and/or $1/(\hat{s}\,\hat{u}^3)$. This behavior is the result calculated in the CIM (Figure 35b) for spinor quarks and, as noted above, is assumed for Q-Q model (Figure 35a). Hence the form of the hard scattering cross section is unlikely to create any problem for these two models (although proponents of alternate pictures (28-31) should determine whether it is a reasonable form) and this question will not be discussed further. Likewise the ratio of the production rates of various hadrons is unlikely to be very discerning until detailed comparisons between models and data can be made (34). The dramatic rise of $pp \to \pi^+ X/pp \to \pi^- X$ with transverse momentum is certainly predicted in the Q-Q picture. However, it arises naturally to a greater or lesser extent in all models where quantum numbers are traced via quarks. Note, for example, in Figure 35b the quark of the outgoing meson is exactly the incoming quark from one of the initial hadrons. Thus, just as in Figure 35a, an initial pp state (uud-uud) will tend to produce more π^+'s than π^-'s and one may anticipate that while the data will constrain the models, it will be explained in all such models.

With respect to the observed x_T dependence of the various cross sections (see Tables 1 and 2), the simple counting rules proposed for the CIM (27), whereby one adds the exponents of the (1-x) factors in the F functions plus a $(1-x_T)$ factor for each x integral, provide quite an adequate description of the

results. It should be noted, however, that these rules are really only applicable in the limit $x_T \to 1$. In the region $x_T \lesssim .5$, where one finds the bulk of the data, these rules are of an a priori dubious nature. In this range the distribution functions F are not well described by a single power of (1-x) (as observed in lepton induced processes $F_{q/p}(x)$ has a maximum around $x = 1/3$) and the x dependence of the hard scattering cross section $d\sigma/d\hat{t}$ is of considerable importance. In fact these two effects tend to cancel, leaving the counting result as a good first guess, but detailed calculations are necessary to make a careful test of the model. For the Q-Q model (14) the differences in the $(1-x_T)$ behavior of the various hadrons arise largely from the relative difficulty of producing them from the scattered quark. These differences can be inferred from data on hadron production in lepton interactions and Field and Feynman find good agreement with the large p_T data.

There are a few points, however, concerning single hadron production, which do deserve special attention. One is the apparent difference of the large p_T proton spectrum from all other hadrons (p_T^{-12} instead of p_T^{-8}). This effect is easily accommodated in the CIM (27) by the judicious choice of the dominant diagram for $pp \to pX$. The Q-Q model must seemingly invoke leading particle effects where the observed proton is, in fact, one of the incident protons. The hard scattering proton-quark process thereby involved will behave as p_T^{-12} by the above mentioned counting rules (8 active quarks) or as p_T^{-16} if considered as basically a Q-Q process but including a dipole form factor to describe the proton-proton vertex. Another possibility is to include quark-diquark scattering $\left(\sim p_T^{12}\ ?\right)$ but this is clearly outside the scope of the simple Q-Q model. At the same time proponents of the CIM, with a basic q-meson scattering term, must argue (35) that leading particle effects are small in the

reaction $\pi^+ p \to \pi^0 X$, in order to avoid too large a value for the ratio $\pi^\pm p \to \pi^0 X / pp \to \pi^0 X$. This situation clearly suggests potential difficulties for one of the models and the theorists involved should be pressed to address the problem with more calculations. Likewise, data on the reactions $\pi^\pm p \to \pi^\pm X$ and $\pi^\pm p \to pX$ will be most informative.

6. JET CROSS SECTION

In order to discuss jets, and therefore correlations, it is useful to introduce a notation (23) which is somewhat different from that used above but which focuses attention on the role of the jets. This involves taking certain liberties with the structure of the models, but the deviations are numerically quite small in the region of interest (i.e., $\lesssim 10\%$ for $x_T \lesssim 1/2$) and the simplification is considerable. Define the differential cross section to produce a jet (constituent) with transverse momentum $P_{T_{jet}}$ in the angular region $\theta = 90^\circ \pm 45^\circ$ to be

$$\frac{d\sigma}{dP_{T_{jet}}} \simeq A/P_{T_{jet}}^{n-1} \quad . \tag{7}$$

In the specific models discussed above the right-hand side of this equation would read $P_{T_{jet}}^{-7} f\left(x_{T_{jet}}, \theta^*_{jet}\right)$ and would include the convolution of the initial constituent distributions (the F's) with the hard scattering cross section $(d\sigma/d\hat{t})$. In order to be able to simply perform the integrals in the following analysis it is useful to approximate this complete expression by:

1) ignoring any angular dependence in the region indicated—a reasonable approximation in both the models and the data;
2) parametrizing $f\left(x_{T_{jet}}\right)$ locally as an inverse power of P_T times a function of s alone.

Hence, in principle, A is a function of s while n is a function of p_T and s. As illustrated in Figure 36 it turns out that in the limited region of s and p_T where

data exist, it is possible to set A equal to a constant and consider n as a function of s only. Typical values for n, as indicated in Figure 36, are n=9 at the largest ISR energies and $n \geq 13$ for $p_{lab} \leq 300$ GeV/c. Note that for the specific parametrization suggested earlier, $d\sigma/dp_T(\pi) \sim p_T^{-7}(1-x_T)^9$, one has $n \sim 8+9\,x_T/(1-x_T)$, which is at least approximately constant for any finite range of x_T for $x_T \lesssim 1/2$. To reiterate, while Equation 7 is highly simplified, it does offer a reasonable description of the single particle data and provides enormous simplification and transparency in the following illustrative calculations.

To proceed it is necessary to adopt a specific form for the function $D(z, \bar{k}_T)$ which describes the distribution of hadrons within a jet. As noted earlier the usual picture assumes a distribution which is rapidly cutoff in momentum space in the direction transverse to the jet direction (i.e. in the variable $\bar{k}_T$). The naive expectation is that the quantitative value of this cutoff should be characterized by the behavior observed in normal inelastic events, i.e. a cutoff around 350 MeV/c. This expectation does seem to be born out in the same side correlation data. Since the models are not differentiated by their statements concerning this point, it will not be discussed further except to note that the inclusion of this cutoff structure is an essential feature of any detailed analysis of limited acceptance data. Focusing instead on the longitudinal distribution in the variable z defined earlier, it is useful to introduce the characteristic form for π production

$$D_{\pi/c}(z) = \frac{B^\pi}{z}(1-z)^2 + L^\pi + K^\pi\delta(1-z) \quad . \qquad 8$$

This specific parametrization is not to be considered fundamental, but rather illustrative of various aspects of the models under study. In the limit B^π/K^π and $L^\pi/K^\pi \to 0$, Equation 8 describes a jet containing only a single pion

corresponding to the naive CIM term illustrated in Figure 35b where the observed meson is produced directly in the hard scattering process. The opposite limit, where K^{π} goes to zero while B^{π} and L^{π} remain nonzero, is characteristic of the Q-Q model (Figure 35a) of Feynman and Field (14). More specifically they chose a parametrization of the D functions which gives for a u quark yielding π^+'s plus π^-'s

$$D_{\pi^+/u}(z) + D_{\pi^-/u}(z) \approx \frac{1.4}{z}(1-z)^2 - 0.4\frac{(1-z)^3}{z} + 0.05/z \quad . \qquad 9$$

The L term has a simple interpretation as the contribution of single unpolarized ρ meson production and subsequent decay into two pions, one of which is observed. Hence a simple extension of the naive CIM to include resonance production is to keep both the K^{π} and L^{π} terms and set only B^{π} to zero. Thus by studying the relative roles of the three terms one may determine how the models differ.

Combining Equations 7 and 8, the single pion production cross section at large p_T is given by (ignoring corrections proportional to x_T which are small ($\lesssim$10%) for $x_T \lesssim .5$ and including a factor 2 to account for the two jets in each event)

$$\frac{d\sigma}{dp_{T\pi}} \simeq 2A\int_{P_{T\pi}} \frac{dP}{P^{n-1}} \frac{D_{\pi/c}(p_{T\pi}/P)}{P}$$

$$= \frac{2A}{p_{T\pi}^{n-1}}\left(\frac{2B^{\pi}}{n(n-1)(n-2)} + \frac{L^{\pi}}{n-1} + K^{\pi}\right) \quad . \qquad 10$$

The value of the approximate parametrization of Equation 7 should now be apparent. More importantly this result clearly indicates an effect not widely appreciated until recently (23, 32, 36): a marked trigger bias results from the application of the single particle trigger to a rapidly falling cross section. Even if K^{π} and L^{π} are numerically much smaller than B^{π} and therefore make

a negligible contribution to an unbiased event and the momentum sum rule

$$\sum_h \int y\,dy\; D_{h/c}(y) = \sum_h \left(\frac{B^h}{3} + \frac{L^h}{2} + K^h\right) \equiv 1 \quad , \qquad 11$$

it is still likely that such "quasi-exclusive" terms will dominate the single particle triggers ($n(n-1)(n-2) \gtrsim 100$). The resulting biased event structure is idealized in Figure 37. It arises from the same initial constituent distribution as that shown in Figure 33a and is to be contrasted with the unbiased hadronic distribution of Figure 33b. The role of such "quasi-exclusive" events, in which most of the jet's momentum is concentrated in a single hadron, is reflected in the ratio of the momentum of the jet to the momentum of the triggering particle which arises from the jet. This ratio will be smaller in models where such quasi-exclusive events are relatively more likely. Since the models are to a certain extent tailored to yield the observed shape and magnitude of the single particle cross section, it is only at this internal level that the models begin to make divergent statements. A more direct check will be supplied by the ratio of the cross section for a jet type trigger to the single particle ratio at the same energy. For models where a single hadron with all the momentum is likely ($K >>> B, L$) this ratio approaches unity, while in models, where its momentum to a single hadron ($B >> K, L$), the ratio should be of order n^3. This point will be discussed in more detail below.

In the notation of Equation 9 the ratio between the average jet momentum and the trigger pion momentum is given by

$$\langle P_{jet}\rangle / p_\pi = \frac{\int \frac{dP}{P^{n-1}} \frac{D_{\pi/c}(p_\pi/P)}{P} \cdot \frac{P}{p_\pi}}{\int \frac{dP}{P^{n-1}} \frac{D_{\pi/c}(p_\pi/P)}{P}} = \frac{\frac{2B^\pi}{(n-1)(n-2)(n-3)} + \frac{L^\pi}{n-2} + K^\pi}{\frac{2B^\pi}{n(n-1)(n-2)} + \frac{L^\pi}{n-1} + K^\pi} \qquad 12$$

Hence the ratio is bounded by

$$n/n-3 \geq \frac{\langle p_{jet} \rangle}{p_\pi} \geq 1$$

$$B/K, L/K \to \infty \qquad K/B, K/L \to \infty \quad .$$

While this appears to correspond to a strikingly narrow range, 1.5 to 1 for n=9, the correlation data, particularly on the away side, are very sensitive to this quantity. It appears that the data require a value around 1.1 (23). In the context of the CIM which naively saturates the lower bound in (12) (see Equation 6) this experimental result clearly indicates the presence of direct resonance production in Figure 35b. While this extension is well justified a priori, both theoretically and experimentally (see Figures 20-23), the small (10%) required deviation from the naive ratio of 1 apparently requires a sizeable resonance contribution. For example, including an equal amount of direct π and ρ resonance production in Equation 12, L=K (B=0), leads to a ratio 1.016 for n=9. Resonances more massive than the ρ with higher multiplicity final states will lead to contributions further suppressed by powers of 1/n. Clearly it is very important to study and clarify the role of resonances in the context of the hard scattering models.

This section is closed by speculation on another possible difference between the two pictures. For the particles which are produced relatively rarely at large p_T, e.g. K^-, the present formalism looks rather different in the two models. In the Q-Q model, it is more difficult to make a K^- than a π^+ because $D_{K^-/u,d}(z)$ is more rapidly cut off in z than is $D_{\pi^+/u,d}(z)$. Hence, by arguments similar to those above, one expects that $\langle P_{jet} \rangle / p_{\pi^+}$ for π^+ production is smaller than $\langle P_{jet} \rangle / p_{K^-}$ for K^- production. In the CIM model it is more difficult to produce a K^- than a π^+ from protons simply because one is less likely to find a

virtual K^- or K^o within a proton than to find a virtual π^+ or π^o. In the present language this corresponds to a larger value of n but no change in the ratio $\langle P_{jet}\rangle/p_{trigger}$ from K^- to π^+ if single hadron production dominates. Since the cross section for production of K^- is much smaller than that for K^+, the effects of ϕ resonance production presumably do not dominate. In any case, since $\langle P_{jet}\rangle/p_{trigger}$ is measurable through the correlations discussed below, it will be interesting to study the differences in the correlations for K^- versus π^+ triggers.

7. SAME SIDE CORRELATIONS

The most global same side correlation is just the behavior of the associated multiplicity in the same hemisphere as the triggering particle. In any model with $\langle P_{jet}\rangle/p_\pi > 1$ one expects an associated multiplicity within the jet which increases with the p_T of the trigger, while for single meson or resonance production ($\langle P_{jet}\rangle \sim p_\pi$) one anticipates a small, fixed associated multiplicity. In order to study this effect in the data one must presumably first remove those particles which are associated with the background low p_T physics. This is generally accomplished by subtracting from the multiplicity observed in large p_T events the multiplicity seen in corresponding inelastic but all low p_T events. However, even this procedure is not free of ambiguity (37). Just as there is a nonzero transverse dimension to the distribution of hadrons within a jet, one expects a finite transverse width in the distribution of constituents within the incident hadrons (38). This situation leads to a new type of trigger bias. By selecting events with a large p_T particle in one direction one is preferentially selecting events where the hard scattering constituents initially had their p_T in the trigger direction. Hence one is choosing those events where the cloud of background low p_T hadrons have a total p_T in the direction opposite to the trigger.

This is illustrated schematically in Figure 38 where a is the initial, biased constituent distribution and b shows the resulting hadrons distribution. Note in particular the depleted associated low p_T multiplicity in the trigger hemisphere which may obscure the effect of any possible increase of the multiplicity within the towards jet. Hence global same side associated multiplicity measurements are fairly difficult to interpret without a more complete model which includes also the p_T distribution of constituents within the initial hadrons and accounts for the effect of this distribution on the low p_T cloud. Note, however, that one can precisely discuss the associated multiplicity of hadrons with momentum greater than some $p_0 >> 300$ MeV/c such that they are all associated with the jet and not to be confused with the background (32).

A quantity which is better defined theoretically, though perhaps not uniquely predicted by the models, is the cross section for the production of two large p_T particles in the same hemisphere. In the context of a jet picture both particles are members of the same jet and are therefore well collimated in momentum space. This does indeed seem to be the case as shown earlier in Figure 19 and provides the best determination of the jet radius. The distribution along the jet axis is defined by a new function $D^2_{h_1 h_2/c}(z_1, z_2)$ which again must satisfy a momentum sum rule

$$\sum_{h_2} \int_0^{1-z_1} dz_2 z_2 D^2_{h_1 h_2/c}(z_1, z_2) = (1-z_1) D_{h_1/c}(z_1) \quad . \qquad 13$$

A likely candidate for the structure of D^2 is

$$D^2_{h_1 h_2/c}(z_1, z_2) = \frac{C^{h_1 h_2}}{z_1 z_2}(1-z_1-z_2)^2 + J^{h_1 h_2}(1-z_1-z_2) \qquad 14$$

where Equations 13 and 8 imply the relations

$$\sum_{h_2} C^{\pi h_2} = 3B^{\pi} \quad \text{and} \quad \sum_{h_2} J^{\pi h_2} = L^{\pi} \quad . \qquad 15$$

Again the latter term corresponds, where applicable, to the production of resonances with two body decays (i.e. does not apply to the $\pi^{\pm}_{o}\pi^{\pm}_{o}$ data). Note in particular that $D^2(z_1, z_2)$, as a function of z_1+z_2 is very similar in functional form to D(z). This leads to the result that the two particle, same side cross section is essentially proportional to the single particle cross section evaluated at the total $p_T=p_{T_1}+p_{T_2}$ (23). This statement applies to the shape and s dependence of the two particle cross section and, to first approximation, also to the magnitude. Furthermore this ansatz also leads to the expectation that the two particle cross section is primarily a function of $p_{T_1}+p_{T_2}$ and only weakly dependent on $p_{T_1}-p_{T_2}$. These general results are sufficient to understand, at least qualitatively, all the observed features of the same side two particle correlations.

In order to perform detailed comparisons with the data, one must include in the jet distribution also the transverse distribution. A typical form would be (using the notation of Equation 4)

$$dP_{C/c} = D_{C/c}(z)\, dz\, e^{-\bar{k}^2/\lambda^2} \frac{d^2\bar{k}}{\pi\lambda^2} \qquad 16$$

where, as mentioned earlier, the cutoff parameter λ is best determined by this same side data. This transverse distribution will play a major role in a description of data taken with the (typically) small same side acceptance. While the study of this transverse distribution in the same side data is certainly an important question, it is unlikely to differentiate between the models. As discussed earlier, a question of more immediate interest to the models is the role of

resonances. This is particularly the case since it is already known that the same side correlations are not given entirely by two body resonances. One may even expect that, as the CIM is enlarged to include the direct production of more massive resonances and the jets in the Q-Q picture are generalized to include coherent resonance effects, the two pictures will tend to merge—a not totally unattractive possibility. Clearly this is an area needing further study.

Another interesting question is the structure of the trigger bias for a two hadron trigger. The similarity of the single and two particle cross section suggests that the quantity $\langle P_{jet} \rangle / p_{T_1} + p_{T_2}$ will be bounded by n/n-3 and 1 as in Equation 12. If the "quasi-exclusive" effects which kept the single particle trigger result near the lower bound have no analogue in higher mass resonances, then triggers like $\pi^+\pi^+$ should lead to values closer to the upper bound. This will be interesting to test by studying, for example, the away side multiplicity in two particle trigger events.

A final point concerning the towards side is the question of quantum number conservation. In a Q-Q picture with only a small contribution from strange quarks in the initial state, one anticipates that strangeness will be conserved within the large p_T jet. In practice this means nearby in rapidity and in the same azimuthal hemisphere but not necessarily at a similar p_T. For the CIM the extra strangeness is presumably left in the low p_T cloud (except for resonance production as in $\phi \rightarrow K\bar{K}$).

8. AWAY SIDE CORRELATIONS

The interesting feature of the structure of the away side correlations is that in both the Q-Q picture and in the CIM one expects unbiased jets similar to those observed in lepton induced reactions. (This comment does not obviously apply to the quark-fusion picture of Figure 35c.) The major difference in hadronic

reactions is that, whereas in lepton induced reactions (ep or νp) one knows the momentum which is imparted to the constituent, in the hadronic case the constituent momentum is smeared over a large range of values. In order to differentiate the models it is again necessary to consider the question of the ratio of jet momentum (presumed to be essentially equal to the momentum in the away side jet) to the triggering hadron momentum.

In the notation used in previous sections, the two particle cross section takes the form $\left(z=\vec{p}_2\cdot\vec{p}_1/|\vec{p}_1|^2 \leq 1\right)$

$$\left.\frac{d\sigma^{h_1h_2}}{dp_{T_1}dp_{T_2}}\right|_{away} \approx 2A\int\frac{dP}{P^2}\frac{1}{P^{n-1}}D_{h_1/c}\left(\frac{p_{T_1}}{P}\right)D_{h_2/d}\left(\frac{p_{T_2}}{P}\right) \quad . \qquad 17$$

In the most naive interpretation of the CIM where quark-meson scattering dominates (Figure 35b), one expects the trigger side jet to contain essentially one hadron (K^{h_1} dominates) while the opposite side jet, which arises from the scattered quark, is a more "normal" multiparticle jet ($K^{h_2}=0$). In the notation being used here this picture yields a normalized away distribution of the form

$$\left.\frac{dN}{dz}\right|_{CIM} \equiv \frac{p_1 d\sigma/dp_1dp_2}{\frac{d\sigma}{dp_2}} \simeq \frac{B^{h_2}}{z}(1-z)^2 + L^{h_2} \quad . \qquad 18$$

In the absence of the quasi-exclusive term L^{h_2} this expression will vanish at z=1 in contradiction with the data. More generally, the overall normalization of this expression tends to be well below the observed correlation. This is easily understood, since in this quasi-exclusive limit the jet momentum is minimized ($P_{jet}/p_{trigger}=1$). Hence the momentum to be conserved on the away side is minimized and it is relatively unlikely to find an energetic particle. This effect is illustrated in Figure 39 where the data of the CERN group (21) are compared to the two extreme limits $K^{h_1} >> L^{h_1}, B^{h_1}$ and $B^{h_1} >> L^{h_1}, K^{h_1}$.

The limit where multiparticle final states dominate both jets ($B^h >> L^h, K^h$) can be taken as characteristic of the Q-Q scattering picture. This leads to an away distribution of the form

$$\left.\frac{dN}{dz}\right|_{Q-Q} = \frac{B^{h_2}}{2}\left[1 - 2\frac{n-2}{n+1}z + z^2\frac{(n-1)(n-2)}{(n+1)(n+2)}\right] \quad . \qquad 19$$

For the case n=9 the factor in the square brackets is well approximated by $(1-0.7z)^2$. In any case this limiting form tends to have a normalization larger than the data (recall B^h is normalized via the appropriate momentum sum rule) as evidenced in Figure 39. It is clear that some intermediate choice of the parameters B, K and L will result in a satisfactory description of the data as shown by the solid curve corresponding to the values in Reference (23). At the same time this is a likely place to find results which will differentiate between the various specific models. Again the reader is forewarned that detailed analyses will require knowledge both about the transverse structure within a jet and the transverse distribution of constituents within the initial hadrons. In particular this latter distribution, via its role in the trigger bias distortion illustrated in Figure 38, can effect the normalization of dN/dz. The point is that, while the single particle distribution is sensitive to this distortion, as in Figure 38, the back-to-back two particle cross section chooses a more symmetric configuration. Hence dN/dz, which depends on the ratio of these two cross sections, is also sensitive to the initial wave function distribution. Increasing the average p_T in the incident hadron wave functions will lead to a relative increase in the single particle cross section and a decrease in dN/dz (33).

Other important questions include those of scaling (recall Figure 32) in the various variables. To the extent that the various n dependent factors in Equation 19 $\left(\text{e.g. } \frac{n-2}{n+1}\right)$ are insensitive to small changes in n, the quantity dN/dz

should depend only on z and not on s, p_{1_T} or p_{2_T} individually. Also, calculations (32) indicate that in events containing hadrons with equal and opposite large p_T the average jet momentum is considerably larger than for a single hadron trigger at the same trigger momentum. This should lead to a larger associated multiplicity and to a softening of the quantum number correlations between the two trigger particles. This latter point is a result of the fact that since each of the hadrons may be carrying less than 60% of their respective jet's momentum, their quantum numbers may not be tightly correlated to that of the initial constituents.

Finally one may study the associated multiples where, as above, the best defined theoretically quantity is the associated multiplicity of hadrons with $p_T > p_0$. For p_0 sufficiently large one is discussing only hadrons associated with the jet independent of the low p_T background

$$\langle n(p_T, p_0)\rangle_{jet} = \sum_h \int_{p_0/p}^{1} dz\, D_{h/c}(z) \qquad 20$$

With the parameters of Reference (23), this formalism seems to offer a quite acceptable description of the data (32, 39). To study the global away side multiplicity one should include the trigger bias effects on the background low p_T physics which, as discussed earlier, tend to over-populate the away side.

9. JET TRIGGER

Since data will soon be available on inclusive calorimeter triggers, it is of interest to determine what the various models say about this prospect. This discussion will ignore the difficult experimental problems inherent in defining a jet and proceed as if calorimeter triggers correspond exactly to a jet in the theoretical sense, i.e., the set of hadrons which result from the evolution of a scattered constituent.

In the naive CIM one expects the cross section for large p_T jets to be about 10 times greater than the corresponding cross section for large p_T single particle at the same energy. The simple quark-meson scattering term (Figure 35b) gives approximately equal jet and single meson cross sections. The inclusive jet trigger, however, includes also the single particle triggers. Summing over the various types of single hadrons (assumed to be ~4 times the π^o signal) one finds a total ratio of jets to π^o's of about 10 as illustrated in Figure 40. This result is to be contrasted with the corresponding ratio in the quark-quark scattering model of Feynman and Field, where it is assumed that it is fairly difficult to find a large fraction of a jet's momentum in a single hadron. The resulting ratio of jet to single hadron trigger cross sections turns out to be greater than 100.

Unfortunately this contrast between the two models is almost certainly an oversimplification. The correlation data discussed above speak strongly in favor of the important role of resonance production within the context of the CIM. To the extent that the single meson in Figure 35b is replaced by a summation of resonances, each of which is relatively unlikely to give all of its momentum to a single hadron in its decay one may expect an increased ratio of inclusive jet to single particle cross sections. At the same time this summation of resonances is apt to result in a distribution of hadrons which looks remarkably similar to that in one of the quark initiated jets of the Q-Q picture. Hence one may be faced one day with the almost philosophical question as to which is the more appropriate language: quark-quark or quark-sum of resonances. More generally one may expect that in their attempts to explain the same data the models will gradually evolve toward a common descendant.

There is of course another possible picture which in a sense is already an interpolation midway between the two models discussed above. The general idea (40) is that the basic hard scattering process exhibits the canonical (i.e. dimensional) p_T^{-4} behavior, as in the early, naive Q-Q models, and that the observed p_T^{-8} behavior is an artifact of the single hadron trigger bias. As demonstrated earlier in the context of a general jet model, this trigger bias selects those very rare events where essentially all of the jet's momentum is carried by a single hadron. In the quark language this corresponds to the case where an energetic quark succeeds in picking up a slow antiquark to become a single meson. It is perhaps not surprising that such a process should contain an explicit scale, i.e. the size of the meson, and hence not exhibit the naive dimensional scaling behavior (p_T^{-4}). More explicitly one can attempt to relate the part of the meson's wave function relevant here, i.e. where one of the meson's valence quarks (antiquarks) carries essentially all of its momentum, to the determination of the meson's electromagnetic form factor which is thought to involve precisely the same piece of the wave function. If the form factor behaves as $(q^2)^{-1}$ and since this term is squared in the cross section, it is easy to imagine (if difficult to prove rigorously) that an extra factor of p_T^{-4} is present for these special events. This explanation of the p_T^{-8} behavior is, in fact, not totally distinct from the concepts central to the CIM. The scenario is then that large p_T events which scale as p_T^{-4} are indeed present but are discriminated against by the single particle trigger bias and the special events with p_T^{-8} behavior dominate these triggers at present energies (41). It should be noted that the similarity between the nonresonant same side two particle data and the single particle data and the dissimilarity between the $\bar{p}$ and p data creates problems for such a picture. However this picture does suggest that the unbiased jet

triggers will exhibit naive p_T^{-4} behavior in contrast to the other models discussed and this should be straight forward to test in the near future. The broad band in Figure 40 illustrates the "expected" range of the jet to single trigger ratio in such a picture (for $s \sim 400$ GeV/c^2). Note the dramatic $p_T(x_T)$ dependence. The curve labeled "p_T^{-4} upper limit" would result if both the jet and the single triggers were already exhibiting p_T^{-4} behavior so that an experimental ratio well above this line would rule out such a picture. Note that this limit is still below that of the p_T^{-8} Q-Q model (due to the larger n value in the latter model). In any case the utilization of jet triggers, including data on correlations, should provide a most informative arena for new studies. At the least the rates will be higher and at the most one will be able to directly study the behavior of the short distance constituent-constituent interactions (2) which is accessible no where else.

10. REVIEW

In conclusion the most important questions which one can hope will be resolved experimentally and understood in terms of the models in the near future are:

1) Is there a scaling of the particle distribution inside the jet? Scaling properties are inherent to all constituent models and the doubts raised by the preliminary data of the CCHK Collaboration (25; see Section 3) should be further studied experimentally at higher values of transverse momentum in large acceptance experiments.

2) Do the models successfully explain the observed correlation data a) How do the multiplicities behave in detail both experimentally and in the models? b) Is dN/dz a function of z only, e.g. is it independent of the emission angle and p_T?

c) Can both the CIM and Q-Q models be formulated to agree with the observed form of dN/dz?

3) What is the role of resonances within jets? Here the CIM has rather strong constraints especially for the "towards" jet.

4) How does the jet cross section behave, i.e. how does it depend on transverse momentum and energy? What are the decay properties of the jet? The ratio of jet/single hadron triggers as function of E_T and s should help considerably to distinguish between the models.

There are also several experimental questions which address themselves directly to the details of particular models, e.g. is the steep decrease of the proton large p_T spectrum observed also in other than pp collisions? Are the data from meson-proton collisions compatible with the models? Large acceptance experiments with good particle identification will help in answering interesting question concerning how the various quantum numbers are conserved. In a purely quark-quark interaction picture one expects, e.g. strangeness to be conserved inside the jet, while in the CIM model the quantum numbers may be conserved globally, i.e. including the low p_T cloud. Finally there remains the question of understanding the basic quark-quark interaction. In particular, is p_T^{-4} dynamics lurking just beyond the horizon?

It is the hope of the authors that these questions and the preceding review will succeed in stimulating their experimental and theoretical colleagues to find the answers.

Acknowledgments

We wish to thank our many colleagues for their helpful comments and discussions. Special acknowledgment goes to R. Blankenbecler, S. Brodsky, W. Dunwoodie, J. Gunion, J. D. Bjorken, R. P. Feynman, G. C. Fox, R. D. Field, H. Frisch, R. Hwa and P. Mockett. We also wish to thank the staff at SLAC and especially H. Miettinen for organizing the meeting which is reviewed herein. S.D.E. would like to acknowledge the hospitality of the SLAC theory group during the period when much of this paper was written.

Literature Cited

1. Alper, B. et al 1973. Phys. Lett. 44B:521

Banner, M. et al 1973. Phys. Lett. 44B:537

Büsser, F. W. et al 1973. Phys. Lett. 46B:471

2. Berman, S. M., Bjorken, J. D. and Kogut, J. B. 1971. Phys. Rev. D4:3388

Ellis, D. S. and Kislinger, M. B. 1974. Phys. Rev. D9:2027

For additional references see Sivers, D., Brodsky, S. and Blankenbecler, R. 1976. Phys. Report C23

3. Darriulat, P. 1976. Rapporteur's talks at the International Conference on High Energy Physics, Palermo, 1975.

Della Negra, M. 1976. Invited talk at the VII Colloquium on Multiparticle Reactions, Tutzing, 1976.

4. Büsser, F. W. et al 1976. Nucl. Phys. B106:1

5. Alper, B. et al 1975. Nucl. Phys. B100:237

6. Antreasyan, D. et al 1977. Phys. Rev. Lett. 38:112

7. Eggert, K. et al 1975. Nucl. Phys. B98:73

8. Donaldson, G. et al 1976. Phys. Rev. Lett. 36:1110

9. Chicago-Princeton Collaboration, Frisch, H. private communication.

10. Brodsky, S. J. and Farrar, G. 1973. Phys. Rev. Lett. 31:1153

Brodsky, S. J. and Farrar, G. 1975. Phys. Rev. D11:1304

Matveev, V., Muradyan, R. and Tavkhelidze, A. 1973. Nuovo Cimento Lett. 7:719

11. Cronin, J. W. et al 1975. Phys. Rev. D11:3105

12. Taylor, F. E. et al 1976. Phys. Rev. D14:1217

13. Antreasyan, D. et al 1977. Phys. Rev. Lett. 38:115

14. Field, R. D. and Feynman, R. P. 1968. Quark elastic scattering as a source of high transverse momentum mesons. Preprint CALT-68-568, California Institute of Technology.

15. Ellis, S. D. and Thun, R. 1974. Proceedings of the IX Recontre de Moriond. Tran Thanh van, editor.

16. Alper, B. et al 1976. Nucl. Phys. B11:1

17. Della Negra, M. et al 1976. Preprint CERN/EP/PHYS 76-43, CERN.

18. Della Negra, M. et al 1975. Phys. Lett. B59:401

19. Møller, R. 1976. British-French-Scandinavian Collaboration, preliminary results presented at the VII Colloquium on Multiparticle Reactions, Tutzing, 1976.

20. Eggert, K. et al 1975. Nucl. Phys. B98:49

21. Darriulat, P. et al 1976. Nucl. Phys. B107:429

22. Della Negra, M. et al 1976. Preprint CERN/PHYS. 76-35, CERN.

23. Ellis, S. D., Jacob, M. and Landshoff, P. V. 1976. Nucl. Phys. B108:93

24. Kephart, R. et al 1976. Phys. Rev. D14:2909

25. Sosnowski, R. 1976. Invited talk at the International Conference on High Energy Physics, Tblisi, 1976. Preprint EP/PHYS 76-56, CERN.

26. For a review of the models and theoretical ideas see the last reference in Reference (2) above.

27. Blankenbecler, R., Brodsky, S. J. and Gunion, J. 1975. Phys. Rev. D12:3469 and references therein.

28. Landshoff, P. V. and Polkinghorne, J. C. (1973). Phys. Rev. D8:4157

29. Landshoff, P. V. 1976. Review talk at the VII Colloquium on Multiparticle Reactions, Tutzing, 1976 (CERN preprint TH-2227).

Landshoff, P. V. 1976. Proceedings of the XI Rencontre de Moriond, 1976. See also Combridge, B. L. 1976. Preprint 76/1, Cambridge.

30. Preparata, G. 1974. Nucl. Phys. B80:299

31. Hwa, R. C., Spiessbach, A. J. and Teper, M. J., Phys. Rev. Lett. 36:1418

Fishbach, E. and Look, G. W. 1976. Purdue University preprint.

Contagouris, A. P. and Gasket, R. 1976. Preprint.

32. Jacob, M. and Landshoff, P. V. 1976. Preprint TH-2182, CERN.

33. Furmanski, W. and Wosiek, J. 1976. Preprint TPJU-8/76, Cracow.

Baier, R., Cleymans, J., Kinoshita, K. and Peterson, B. 1976. Preprint B1-TP 76/25, University of Bielefeld.

34. A detailed analysis of the CIM has been performed by Raitio, R. O. and Ringland, G. A. 1976. Phys. Rev. D14:2241

35. Brodsky, S. J. and Gunion, J. F. 1976. Preprint SLAC-PUB-1806, Stanford Linear Accelerator Center.

36. For some of the earliest work on jets and trigger bias effects see Bjorken, J. D. 1975. Lectures at the 1975 SLAC Summer Institute.

37. Combridge, B. L. 1975. Phys. Rev. D12:2893

38. There are indeed indications from the lepton pair production in hadronic reactions and their description via the Drell-Yan mechanism, that the participating partons carry sizeable transverse momentum. See e.g. Duong-van, Minh 1975, 1976. Preprints SLAC-PUB-1604, SLAC-PUB-1819, Stanford Linear Accelerator Center.

39. Abad, J., Oruz, A. and Alonso, J. L. 1976. Preprint TH 2213, CERN.

40. Ellis, S. D. 1974. Phys. Lett. 49B:183

41. Estimates of the absolute size of the p_T^{-4} one gluon exchange contribution to the cross section in fact do suggest a value below observed cross section.

42. Büsser, F. W. et al 1976. Phys. Lett. 61B:309

Table 1 Compilation of parameters fitted to formulae 1-3.

Reaction	N	M^2	F	Collaboration	Reference
	8.60±0.04			CCRS	4
$pp \rightarrow \pi^+$	7.70±0.12	0.74±0.02	11.0±0.7	BS	5
	8.2 ±0.5		9.0±0.5	CP	6
	8.60±0.04			CCRS	4
$pp \rightarrow \pi^-$	7.78±0.14	0.79±0.02	11.9±0.7	BS	5
	8.5 ±0.5		9.9±0.5	CP	6
	8.60±0.04			CCRS	4
$pp \rightarrow \pi^o$	7.2 ±0.2			ACHM	7
	10.8 ±0.4	2.3 ±0.3	7.1±0.4	BNL-CIT-LBL	8
$pp \rightarrow K^+$	8.72±0.30	1.69±0.05	9.0±1.0	BS	5
	8.4		8.8	CP	9
$pp \rightarrow K^-$	8.76±0.36	1.77±0.10	12.2±1.1	BS	5
	8.9		11.7	CP	9
$pp \rightarrow p$	10.38±0.34	1.82±0.07	7.3±0.9	BS	5
	11.7		6.8	CP	9
$pp \rightarrow \bar{p}$	9.1 ±0.3	1.17±0.06	14.0±1.4	BS	5
	8.8 ±		8.0	CP	9
$\pi^+ p \rightarrow \pi^o$	10.0 ±0.2	1.8 ±0.2	5.5±0.3	BNL-CIT-LBL	8

Table 2 Fits to the parametrization $p_T^{-N}(1-x_T)^F$ for the particle ratios in the Chicago-Princeton experiment (13).

R	N	F
p/π^+	3.26 ± 1.50	-1.67 ± 1.00
$\bar{p}/\pi^+$	0.27 ± 1.70	4.29 ± 1.90
K^+/π^-	0.20 ± 0.50	-0.68 ± 0.40
K^-/π^-	1.58 ± 1.40	1.59 ± 1.20

Figure Captions

1. Invariant cross section for π^o production at 90^o for five center-of-mass energies. The extrapolation from data with $p_T < 1$ GeV/c is shown for comparison (Reference (4)).
2. Plot of the quantity $p_T^{8.6}\ E(d^3\sigma/dp^3)$ for π^+, π^- and π^o production as a function of $x_T = 2p_T/\sqrt{s}$ (4).
3. The power α in the atomic number dependence versus p_T for π^+ and π^-. The lines are drawn to guide the eye (9).
4. The π^o invariant cross section $E(d^3\sigma/dp^3)$ for constant x_R or $x_{\|}$ and constant values of p_T versus $\sqrt{s}$ (12).
5. The π^+/π^- ratio versus x_T for p-p and p-"n" collisions at 200, 300, and 400 GeV (6).
6. The particle ratios versus p_T for 200, 300, and 400 GeV p-p collisions (13).
7. Particle-antiparticle ratios for 300 GeV p-p collisions extracted from Chicago-Princeton data (6, 13). $\Lambda/\bar{\Lambda}$ point from Reference (42).
8. The product of p_T^n and the particle ratio versus $(1-x_T)$, where n is the corresponding best fit value for $x_T > 0.35$ (13).
9. Ratio of invariant cross section for π^o production with π^+, π^- and p beams at 100 and 200 GeV/c (8).
10. Ratio of invariant cross sections versus x_T for $pp \rightarrow \pi^o X$ and $\pi^- p \rightarrow \pi^o X$ at 100 and 200 GeV/c (8).
11. Schematic description of the kinematical regions used in the study of large p_T events.
12. Charged particle densities for the π^o trigger at 90^o data, averaged over events with p_T of the $\pi^o > 2$ GeV/c. The solid lines give charged particle densities in minimum bias triggers (20).

13. The p_T dependence of the multiplicity for the π^+, K^- and p triggers in various azimuthal regions: Φ_1 is the towards region, Φ_5 is the away region (16).

14. Rapidity distribution of negative secondaries in the a "towards" azimuthal angle and b "away" azimuthal angle for the 20^o and 45^o positive triggers. Full line indicates the respective distribution of normal events. The vertical scale is the charged multiplicity, times 100, per interval of $\Delta\phi$ and Δy (in radian^{-1}) (17).

15. Same as Figure 14 but for positive trigger and positive secondaries (17).

16. Percentage of events with leading particles as a function of the transverse momentum of the large p_T secondary. Data from References (18) and (19).

17. Invariant density of positive leading particles with $p_T > 0.2$ GeV/c as a function of x in normal events (thin line) and in large p_T events (thick line) (18).

18. The rapidity distribution of negative secondaries in the towards region for the events with 45^o positive particle with $p_T > 2$ GeV/c. The full line represents the equivalent distribution for normal events (22).

19. The transverse momentum squared distribution with respect to the jet axis of particles forming the jet (22).

20. Rapidity distributions and π^o-$\pi^\pm$ mass distributions for particles in the large p_T π^o hemisphere with $|\phi| \leq 27^o$. The mass distributions are plotted for $|y| \leq 2$. The dashed curves show the minimum bias rapidity distributions and the mass spectra expected for uncorrelated particles (21).

21. The $\pi^o\pi^+$ mass distribution in the towards region for large p_T π^o events. The dashed line is the mass distribution for uncorrelated particles and the dashed-dotted line represents assumed background (21).

22. a The $\pi^+\pi^-$ invariant mass distribution for π^- trigger at 20^o with $p_T(\pi^-) > 1.5$ GeV/c. An estimation of the ρ^o signal is shown corresponding to $\rho^o/\pi^- = 1.2$. b Same as a with the ρ^o removed. c Monte Carlo estimation of the minimum bias background under the ρ^o signal (CCHK data, Reference (3)).

23. a Neutral and doubly charged invariant $(\pi\pi)$, $(K\pi)$ and $(p\pi)$ mass spectra including large p_T ($p_T > 2$ GeV/c) identified triggering particle. b Difference between neutral and doubly charged mass spectra indicating production of resonances (19).

24. Rapidity distribution of secondaries with $p_T > 1$ GeV/c in the events with large p_T trigger at y=0. P_w is the p_T of the trigger (19).

25. Azimuth distribution of charged particles in the away region in the events with large p_T π^o emitted at 90^o (21).

26. Distributions of $|p_{out}|$ for different intervals of transverse momentum p_x of the charged particles. The dashed lines correspond to a function $dN/d|p_{out}| \sim \exp(-2|p_{out}|)$ (21).

27. Charged particle densities for the π^o trigger at 53^o. The solid lines give charged particle densities for minimum bias trigger (20).

28. Rapidity distribution of large p_T charged secondaries ($p_T > 0.8$ GeV/c) from events in which the largest x_T particle denoted here as X_E is within rapidity intervals: a $0 \leq y \leq 0.75$, b $0.75 \leq y \leq 1.5$. The particle with the largest x_T is not included in the plot (21).

29. The distribution of rapidity difference of pairs of particles in the away region (full line). Also shown is the equivalent distribution for uncorrelated pairs. c and d show normalized rapidity difference distributions obtained by taking the ratio of the distributions of a and b respectively to the background distributions of these figures (22).

30. Contour lines for the correlation function

$$C(y_1, y_2) = \rho^2(y_1, y_2) - \rho^1(y_1)\,\rho^1(y_2)$$

for particle pairs of opposite charge in the away region. ρ^2 and ρ^1 denote two- and one-particle density distributions, respectively (22).

31. Comparison of x_T distributions for e^+e^-, ep data with corresponding distribution in away region in the events with a large p_T π^o produced in pp collisions (21).

32. The distribution of the number of secondaries per event emitted in the away direction versus the reduced transverse momentum x_T. The three sets of points correspond to three values of p_T of the triggering particle. Only particles with momentum component perpendicular to the trigger plane smaller than 0.6 GeV/c are plotted (25).

33. Pictorial representation of the two step development of large p_T events in constituent hard scattering models. Illustrated are the distributions in momentum space of a the constituents immediately following the hard scattering (open circles) and b the final hadrons (full dots).

34. Pictorial representation of the structure of a large p_T event in terms of the constituents.

35. Pictorial representation of three specific constituent hard scattering processes: a quark+quark → quark+quark, b quark+meson → quark+meson, c quark+antiquark → meson+meson.

36. Plot from Reference (23) indicating the feasibility of parametrizing the single particle data as a fixed power, p_T^{-n}, at a fixed s value.

37. Pictorial representation of the distorted momentum space distribution due to the single hadron trigger bias.

38. Pictorial representation of the distorted momentum space distribution of a the constituents immediately after the hard scattering (open circles) and b the final hadrons (full dots) resulting from the trigger bias coupled with the p_T distribution of the constituents in the initial hadrons.

39. Away side correlation, dN/dz, in the data of Reference 21 compared to the calculated results for the two extreme limits discussed in the text and the parameters of Reference (23) (solid line).

40. Predicted values of the ratio of jet cross section to single hadron cross section in various models discussed in the text. The calculations shown are for pp interactions.

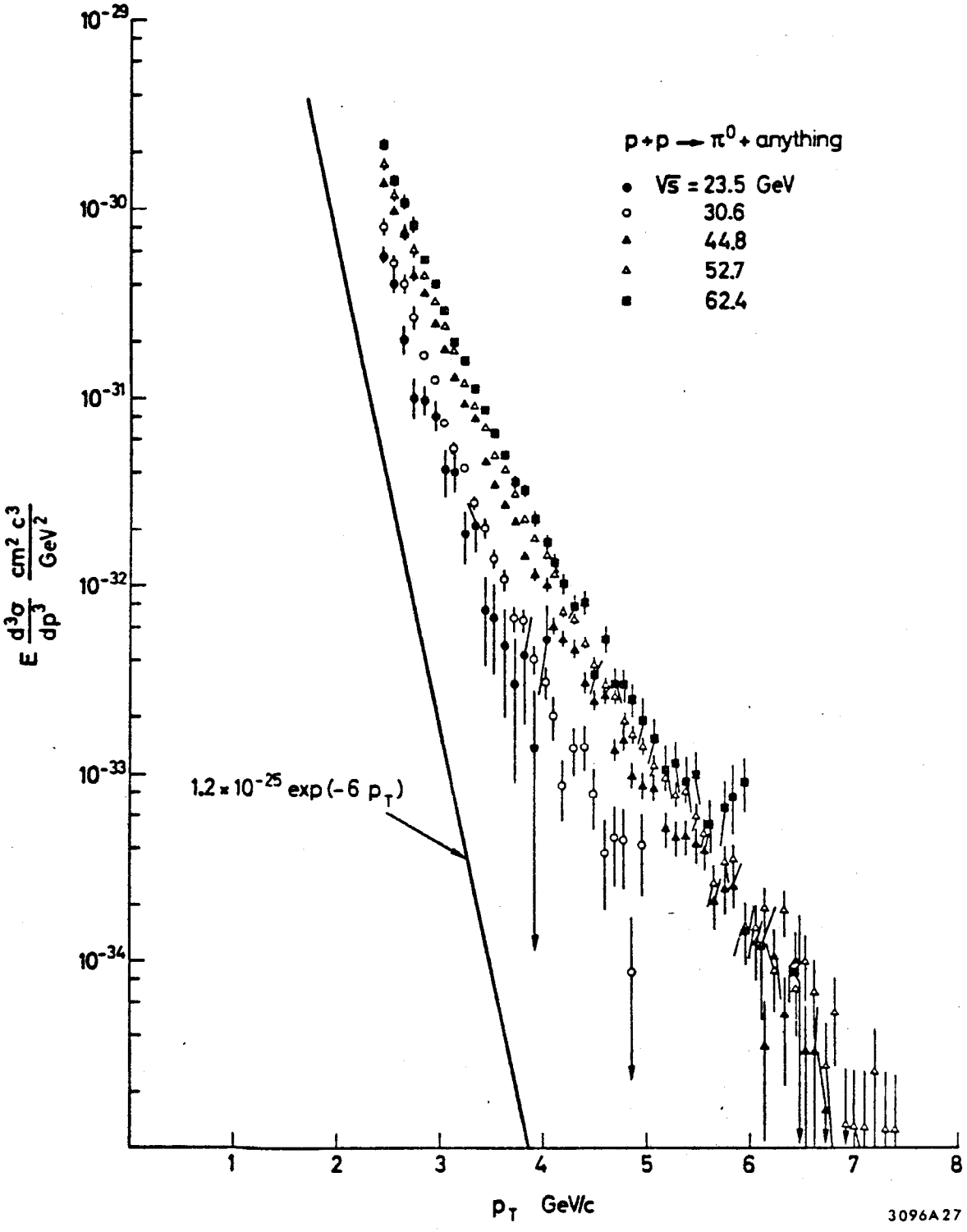
10^{-29}
10^{-30}
10^{-31}
10^{-32}
10^{-33}
10^{-34}
$E\frac{d^3\sigma}{dp^3}\frac{cm^2\,c^3}{GeV^2}$
$p+p \rightarrow \pi^0 + anything$
$\sqrt{s}$ = 23.5 GeV
30.6
44.8
52.7
62.4
$1.2 \times 10^{-25} \exp(-6\ p_T)$
1
2
3
4
5
6
7
8
p_T GeV/c
3096A27

Fig. 1

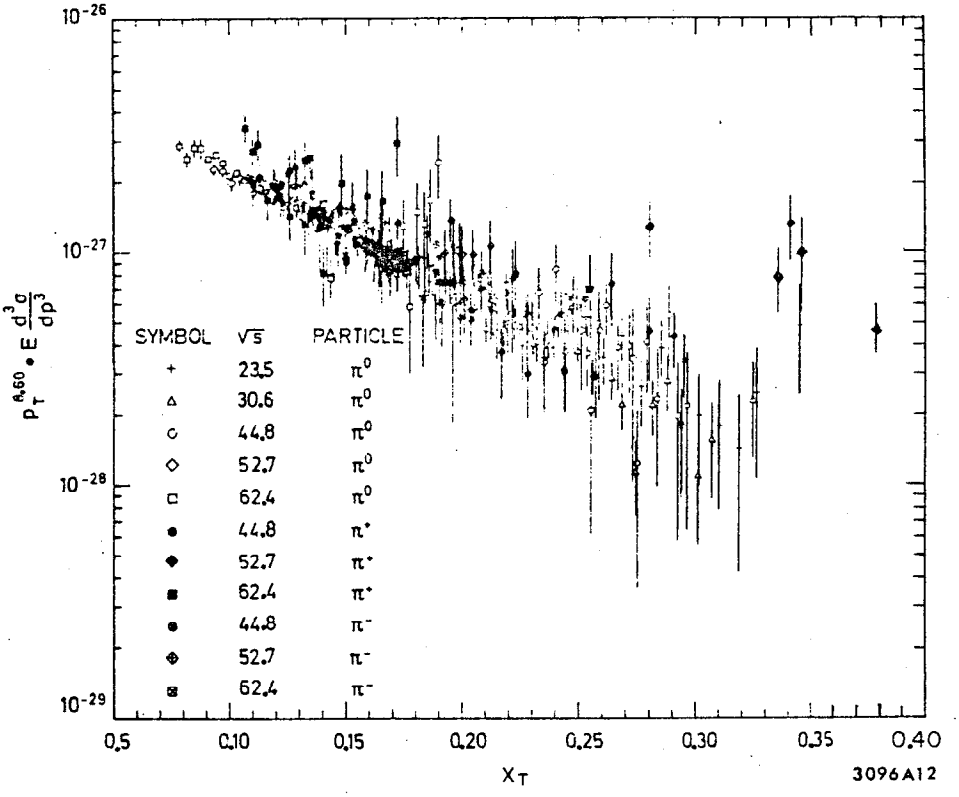
10^{-26}
10^{-27}
10^{-28}
10^{-29}
$p_T^{6.60} \cdot E \frac{d^3\sigma}{dp^3}$
SYMBOL
$\sqrt{s}$
PARTICLE
+ 23.5 π^0
△ 30.6 π^0
○ 44.8 π^0
◇ 52.7 π^0
□ 62.4 π^0
● 44.8 π^+
◆ 52.7 π^+
■ 62.4 π^+
● 44.8 π^-
◈ 52.7 π^-
⊠ 62.4 π^-
0.5
0.10
0.15
0.20
0.25
0.30
0.35
0.40
X_T
3096A12

Fig. 2

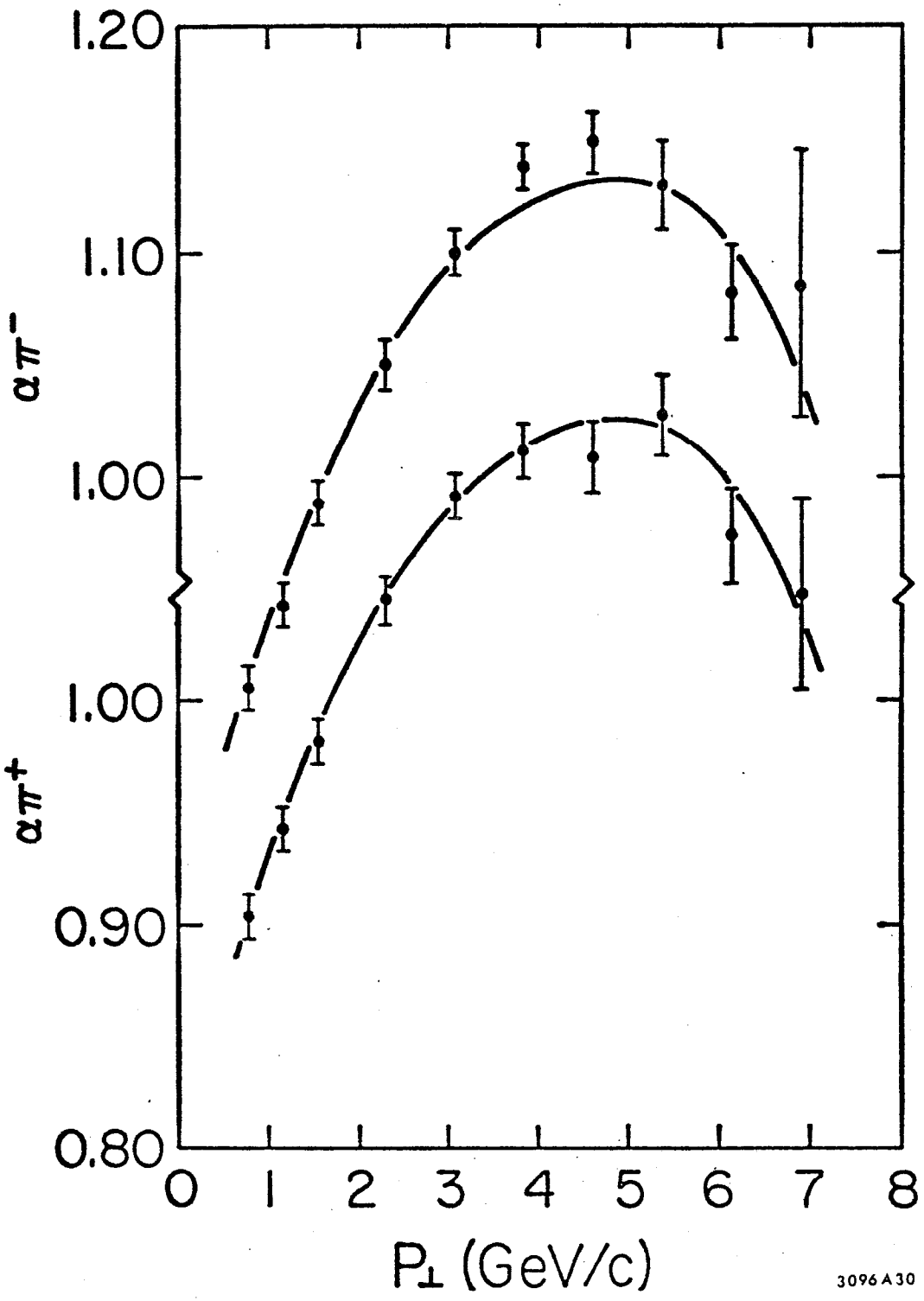
1.20
1.10
1.00
1.00
0.90
0.80
$\alpha\pi^-$
$\alpha\pi^+$
0
1
2
3
4
5
6
7
8
$P_\perp$ (GeV/c)
3096A30

Fig. 3

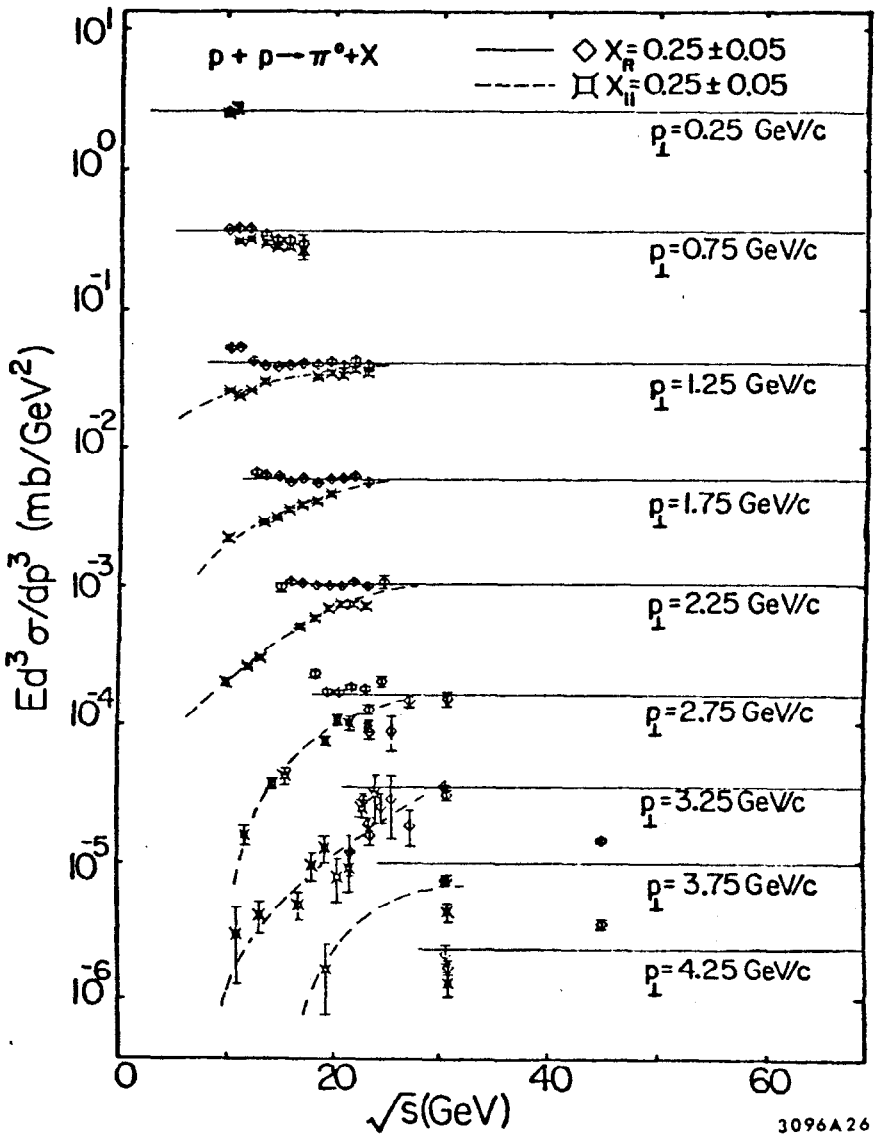
p + p → π° + X
◇ X_R = 0.25 ± 0.05
□ X_II = 0.25 ± 0.05
p_⊥ = 0.25 GeV/c
p_⊥ = 0.75 GeV/c
p_⊥ = 1.25 GeV/c
p_⊥ = 1.75 GeV/c
p_⊥ = 2.25 GeV/c
p_⊥ = 2.75 GeV/c
p_⊥ = 3.25 GeV/c
p_⊥ = 3.75 GeV/c
p_⊥ = 4.25 GeV/c
Ed³σ/dp³ (mb/GeV²)
√s(GeV)
0
20
40
60
3096A26

Fig. 4

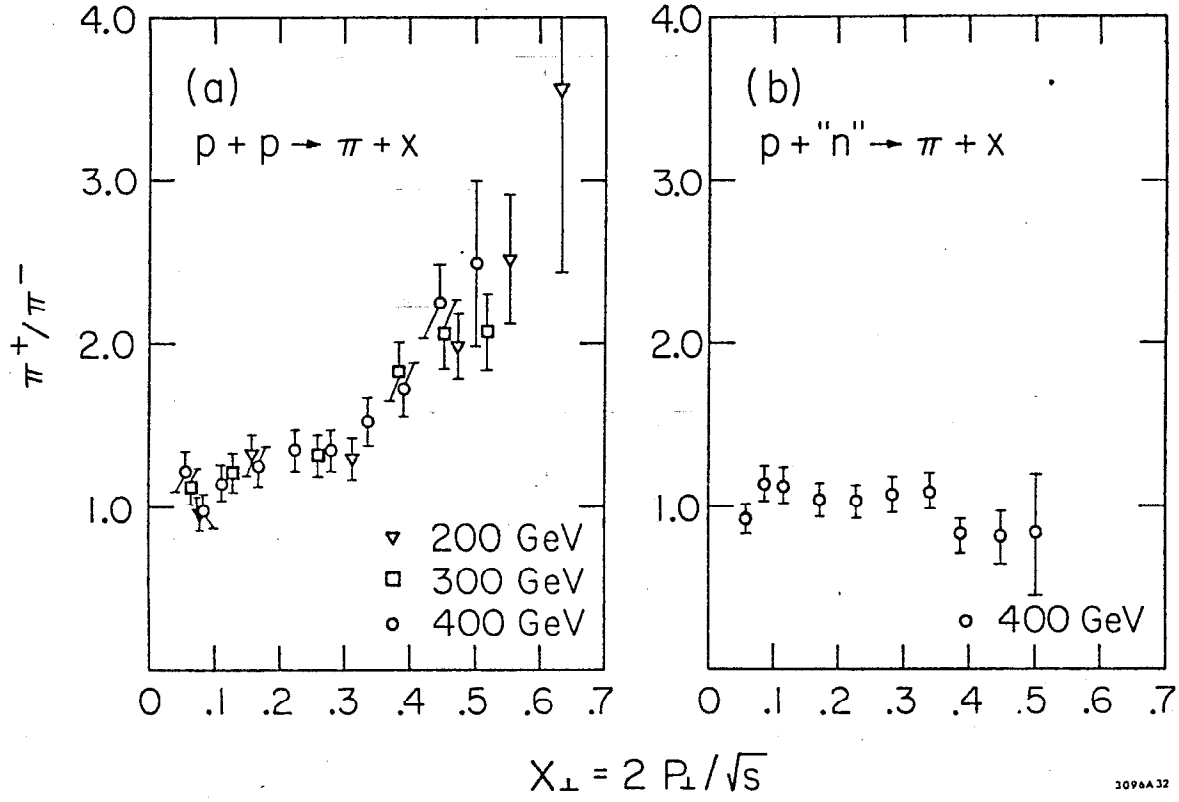
(a)
p + p → π + X
(b)
p + "n" → π + X
π⁺/π⁻
200 GeV
300 GeV
400 GeV
400 GeV
X⊥ = 2 P⊥ / √s
3096A32

Fig. 5

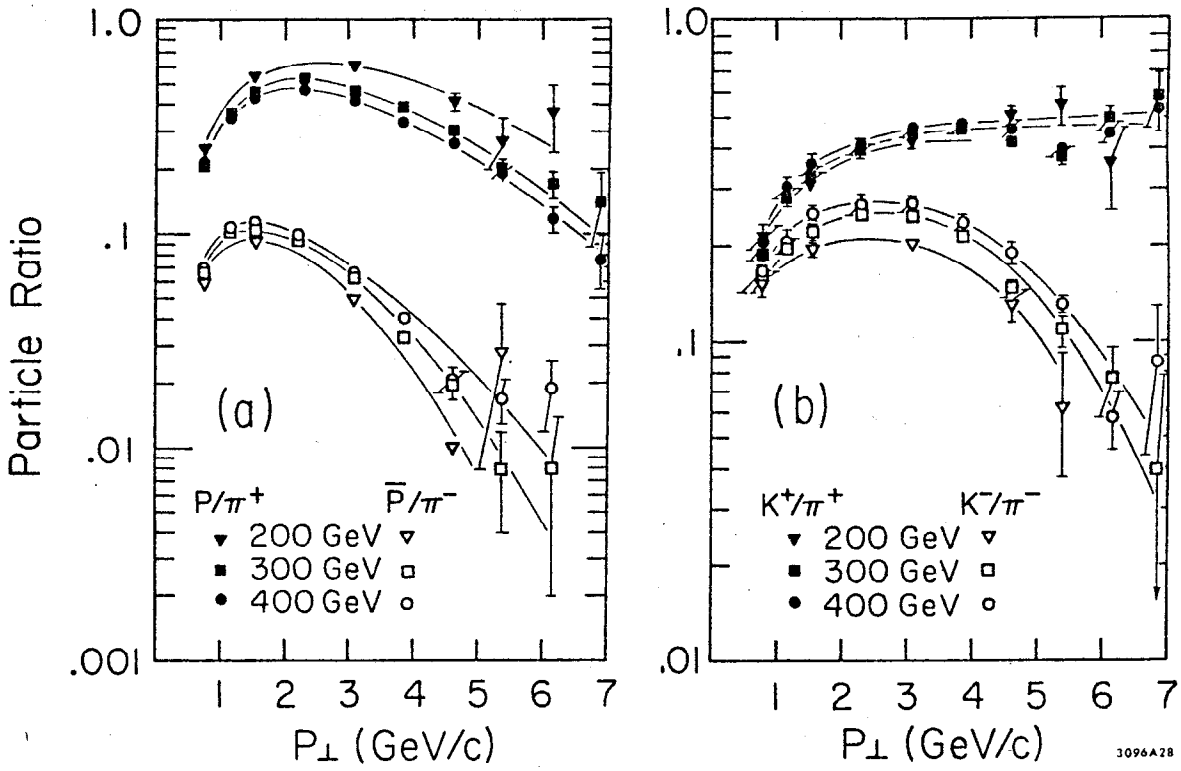
Particle Ratio
(a)
P/π⁺
P̄/π⁻
200 GeV
300 GeV
400 GeV
(b)
K⁺/π⁺
K⁻/π⁻
200 GeV
300 GeV
400 GeV
P⊥ (GeV/c)
P⊥ (GeV/c)
3096A28

Fig. 6

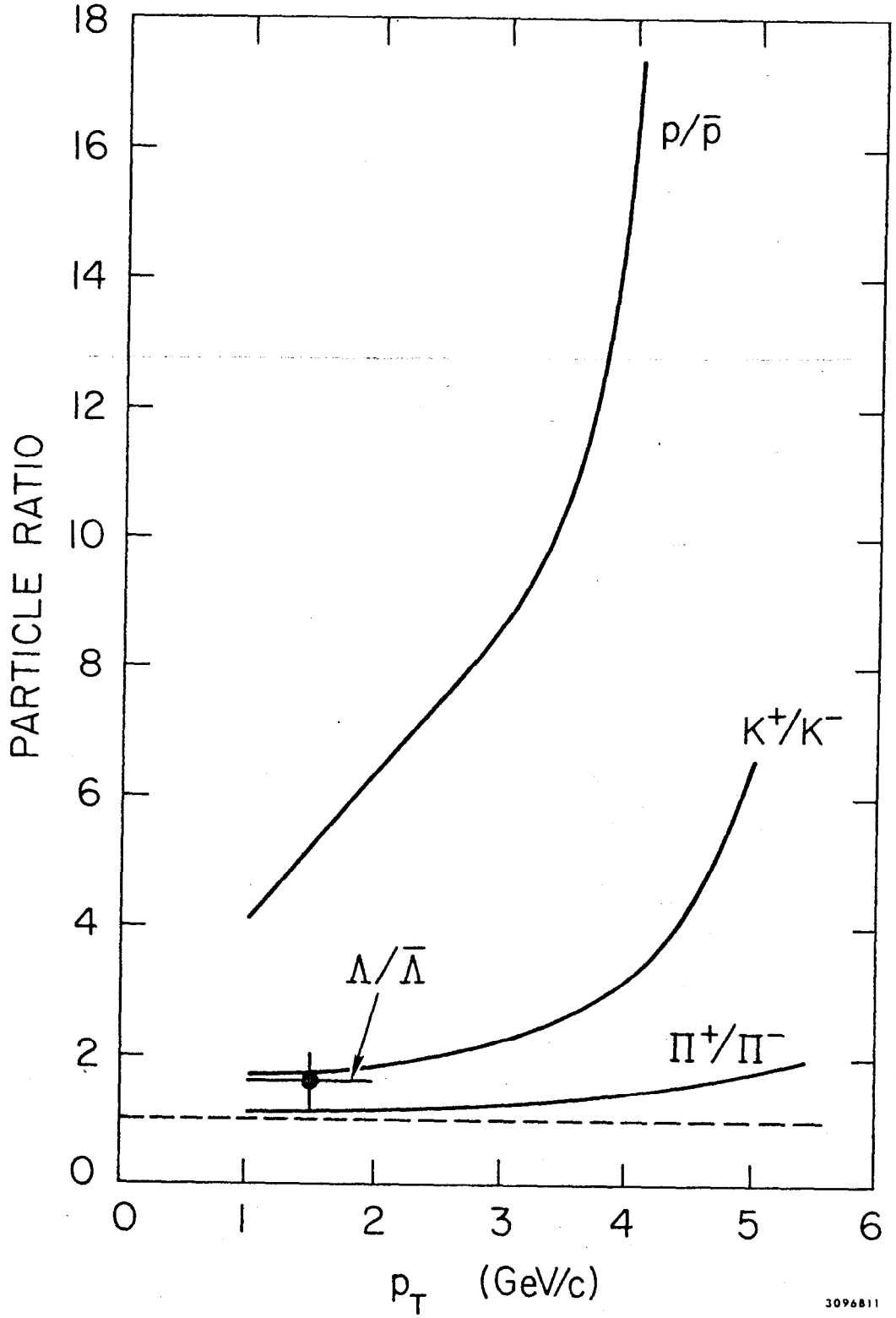
18
16
14
12
10
8
6
4
2
0
PARTICLE RATIO
p/p̄
K+/K−
Λ/Λ̄
Π+/Π−
0
1
2
3
4
5
6
pT (GeV/c)
3096811

Fig. 7

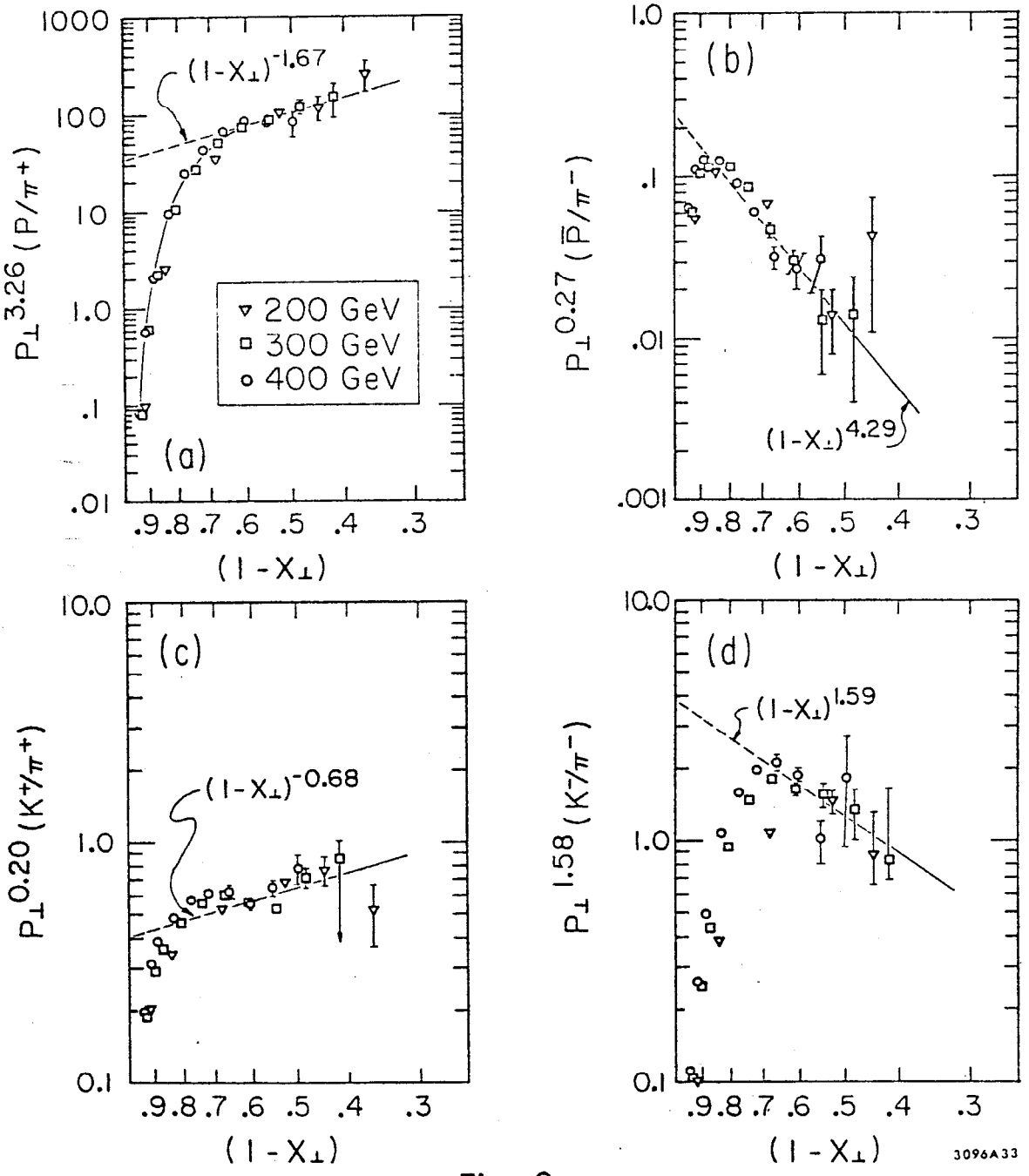
1000
100
10
1.0
.1
.01
$P_\perp^{3.26}(P/\pi^+)$
$(1-X_\perp)^{-1.67}$
200 GeV
300 GeV
400 GeV
(a)
.9 .8 .7 .6 .5 .4 .3
$(1-X_\perp)$
1.0
.1
.01
.001
$P_\perp^{0.27}(\bar{P}/\pi^-)$
(b)
$(1-X_\perp)^{4.29}$
.9 .8 .7 .6 .5 .4 .3
$(1-X_\perp)$
10.0
1.0
0.1
$P_\perp^{0.20}(K^+/\pi^+)$
(c)
$(1-X_\perp)^{-0.68}$
.9 .8 .7 .6 .5 .4 .3
$(1-X_\perp)$
10.0
1.0
0.1
$P_\perp^{1.58}(K^-/\pi^-)$
(d)
$(1-X_\perp)^{1.59}$
.9 .8 .7 .6 .5 .4 .3
$(1-X_\perp)$
3096A33

Fig. 8

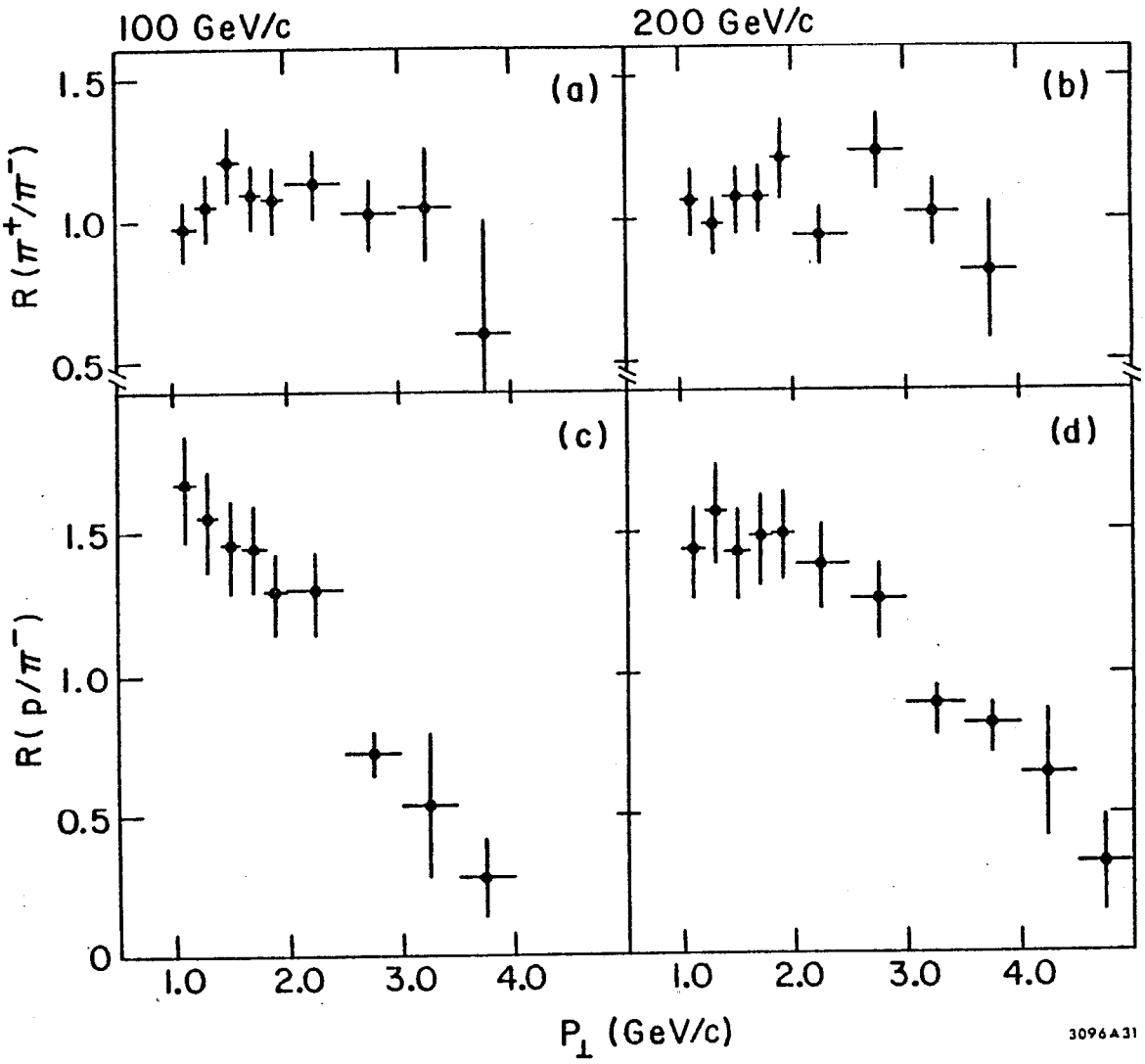
100 GeV/c
200 GeV/c
(a)
(b)
(c)
(d)
R (π+/π−)
R(p/π−)
1.5
1.0
0.5
0
1.0
2.0
3.0
4.0
P⊥ (GeV/c)
3096A31

Fig. 9

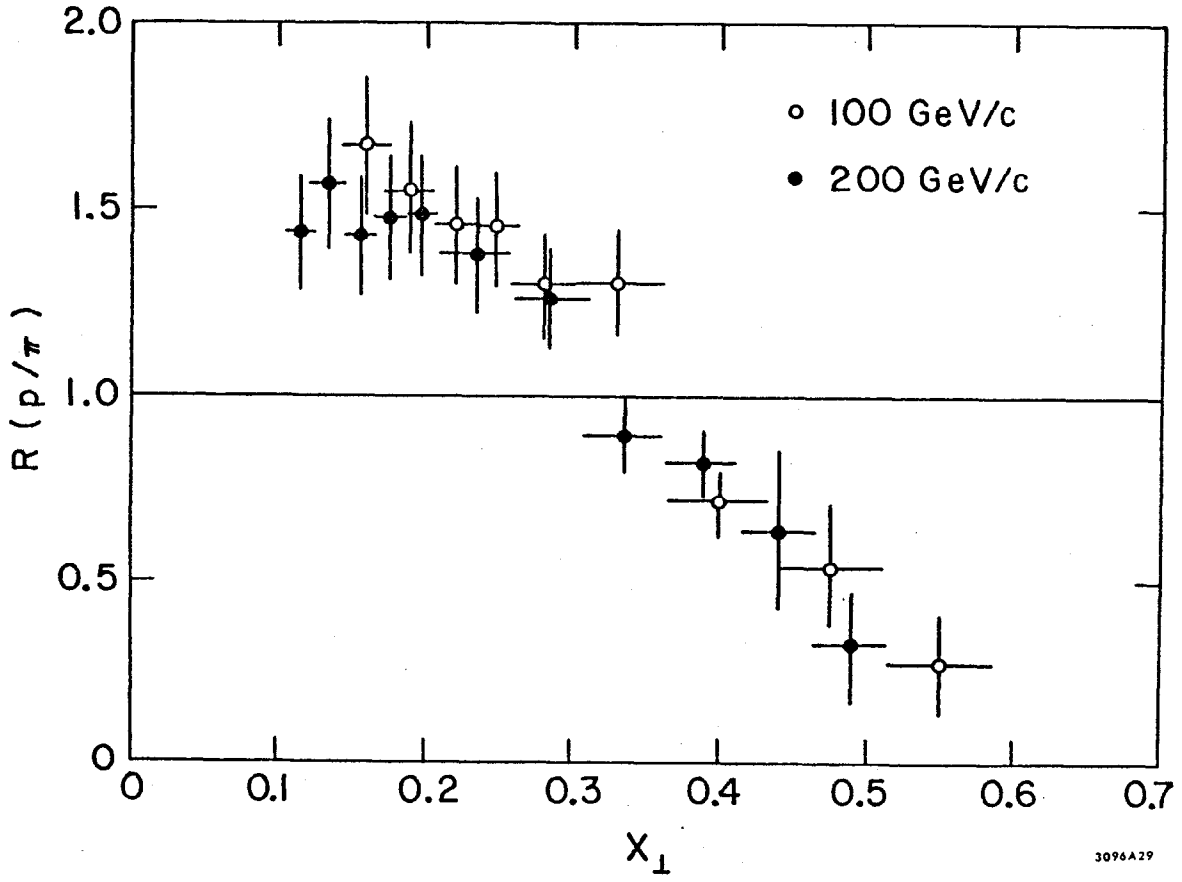
2.0
1.5
1.0
0.5
0
R (p/π)
100 GeV/c
200 GeV/c
0
0.1
0.2
0.3
0.4
0.5
0.6
0.7
X⊥
3096A29

Fig. 10

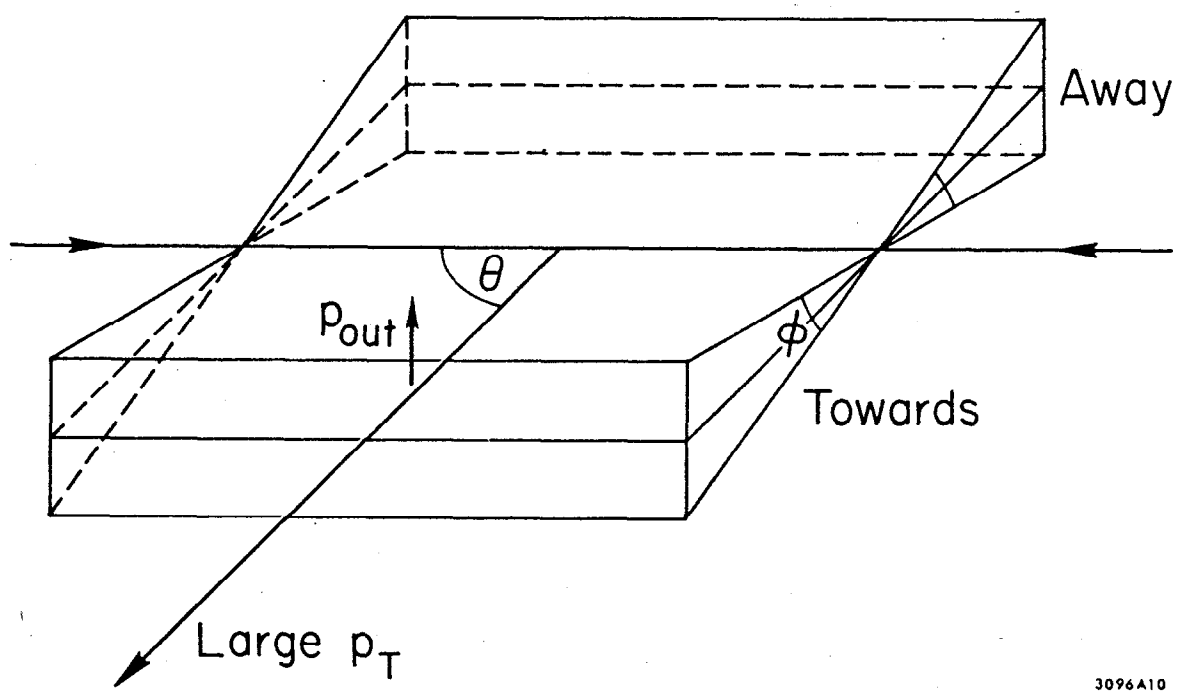
Away
θ
Pout
φ
Towards
Large pT
3096A10

Fig. 11

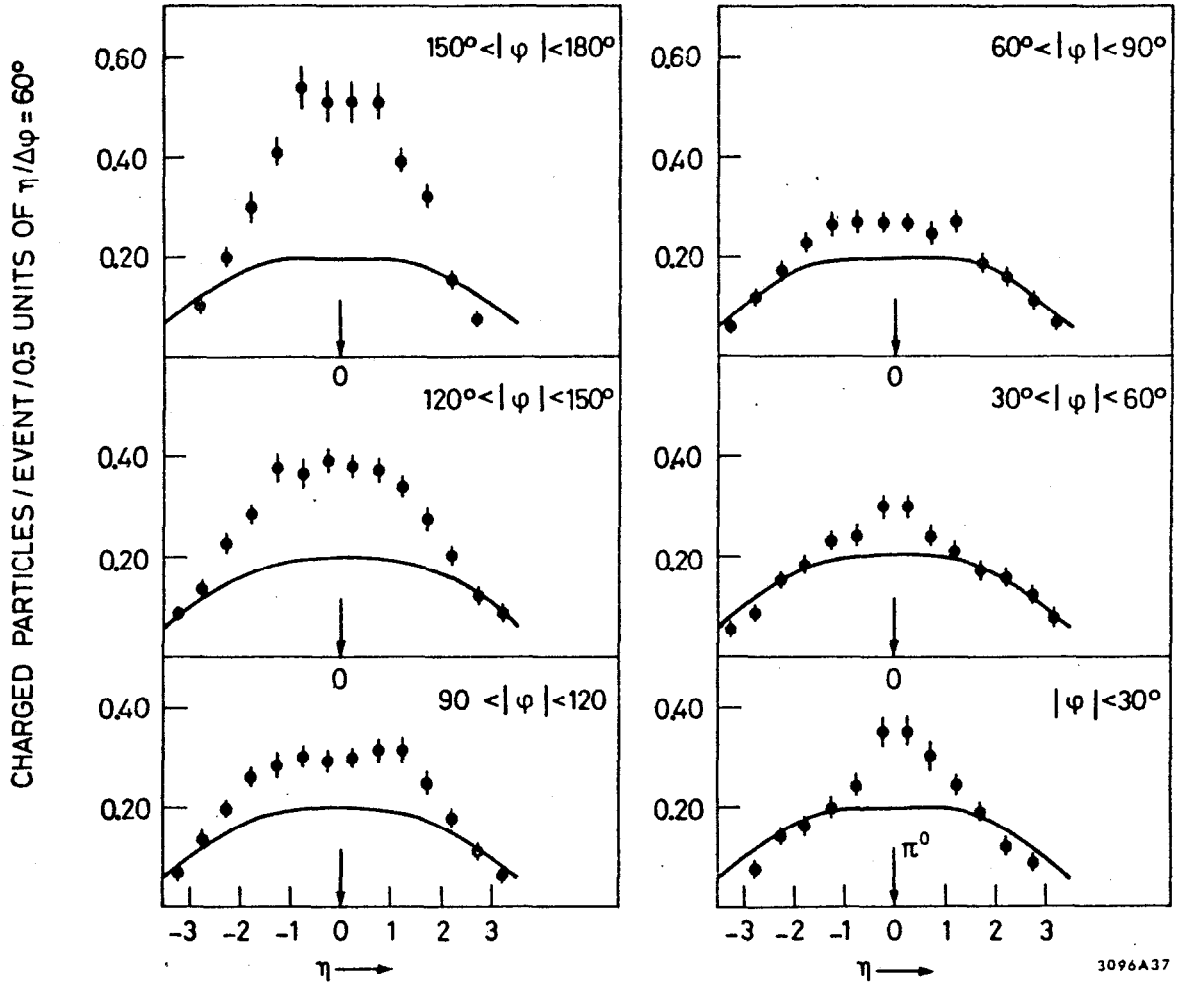
CHARGED PARTICLES / EVENT / 0.5 UNITS OF η/Δφ = 60°
150°<|φ|<180°
120°<|φ|<150°
90 <|φ|<120
60°<|φ|<90°
30°<|φ|<60°
|φ|<30°
0.60
0.40
0.20
0
π⁰
-3 -2 -1 0 1 2 3
η
3096A37

Fig. 12

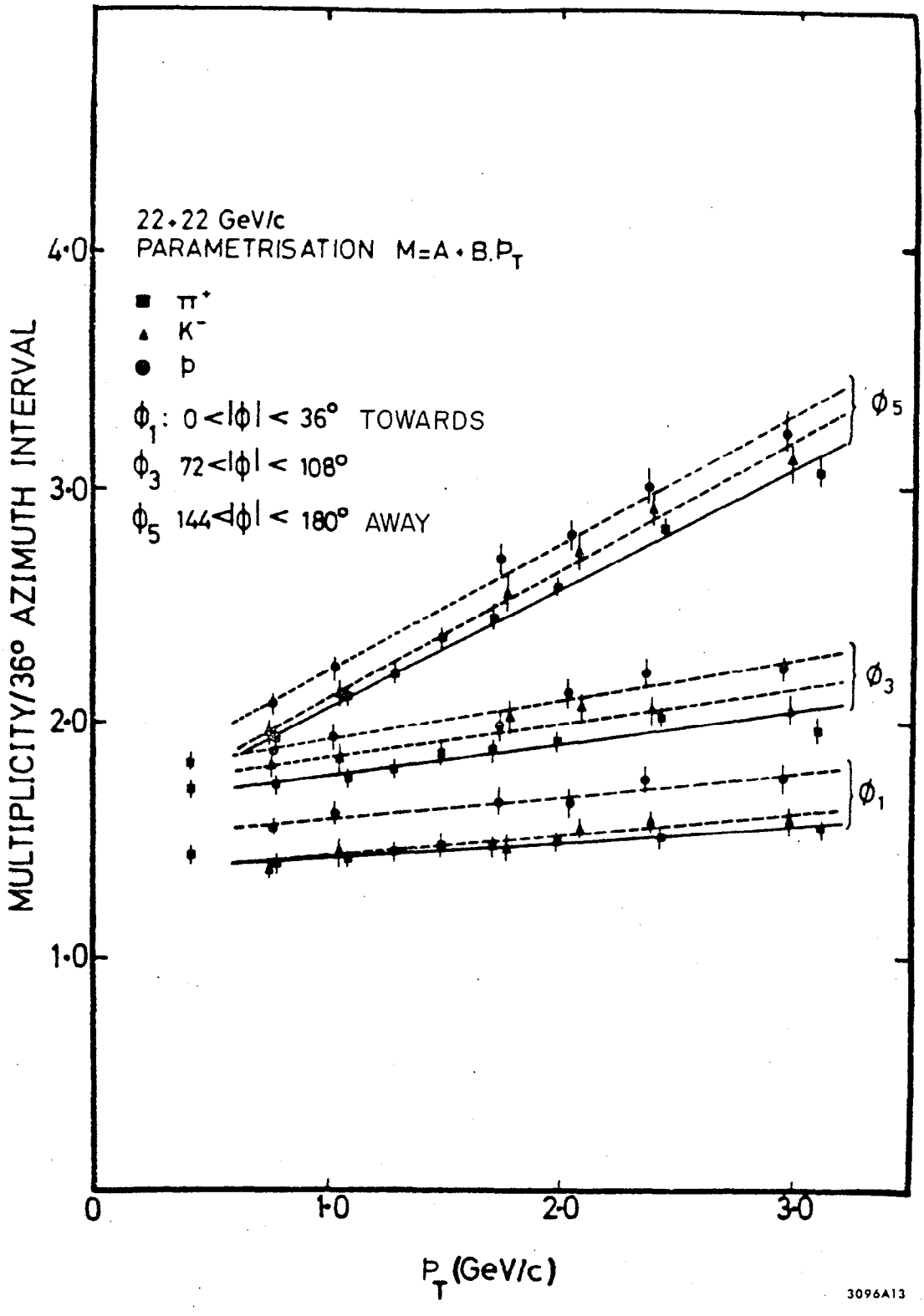
22·22 GeV/c
PARAMETRISATION M=A·B.P_T
π⁺
K⁻
p
φ1: 0<|φ|<36° TOWARDS
φ3 72<|φ|<108°
φ5 144<|φ|<180° AWAY
φ5
φ3
φ1
MULTIPLICITY/36° AZIMUTH INTERVAL
4·0
3·0
2·0
1·0
0
1·0
2·0
3·0
P_T (GeV/c)
3096A13

Fig. 13

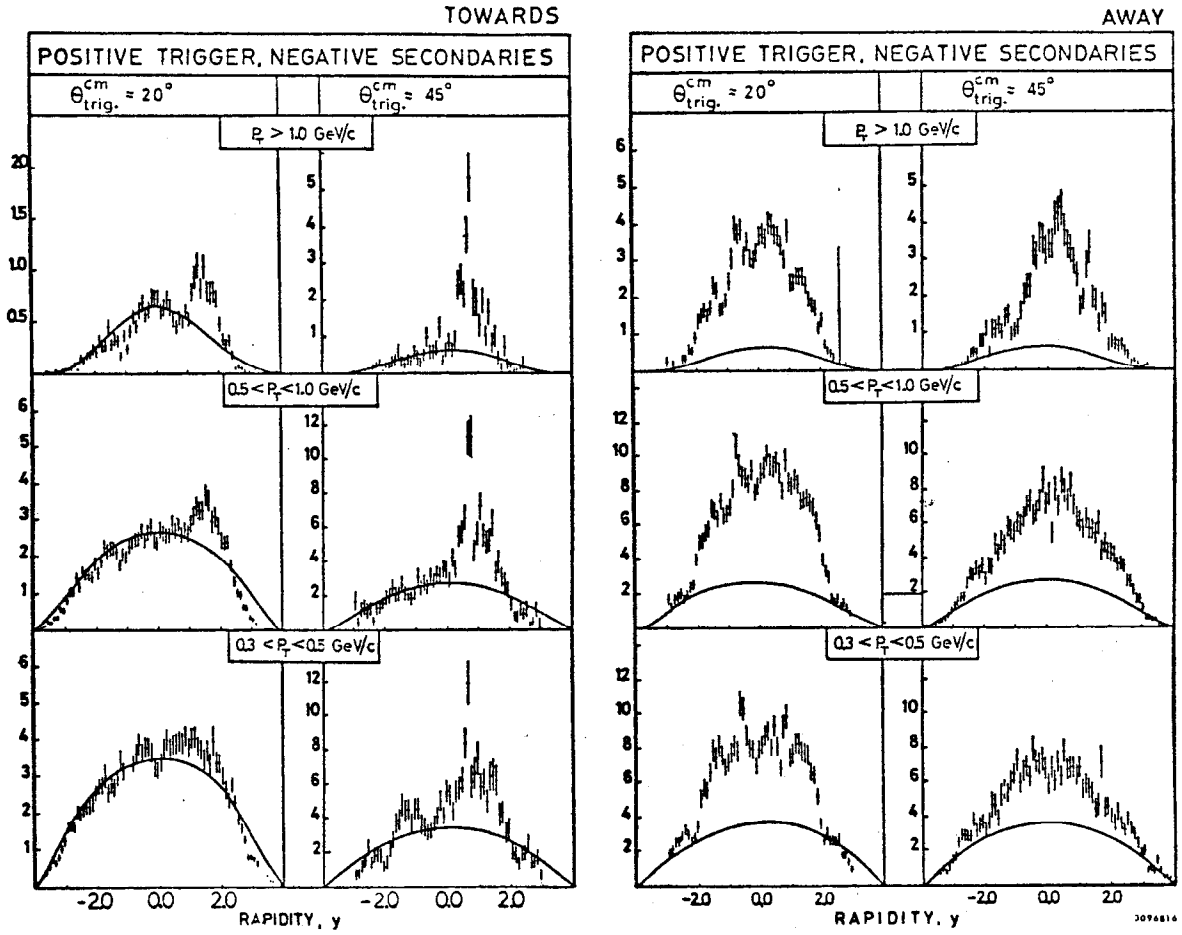
TOWARDS
AWAY
POSITIVE TRIGGER, NEGATIVE SECONDARIES
POSITIVE TRIGGER, NEGATIVE SECONDARIES
$\theta^{cm}_{trig.} \approx 20°$
$\theta^{cm}_{trig.} \approx 45°$
$P_T > 1.0$ GeV/c
$0.5 < P_T < 1.0$ GeV/c
$0.3 < P_T < 0.5$ GeV/c
RAPIDITY, y
RAPIDITY, y

Fig. 14

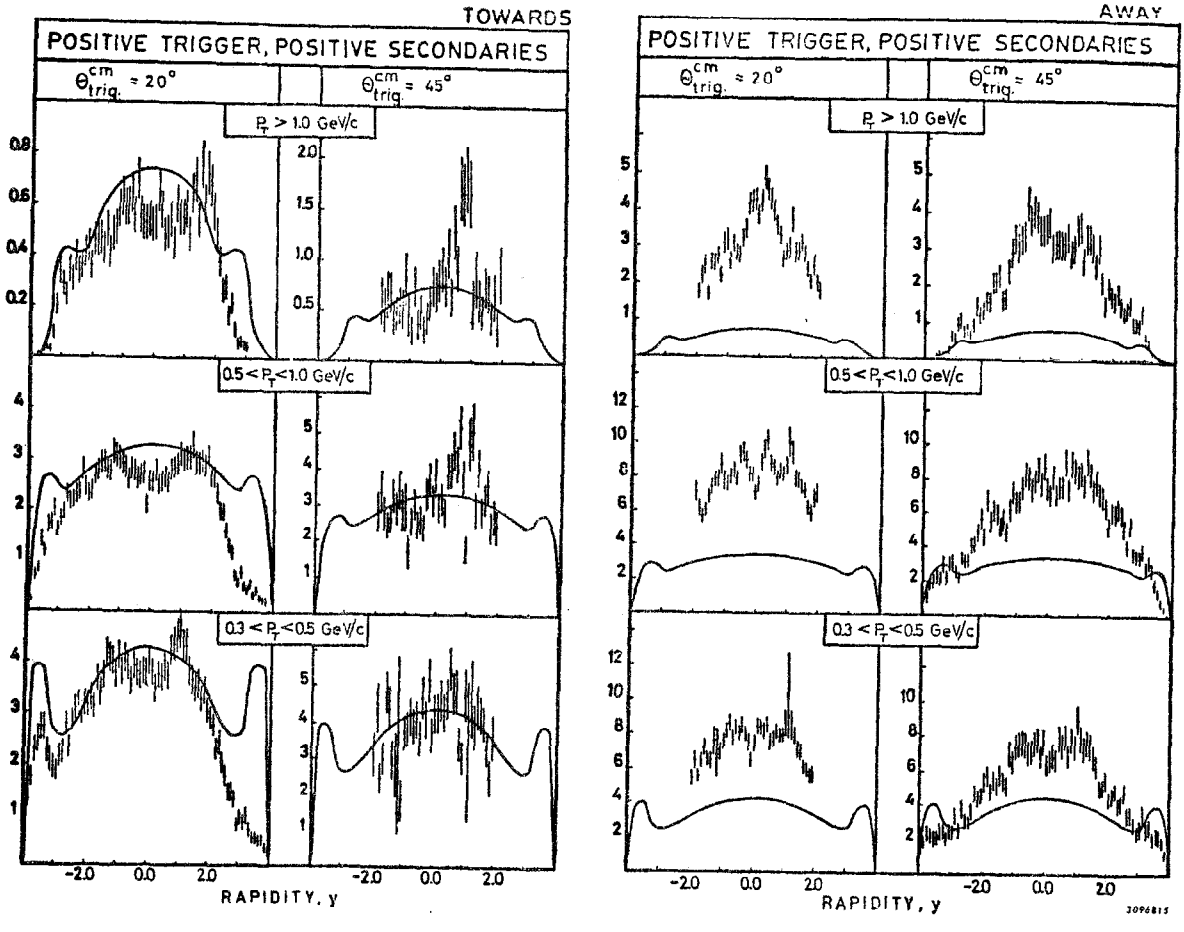
TOWARDS
POSITIVE TRIGGER, POSITIVE SECONDARIES
$\theta^{cm}_{trig.} \approx 20°$
$\theta^{cm}_{trig.} \approx 45°$
$P_T > 1.0$ GeV/c
$0.5 < P_T < 1.0$ GeV/c
$0.3 < P_T < 0.5$ GeV/c
RAPIDITY, y
AWAY
POSITIVE TRIGGER, POSITIVE SECONDARIES
$\theta^{cm}_{trig.} \approx 20°$
$\theta^{cm}_{trig.} \approx 45°$
$P_T > 1.0$ GeV/c
$0.5 < P_T < 1.0$ GeV/c
$0.3 < P_T < 0.5$ GeV/c
RAPIDITY, y

Fig. 15

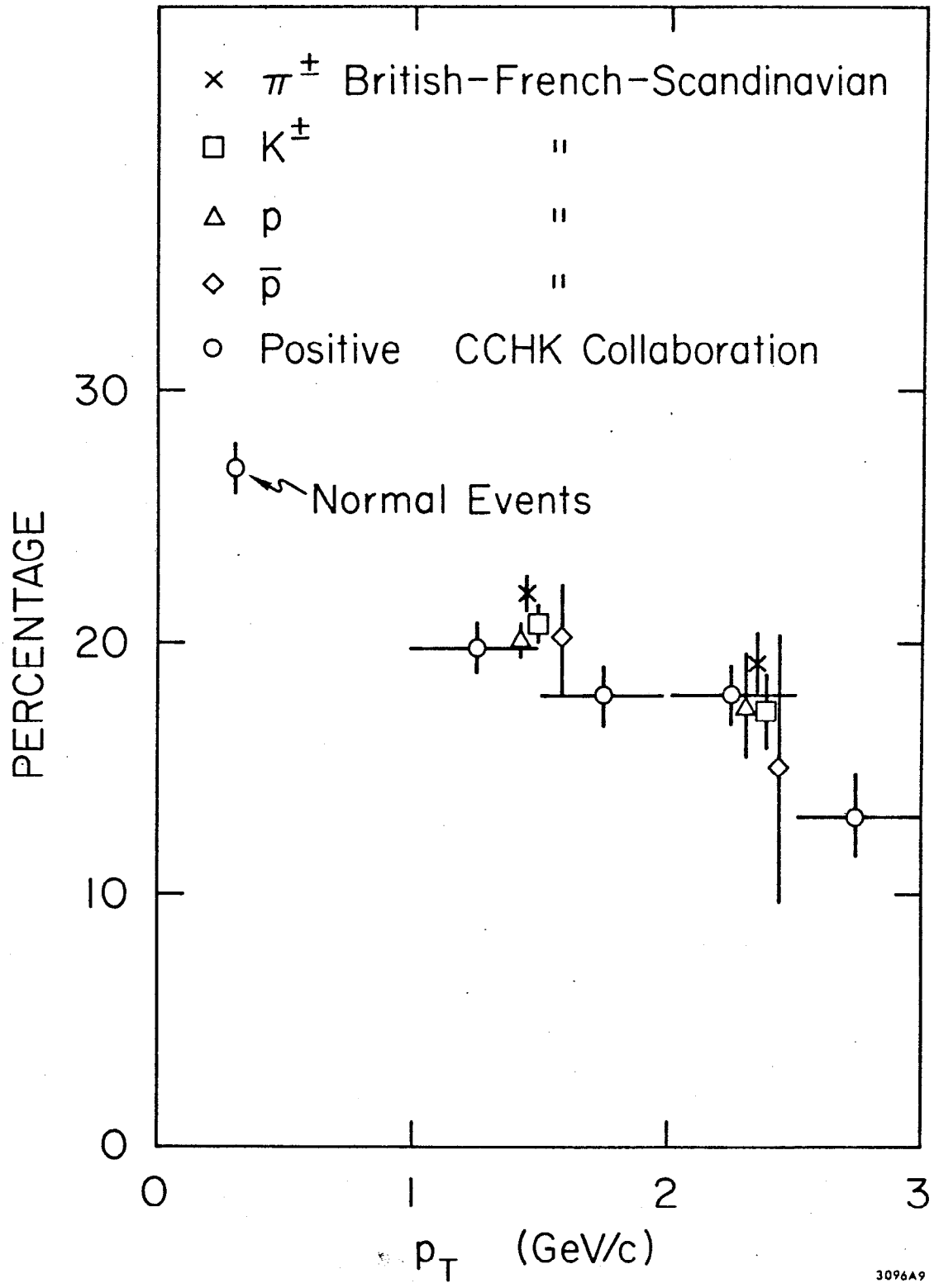
× $\pi^{\pm}$ British-French-Scandinavian
□ $K^{\pm}$ "
△ p "
◇ $\bar{p}$ "
○ Positive CCHK Collaboration
Normal Events
PERCENTAGE
30
20
10
0
0
1
2
3
p_T (GeV/c)
3096A9

Fig. 16

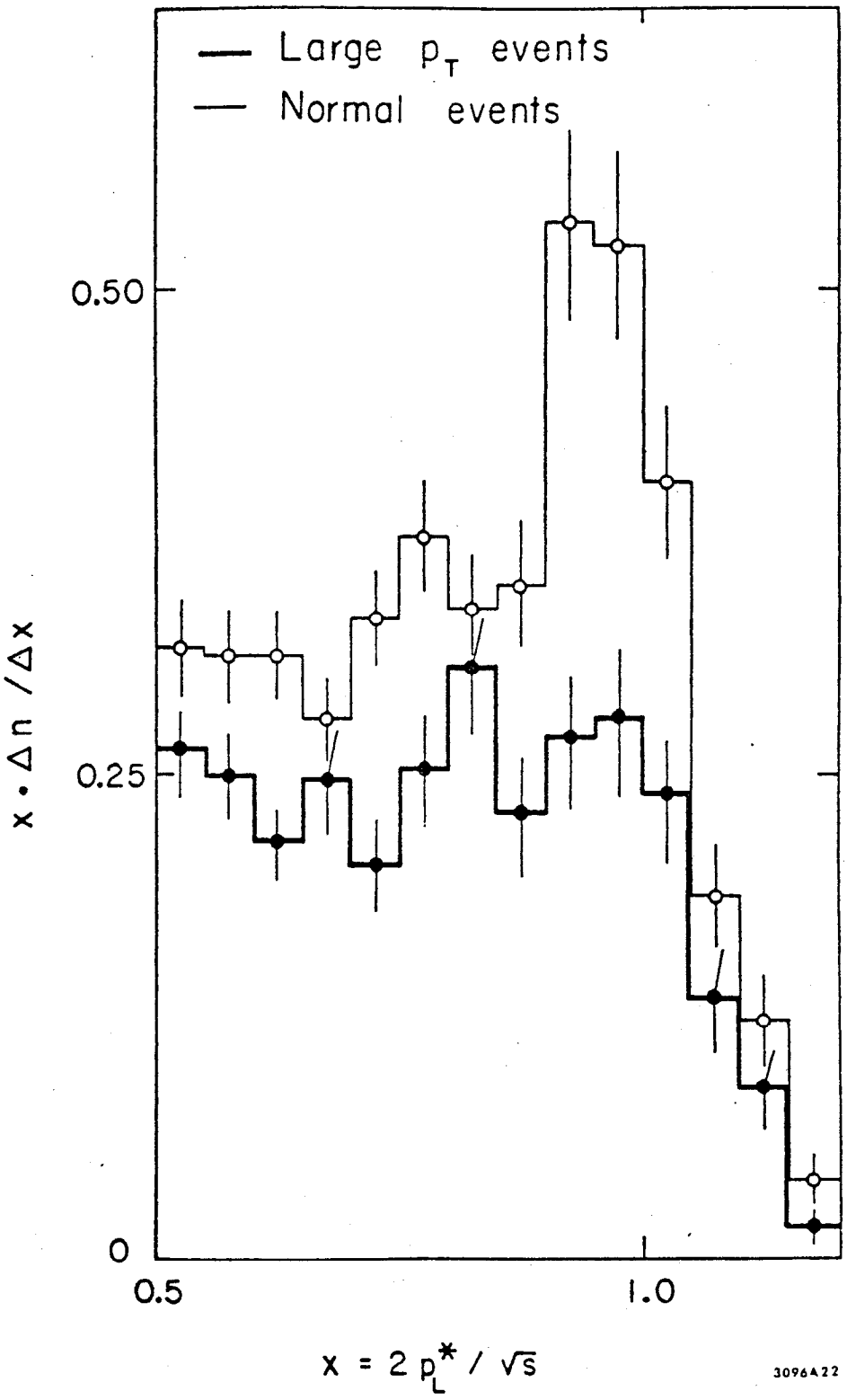
Large p_T events
Normal events
0.50
0.25
0
0.5
1.0
$x \cdot \Delta n / \Delta x$
$x = 2 p_L^* / \sqrt{s}$
3096A22

Fig. 17

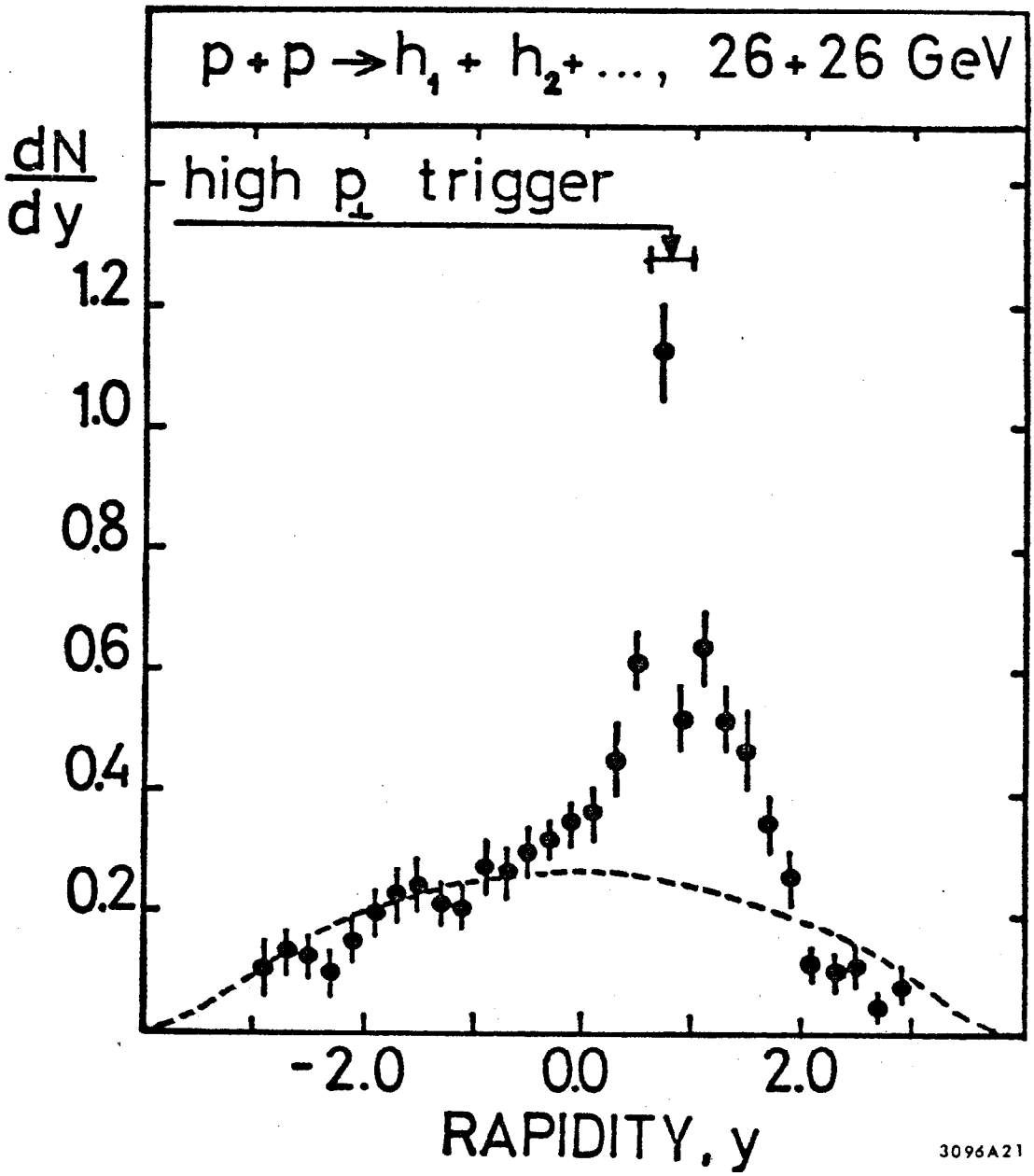
p + p → h1 + h2 + ..., 26 + 26 GeV
high p⊥ trigger
dN/dy
1.2
1.0
0.8
0.6
0.4
0.2
-2.0
0.0
2.0
RAPIDITY, y
3096A21

Fig. 18

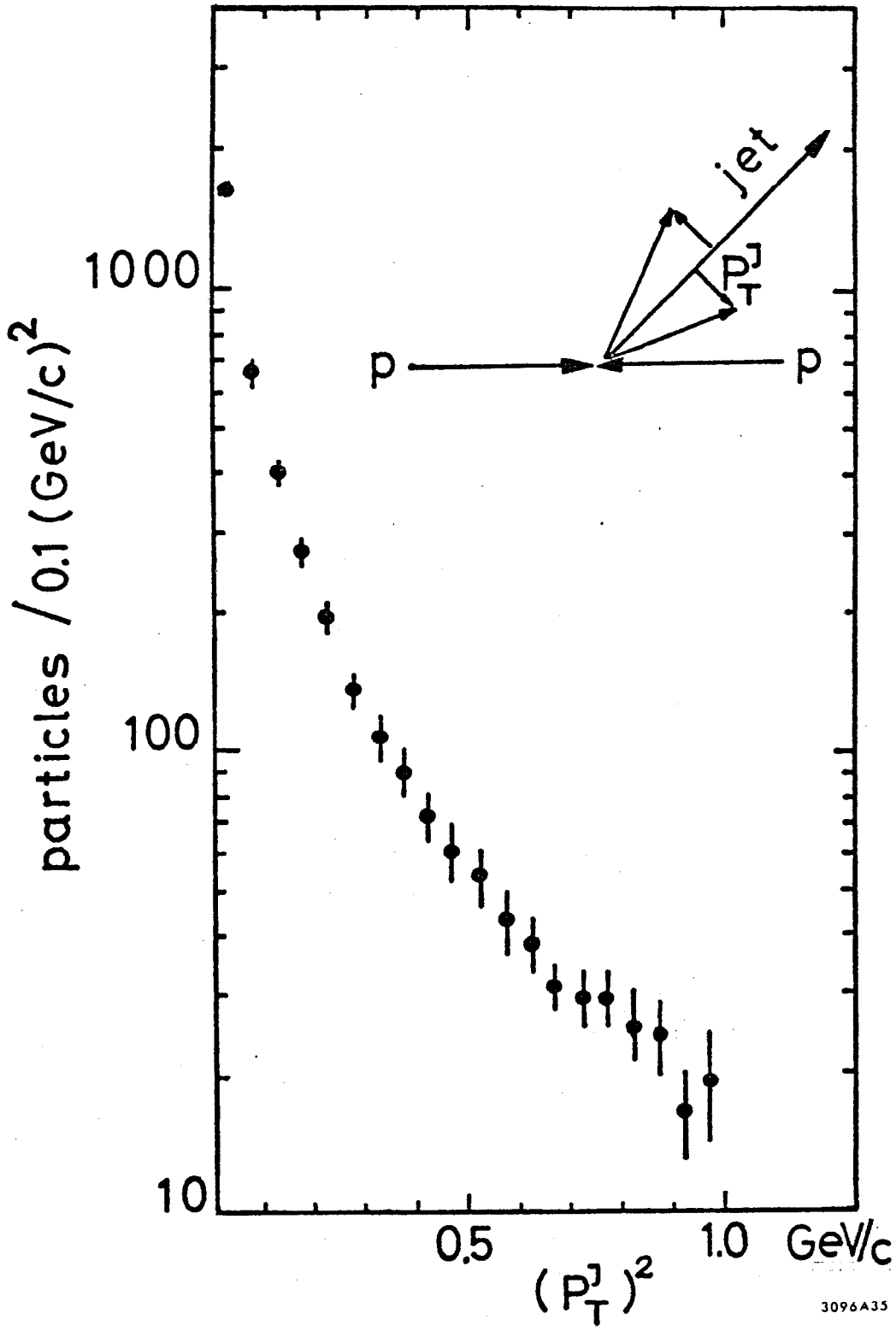
1000
100
10
particles /0.1 (GeV/c)^2
jet
P_T^J
p
p
0.5
1.0
GeV/c
$(P_T^J)^2$
3096A35

Fig. 19

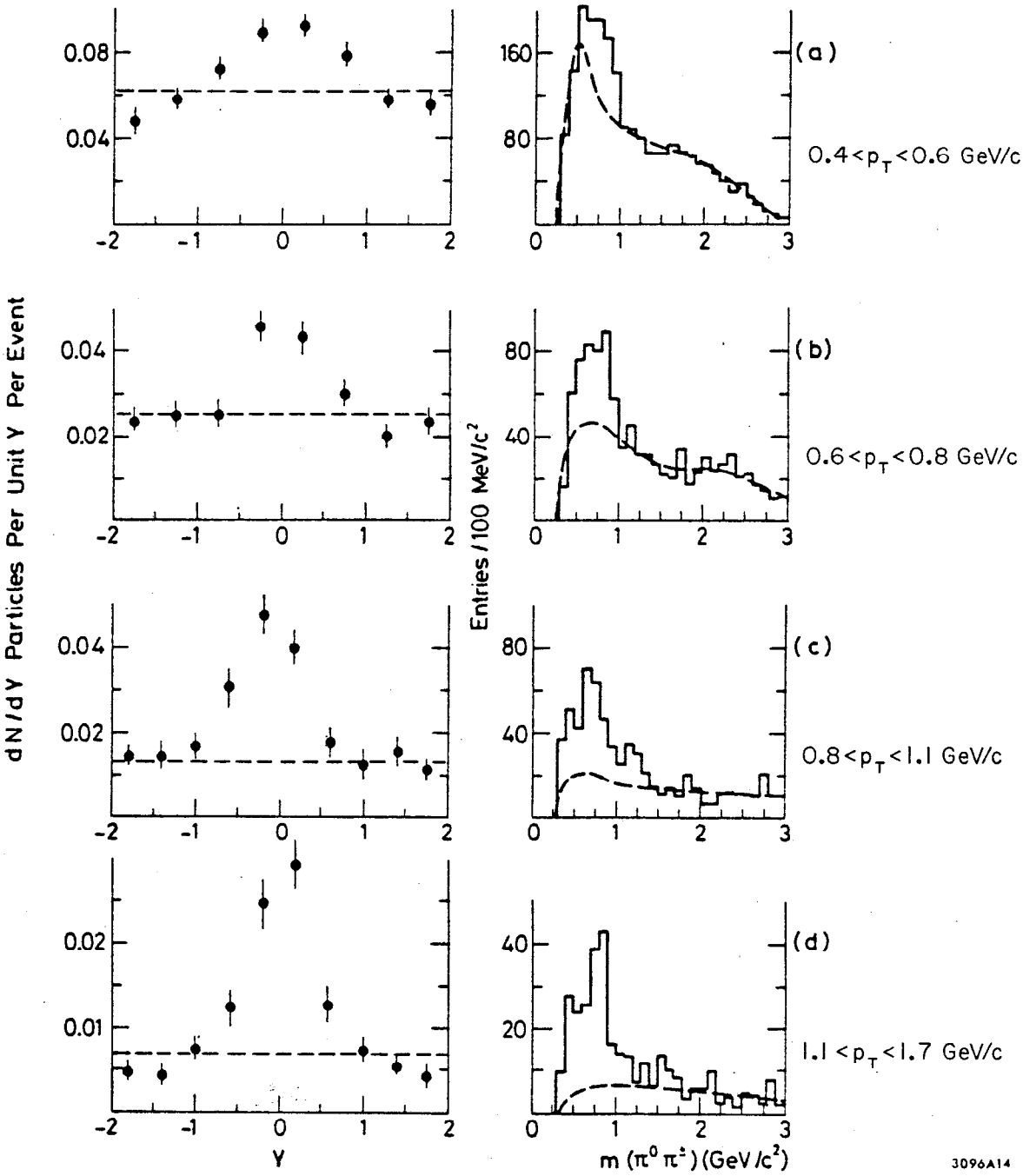
dN/dY Particles Per Unit Y Per Event
Entries / 100 MeV/c²
Y
m (π⁰ π±) (GeV/c²)
(a)
0.4<p_T<0.6 GeV/c
(b)
0.6<p_T<0.8 GeV/c
(c)
0.8<p_T<1.1 GeV/c
(d)
1.1<p_T<1.7 GeV/c
3096A14

Fig. 20

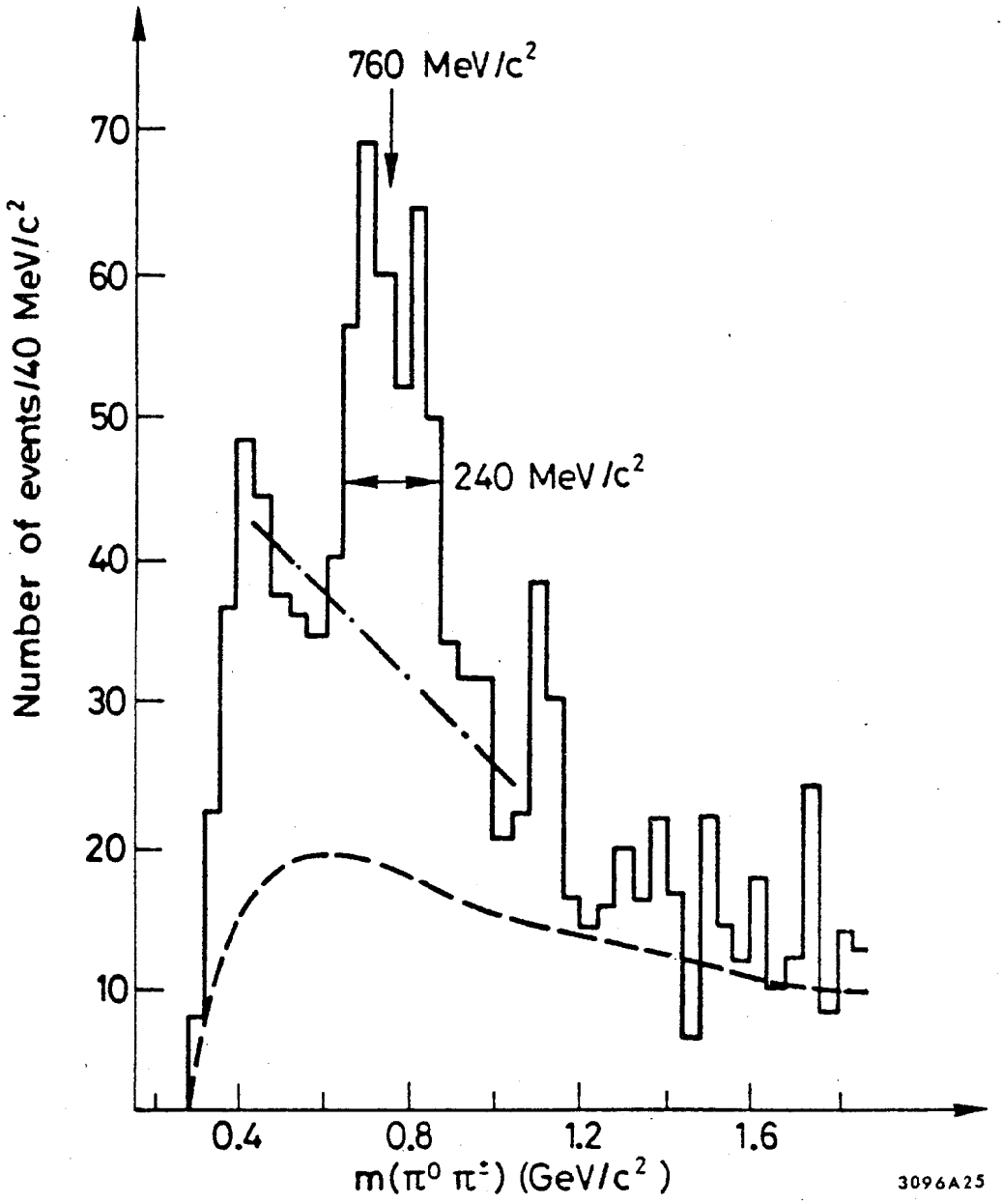
760 MeV/c²
240 MeV/c²
Number of events/40 MeV/c²
70
60
50
40
30
20
10
0.4
0.8
1.2
1.6
m(π⁰ π⁻) (GeV/c²)
3096A25

Fig. 21

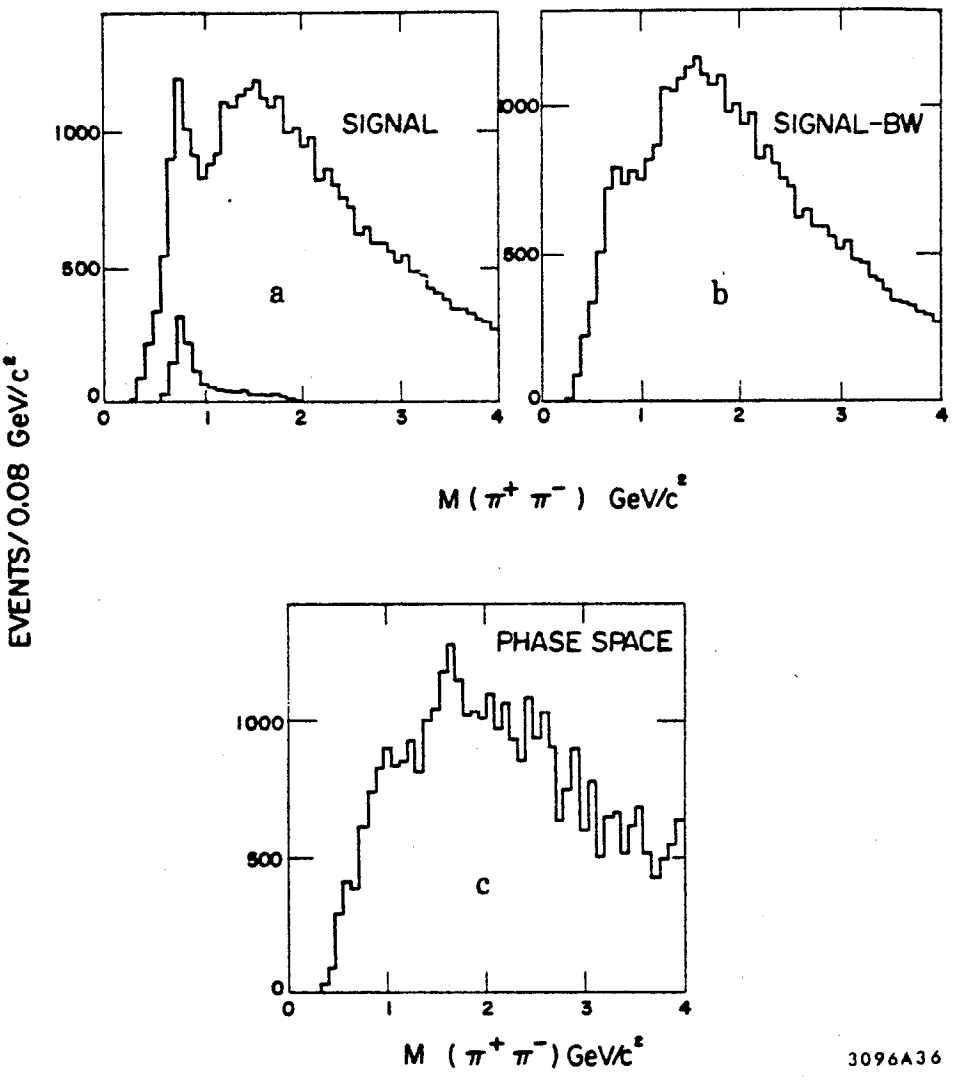
SIGNAL
a
SIGNAL-BW
b
PHASE SPACE
c
1000
500
0
1
2
3
4
EVENTS/0.08 GeV/c²
M (π⁺ π⁻) GeV/c²
M (π⁺ π⁻) GeV/c²
3096A36

Fig. 22

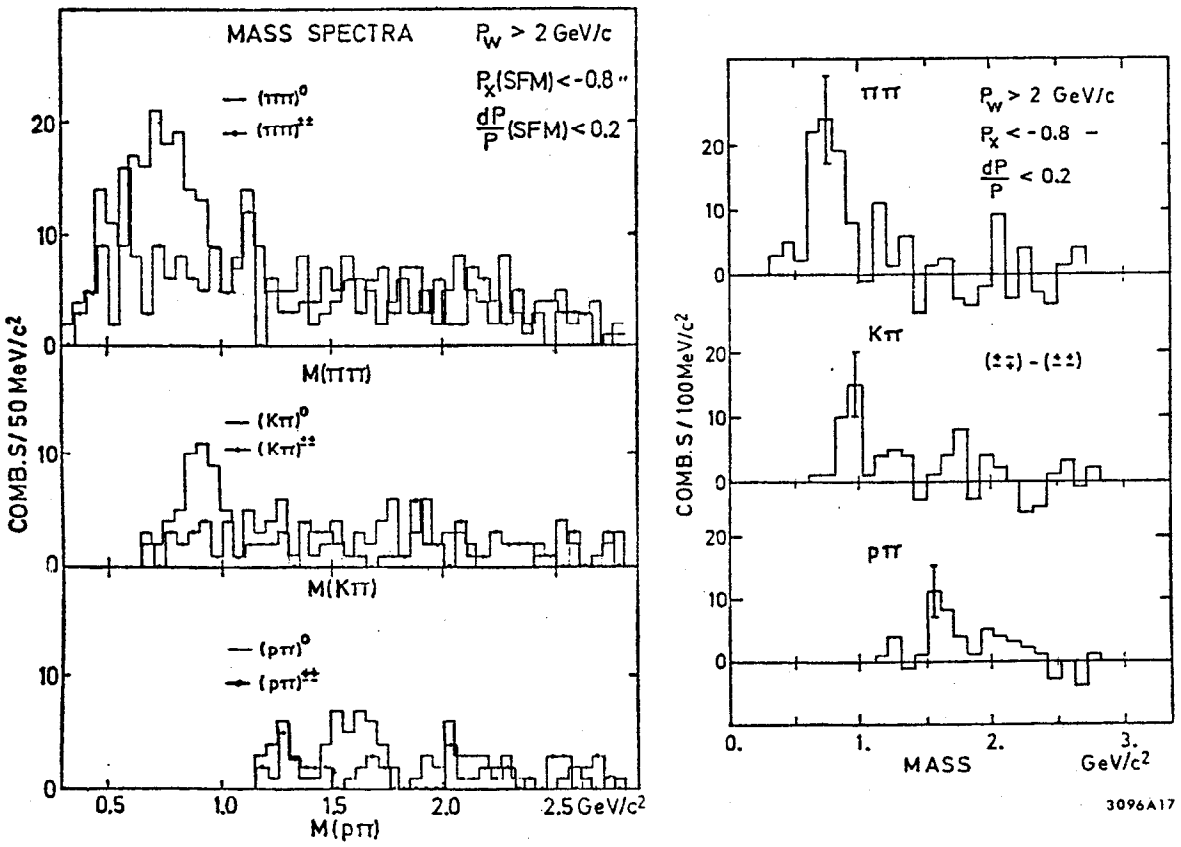
MASS SPECTRA
P_W > 2 GeV/c
P_x(SFM) < -0.8
$\frac{dP}{P}$(SFM) < 0.2
$(\pi\pi\pi)^0$
$(\pi\pi\pi)^{\pm}$
M(πππ)
$(K\pi\pi)^0$
$(K\pi\pi)^{\pm}$
M(Kππ)
$(p\pi\pi)^0$
$(p\pi\pi)^{\pm}$
M(pππ)
COMB.S/50 MeV/c²
0.5
1.0
1.5
2.0
2.5 GeV/c²
ππ π
P_W > 2 GeV/c
P_x < -0.8
$\frac{dP}{P}$ < 0.2
Kππ
(±∓) - (±±)
pππ
COMB.S/100MeV/c²
0.
1.
2.
3.
MASS
GeV/c²
3096A17

Fig. 23

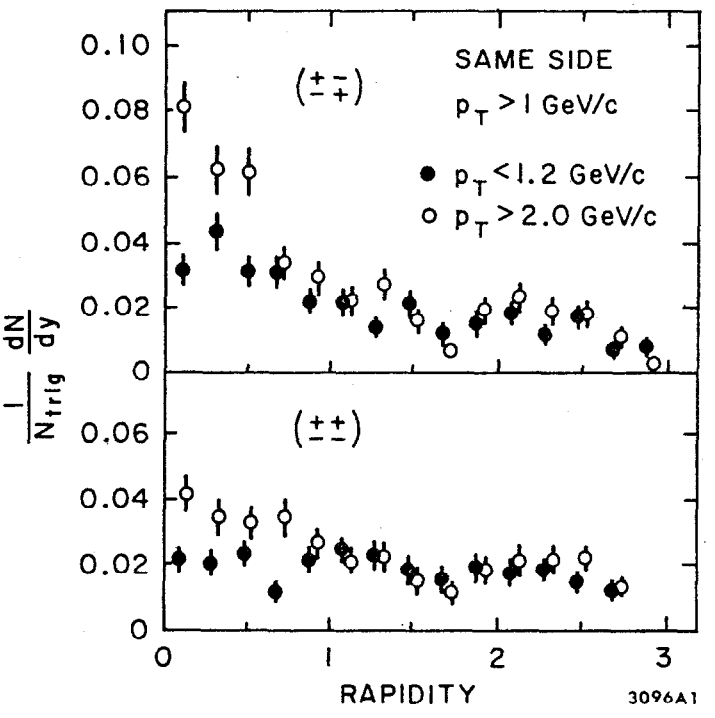
0.10
0.08
0.06
0.04
0.02
0
(+ −)
(− +)
SAME SIDE
$p_T > 1$ GeV/c
$p_T < 1.2$ GeV/c
$p_T > 2.0$ GeV/c
$\frac{1}{N_{trig}} \frac{dN}{dy}$
0.06
0.04
0.02
0
(+ +)
(− −)
0
1
2
3
RAPIDITY
3096A1

Fig. 24

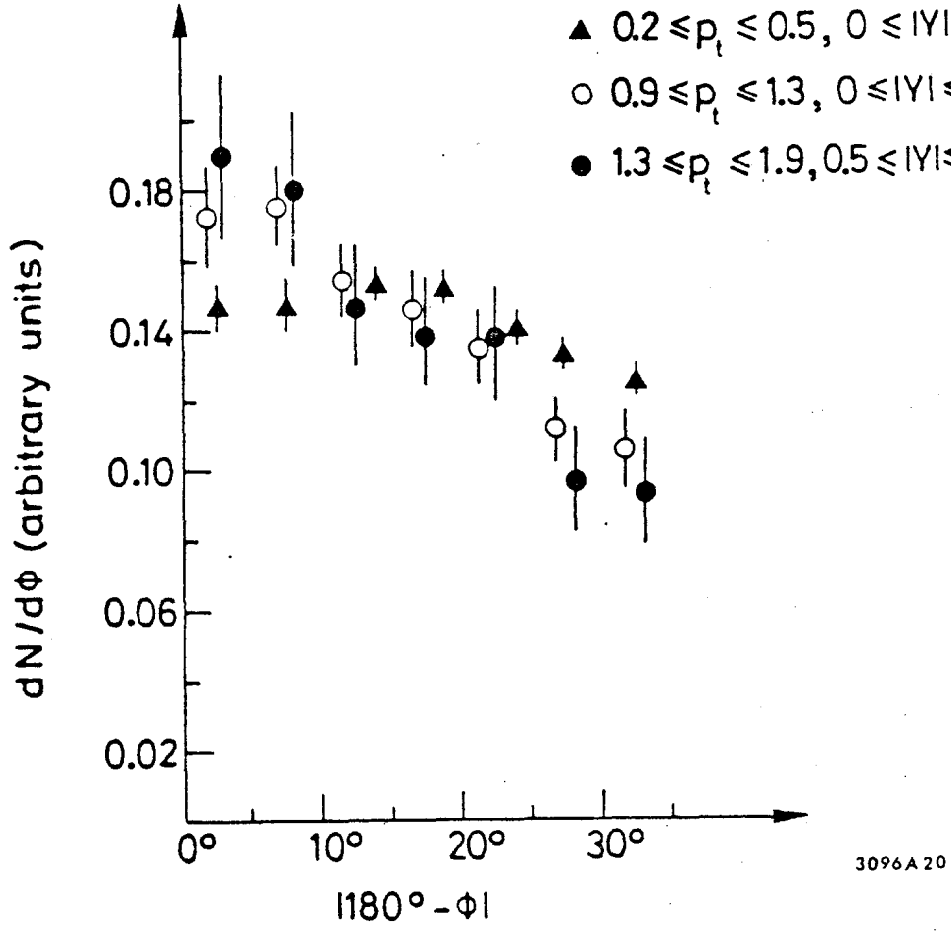
▲ 0.2 ≤ p_t ≤ 0.5, 0 ≤ |Y| ≤ 2.5
○ 0.9 ≤ p_t ≤ 1.3, 0 ≤ |Y| ≤ 2.5
● 1.3 ≤ p_t ≤ 1.9, 0.5 ≤ |Y| ≤ 2.5
dN/dΦ (arbitrary units)
0.18
0.14
0.10
0.06
0.02
0°
10°
20°
30°
|180° - Φ|
3096A20

Fig. 25

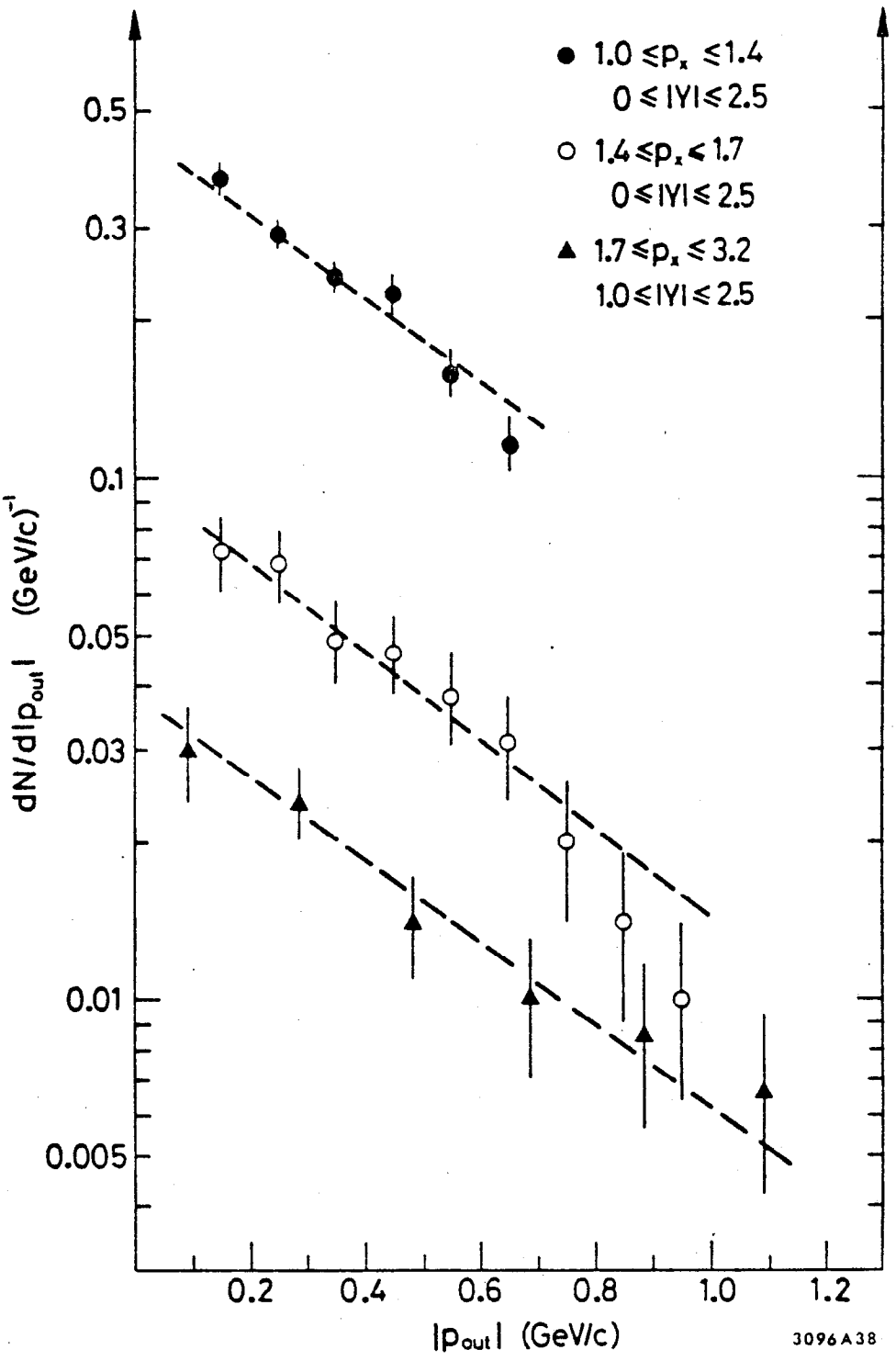
● 1.0 ≤ p_x ≤ 1.4
0 ≤ |y| ≤ 2.5
○ 1.4 ≤ p_x ≤ 1.7
0 ≤ |y| ≤ 2.5
▲ 1.7 ≤ p_x ≤ 3.2
1.0 ≤ |y| ≤ 2.5
0.5
0.3
0.1
0.05
0.03
0.01
0.005
$dN/d|p_{out}|$ $(GeV/c)^{-1}$
0.2
0.4
0.6
0.8
1.0
1.2
$|p_{out}|$ (GeV/c)
3096A38

Fig. 26

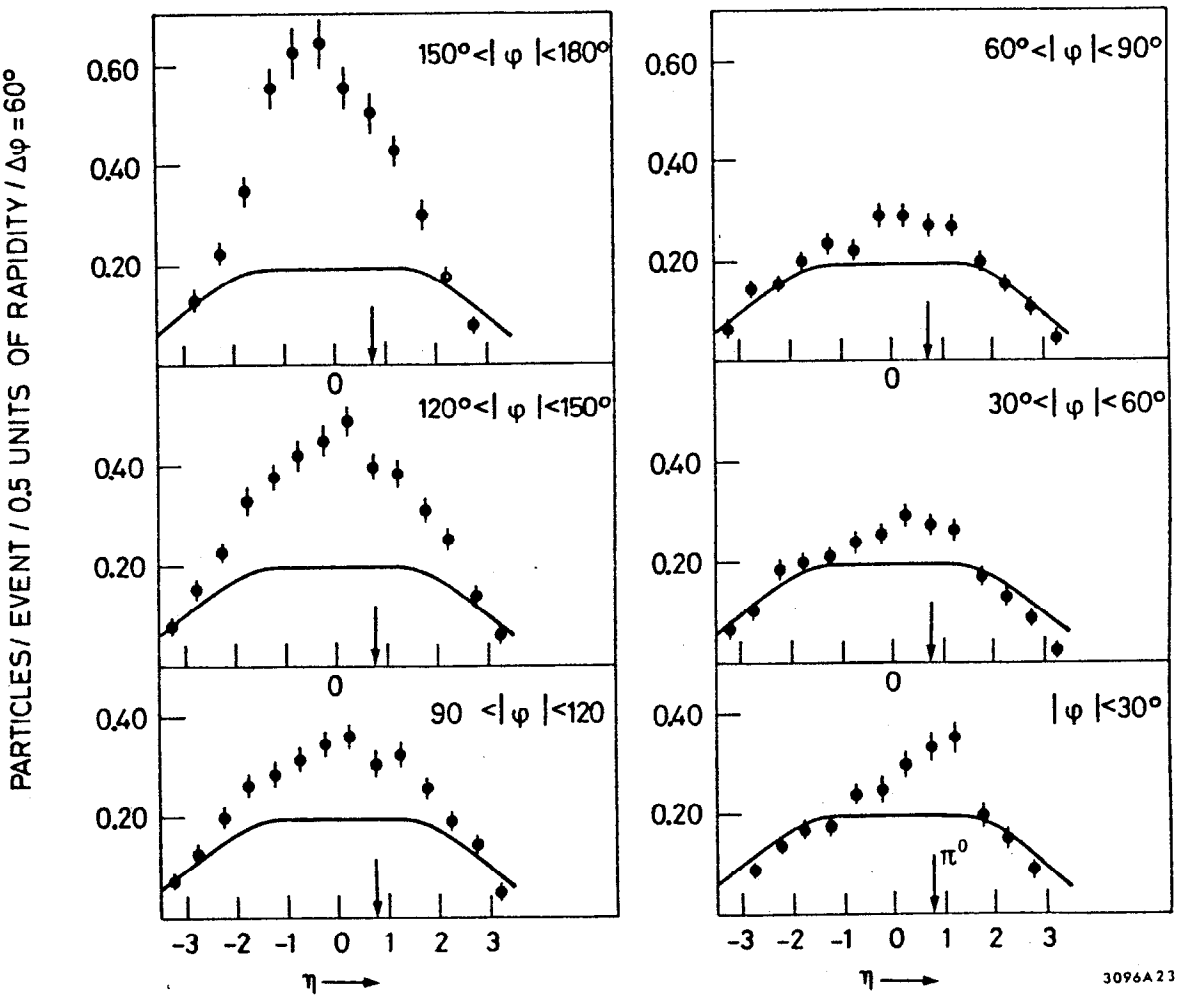
PARTICLES/ EVENT / 0.5 UNITS OF RAPIDITY / Δφ = 60°
150°<| φ |<180°
120°<| φ |<150°
90 <| φ |<120
60°<| φ |<90°
30°<| φ |<60°
| φ |<30°
0.60
0.40
0.20
0
-3 -2 -1 0 1 2 3
η
π⁰
3096A23

Fig. 27

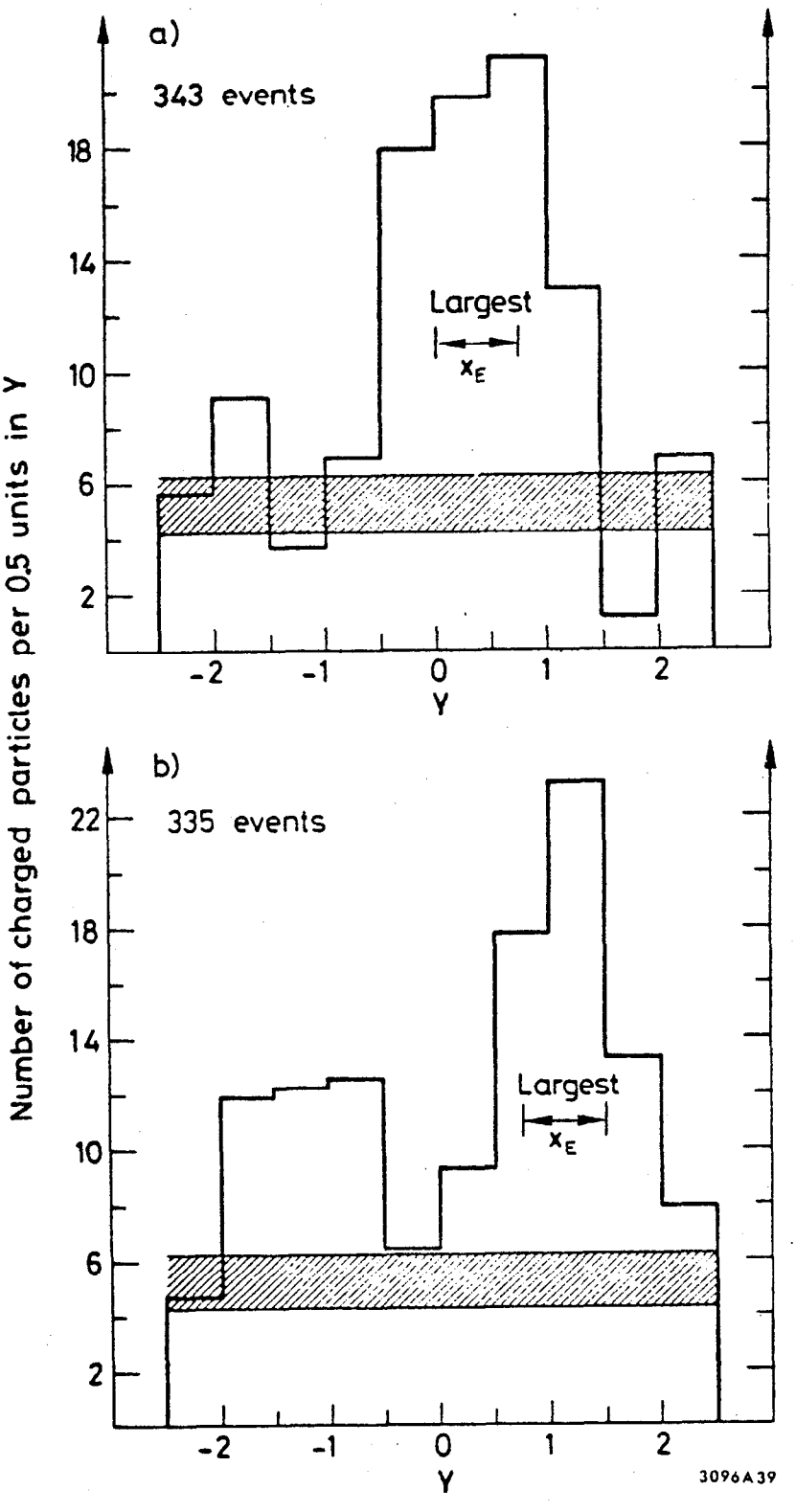
a)
343 events
Largest
x_E
b)
335 events
Largest
x_E
Number of charged particles per 0,5 units in Y
Y
3096A39

Fig. 28

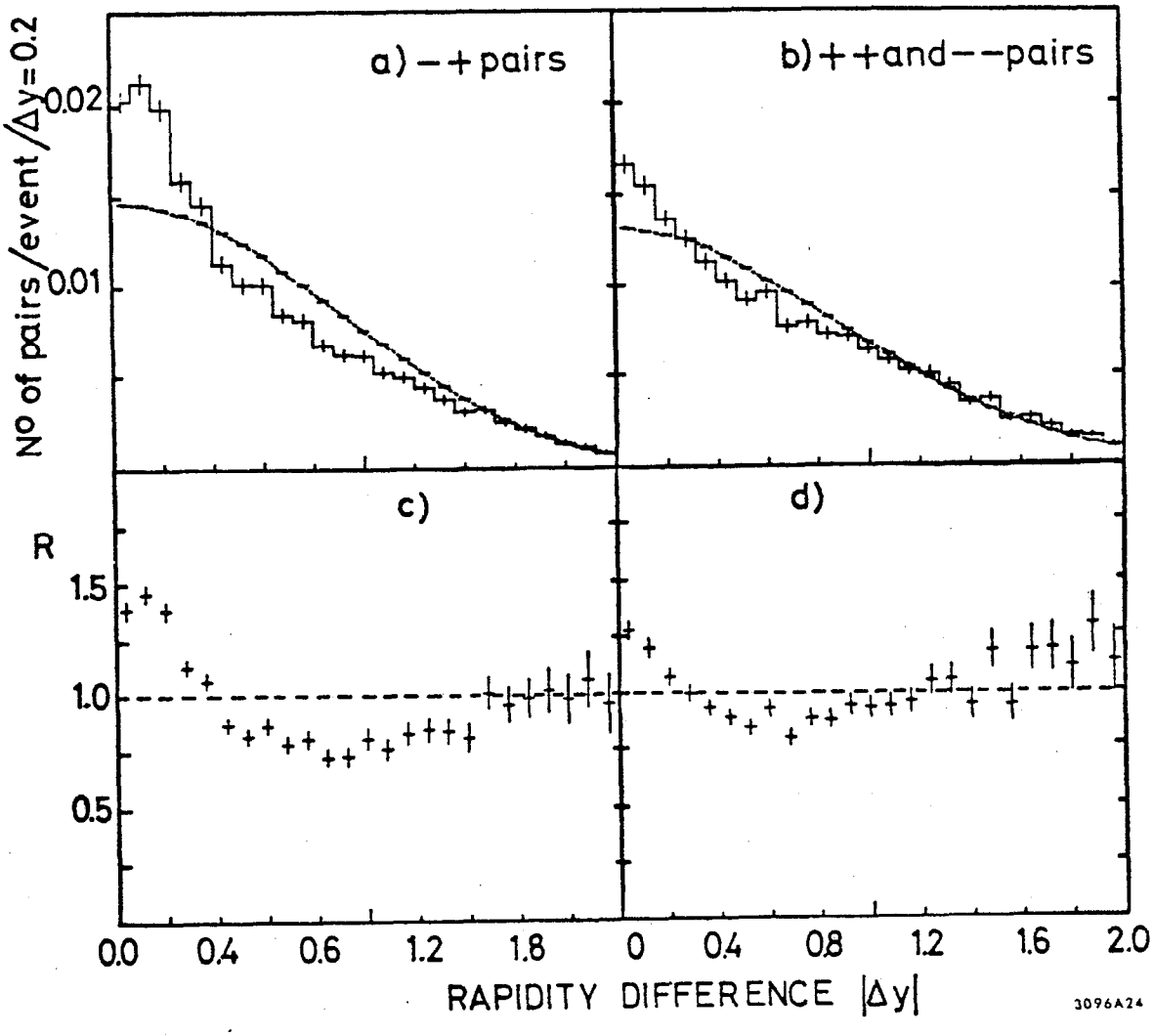
a) −+ pairs
b) ++ and −− pairs
c)
d)
N° of pairs / event / Δy = 0.2
0.02
0.01
R
1.5
1.0
0.5
0.0
0.4
0.6
1.2
1.8
0
0.4
0.8
1.2
1.6
2.0
RAPIDITY DIFFERENCE |Δy|
3096A24

Fig. 29

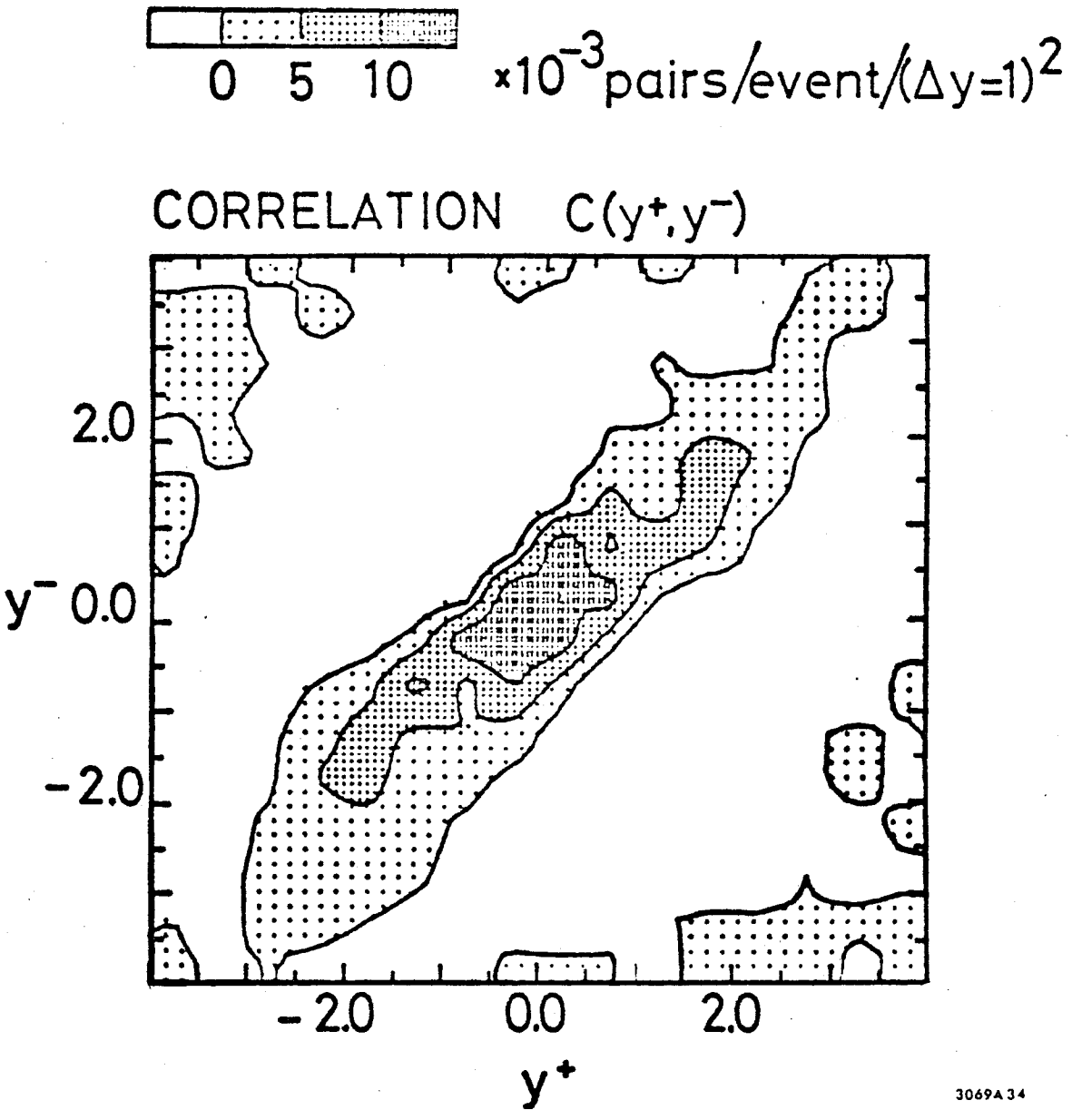
0 5 10
×10⁻³ pairs/event/(Δy=1)²
CORRELATION C(y⁺,y⁻)
2.0
y⁻ 0.0
-2.0
-2.0
0.0
2.0
y⁺
3069A34

Fig. 30

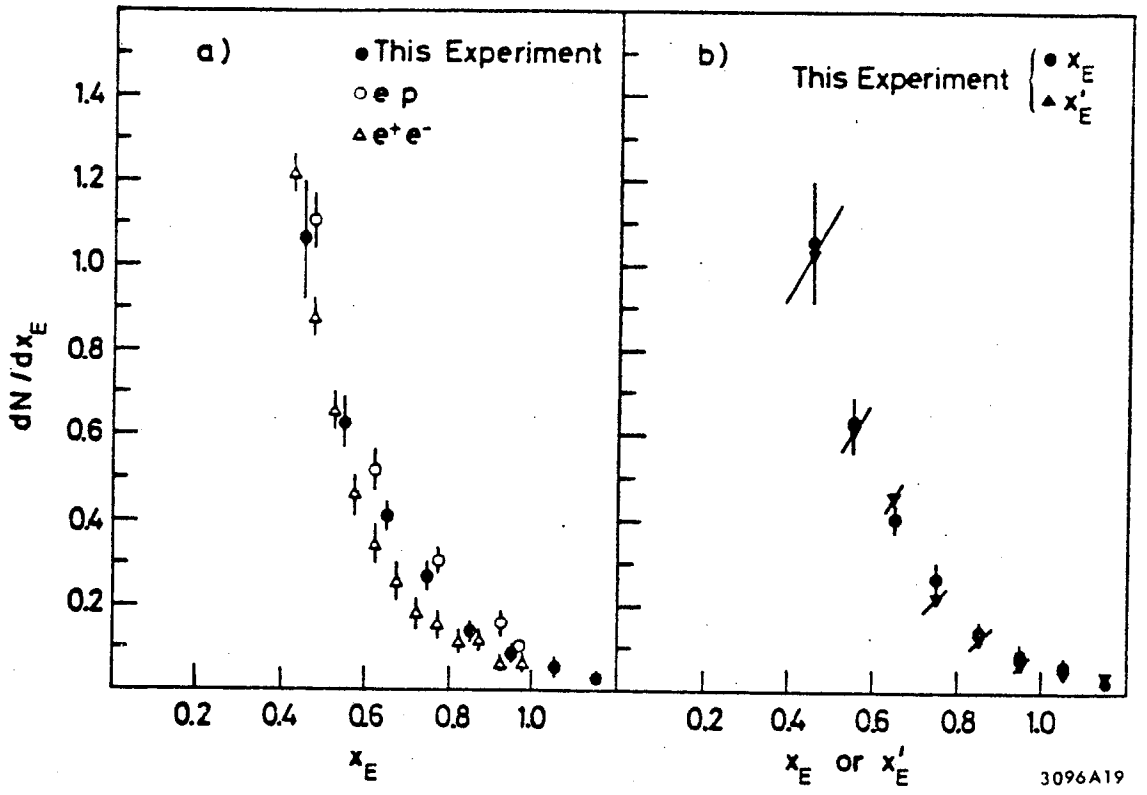
a)
This Experiment
e p
e+e-
b)
This Experiment
xE
x'E
dN/dxE
1.4
1.2
1.0
0.8
0.6
0.4
0.2
0.2
0.4
0.6
0.8
1.0
xE
xE or x'E
3096A19

Fig. 31

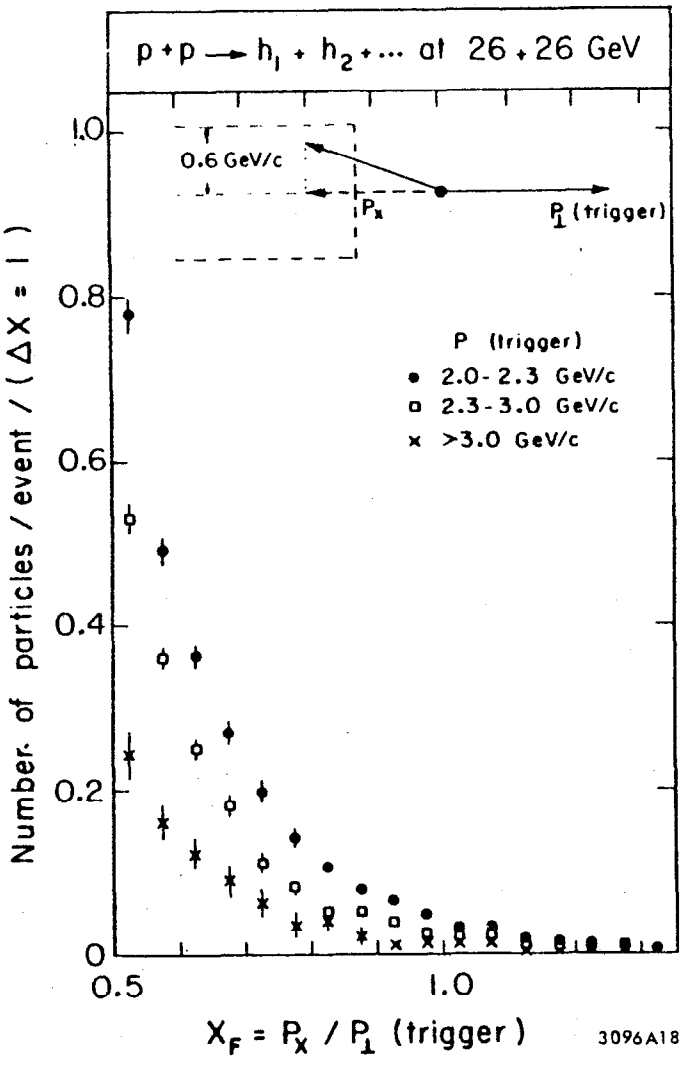
p + p → h1 + h2 + ... at 26 + 26 GeV
0.6 GeV/c
Px
P⊥ (trigger)
P (trigger)
• 2.0 - 2.3 GeV/c
□ 2.3 - 3.0 GeV/c
× >3.0 GeV/c
Number of particles / event / (ΔX = 1)
1.0
0.8
0.6
0.4
0.2
0
0.5
1.0
XF = Px / P⊥ (trigger)
3096A18

Fig. 32

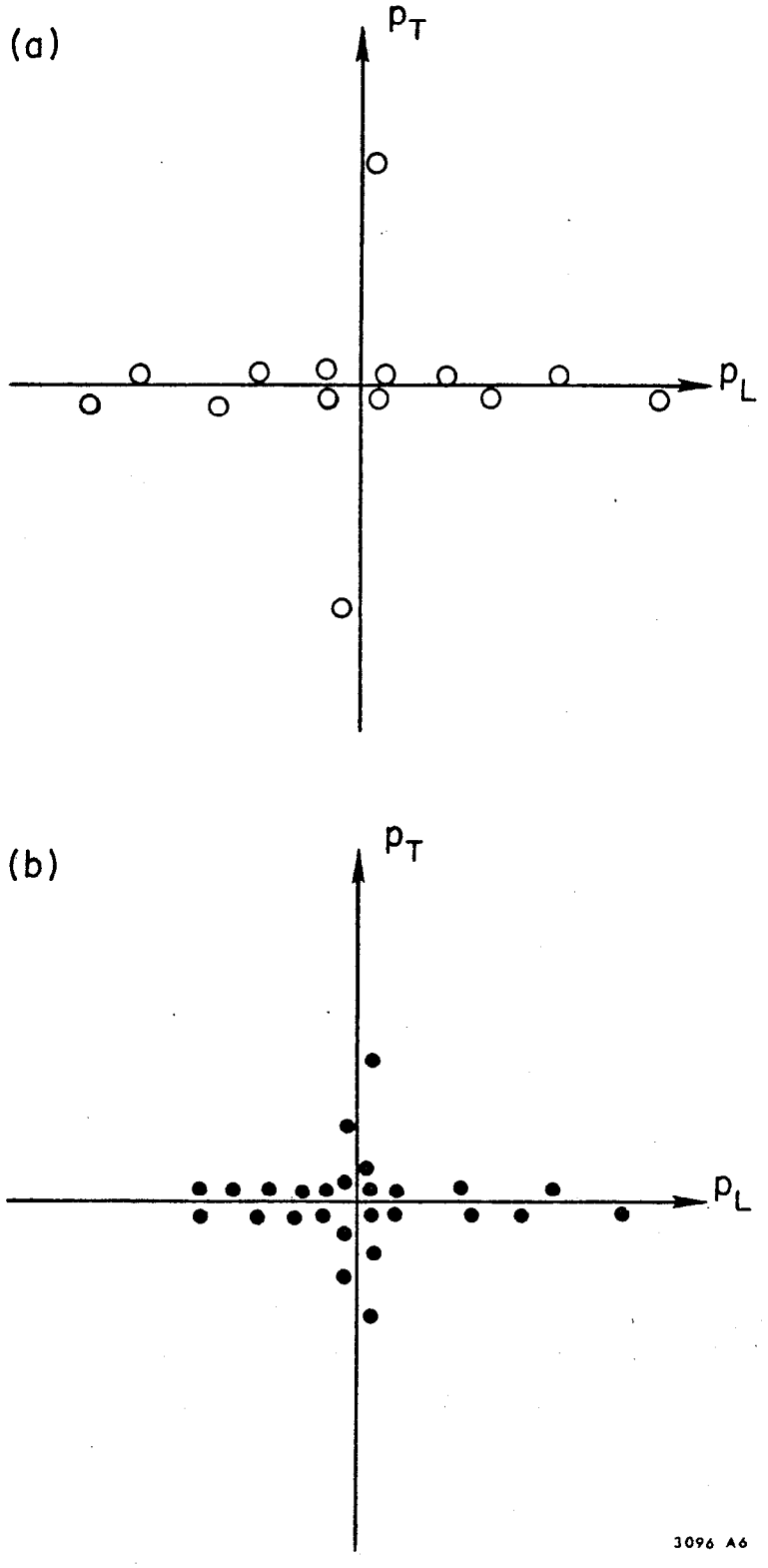

Fig. 33

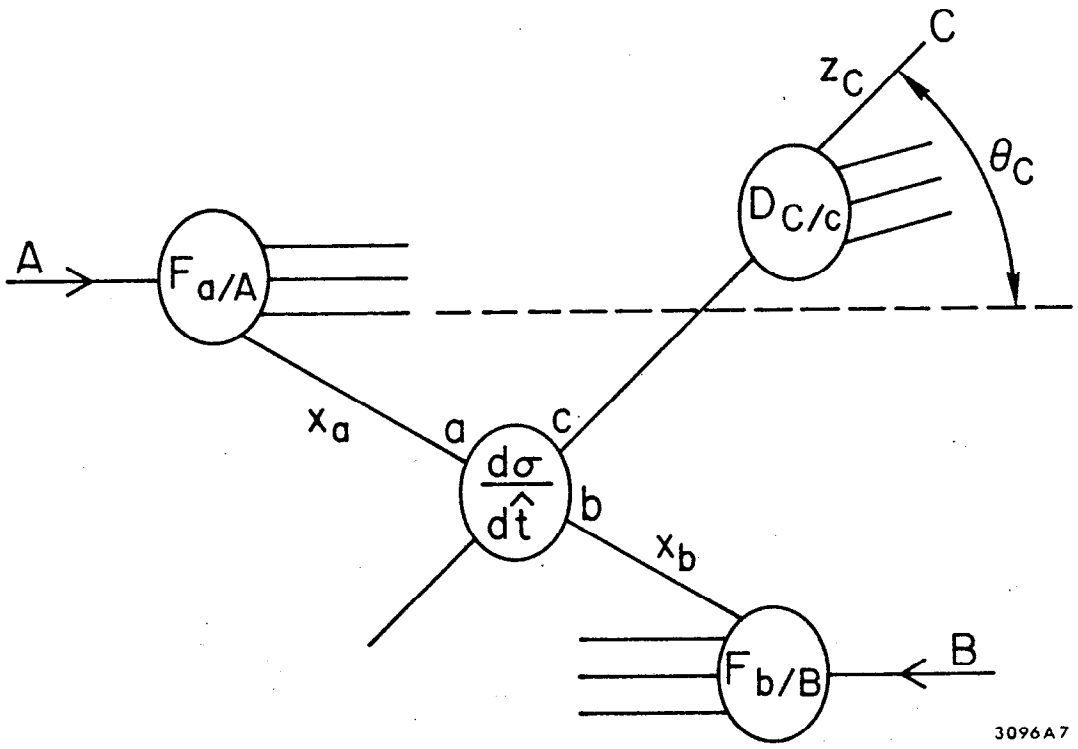

Fig. 34

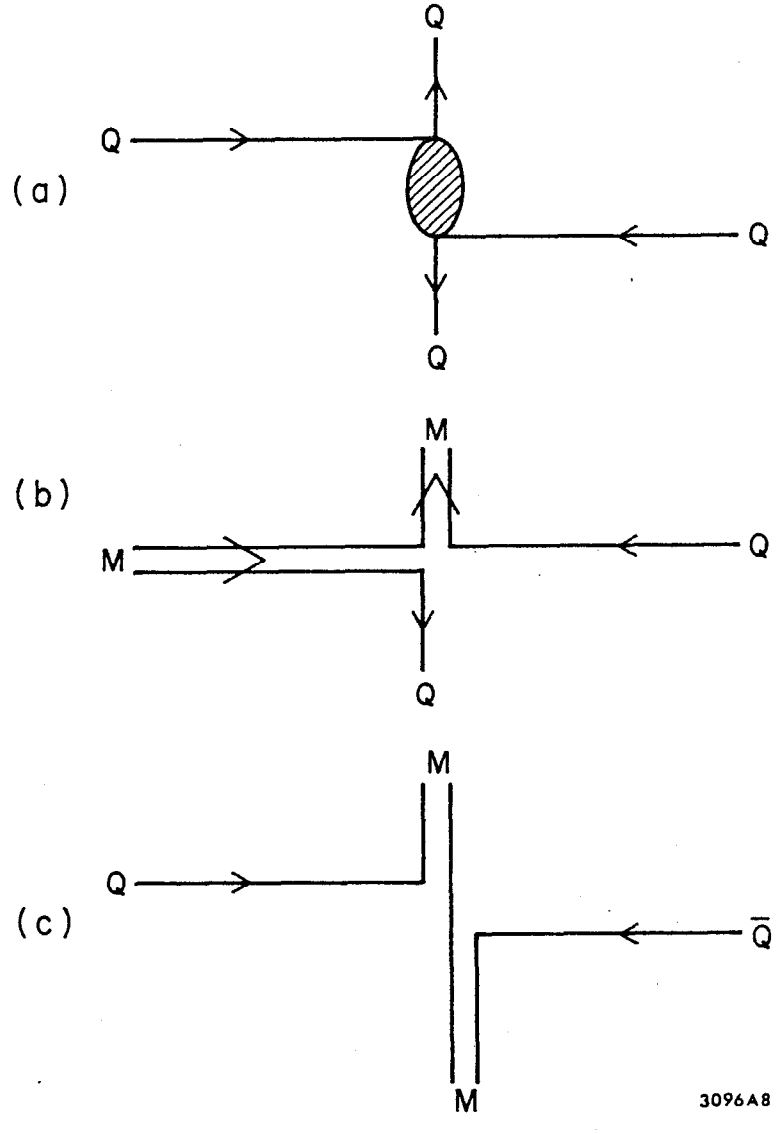

Fig. 35

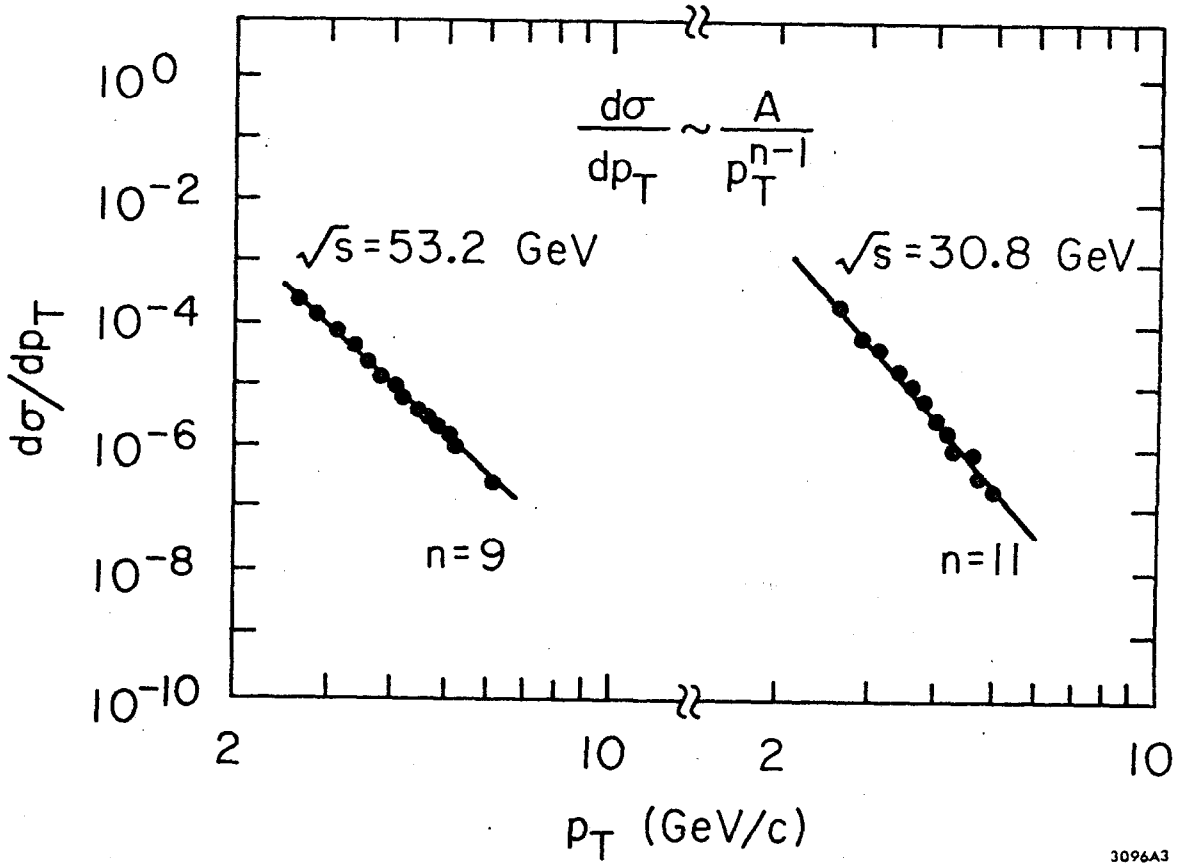
10^0
10^{-2}
10^{-4}
10^{-6}
10^{-8}
10^{-10}
$d\sigma/dp_T$
$\frac{d\sigma}{dp_T} \sim \frac{A}{p_T^{n-1}}$
$\sqrt{s}$ = 53.2 GeV
$\sqrt{s}$ = 30.8 GeV
n = 9
n = 11
2
10
2
10
p_T (GeV/c)
3096A3

Fig. 36

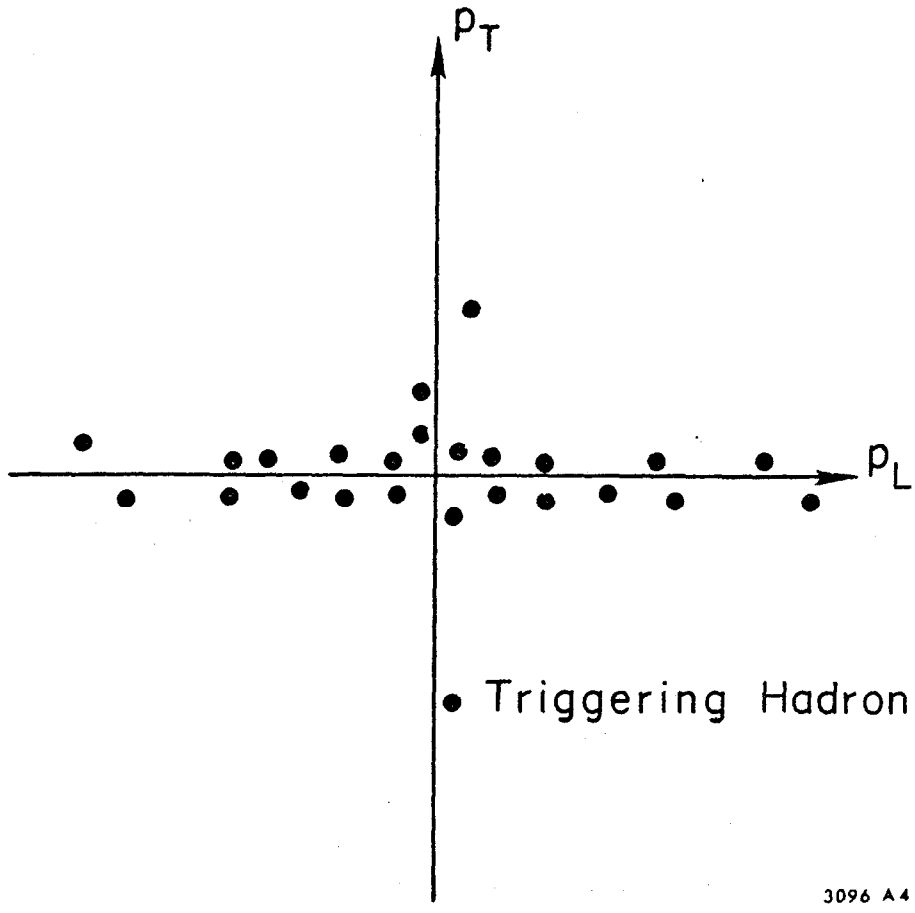

Fig. 37

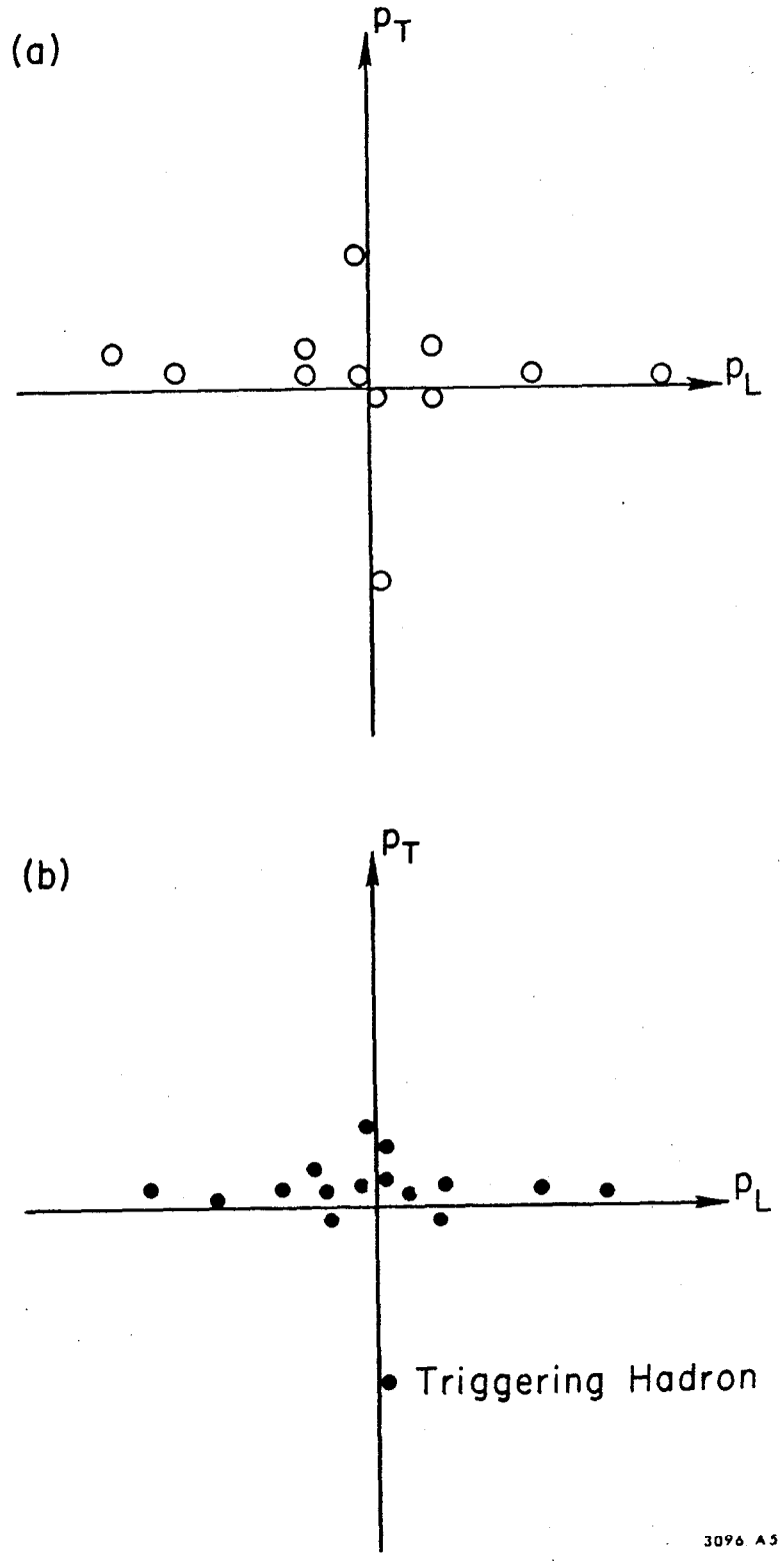

Fig. 38

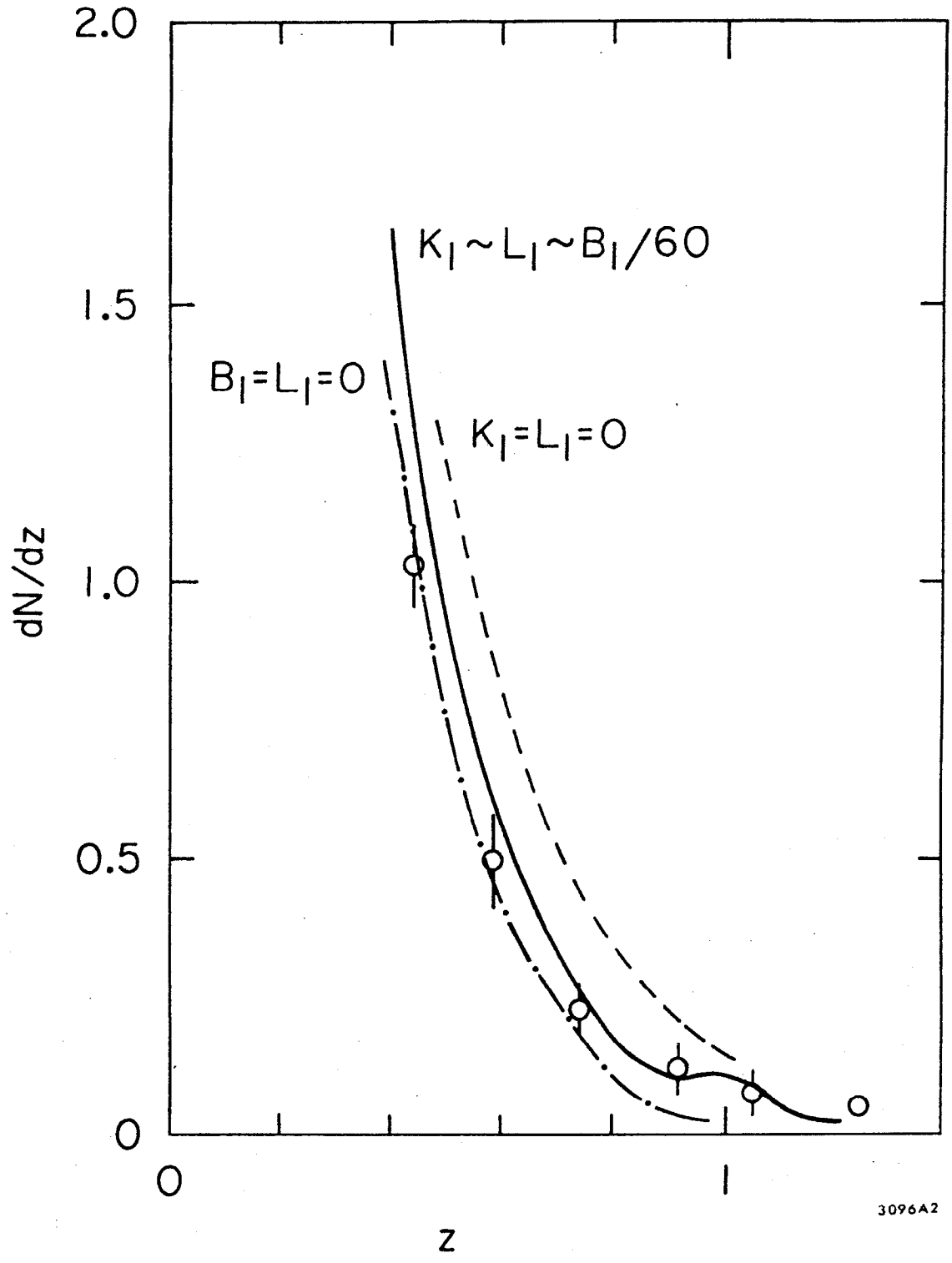

Fig. 39

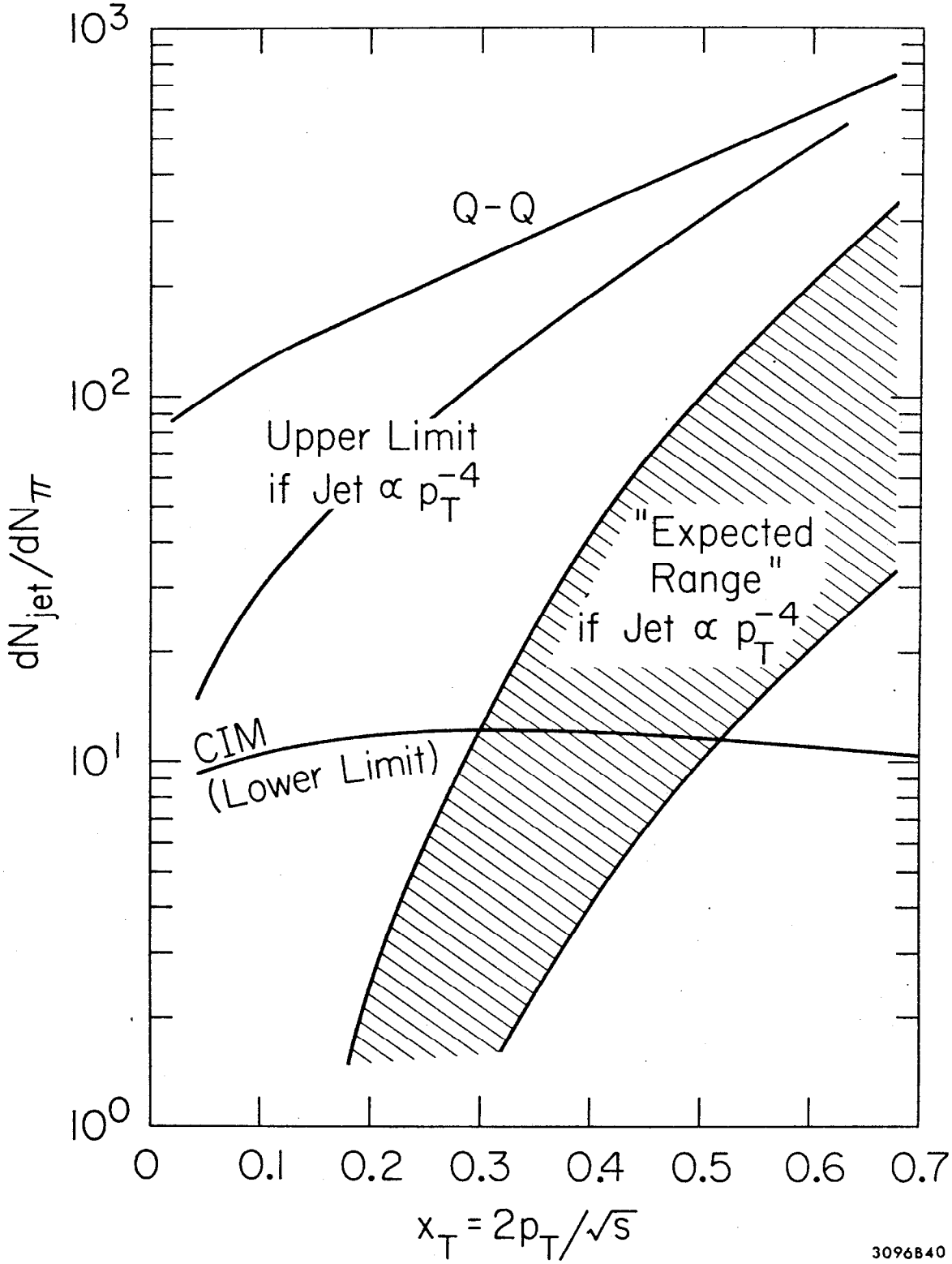
10^3
10^2
10^1
10^0
dN_{jet}/dN_π
Q-Q
Upper Limit
if Jet $\propto p_T^{-4}$
"Expected
Range"
if Jet $\propto p_T^{-4}$
CIM
(Lower Limit)
0
0.1
0.2
0.3
0.4
0.5
0.6
0.7
$x_T = 2p_T/\sqrt{s}$
3096B40

Fig. 40